Thermodynamics of Geologic Fluids

Matthew J. Steele-MacInnis

Dissertation submitted to the faculty of the Virginia Polytechnic Institute and State University in partial fulfillment of the requirements for the degree of

Doctor of Philosophy
In
Geosciences

Robert J. Bodnar, Chair
Patricia M. Dove
Robert P. Lowell
J. Donald Rimstidt

April 25th 2013
Blacksburg, VA

Keywords: hydrothermal fluids, fluid inclusions, silica, quartz, carbon capture and storage, fluid-mineral interaction, ore deposits

Thermodynamics of Geologic Fluids

Matthew J. Steele-MacInnis

ABSTRACT

Fluids play a vital role in essentially all geologic environments and processes, and are the principal media of heat and mass transfer in the Earth. The properties of geologic fluids can be diverse, as fluids occur at conditions ranging from ambient temperatures and pressures at Earth's surface, to extreme temperatures and pressures in Earth's deep interior. Regardless the wide ranges of conditions at which geologic fluids occur, fluid properties are described and governed by the same fundamental thermodynamic relationships. Thus, application of thermodynamic principles and methods allows us to decipher the properties and roles of geologic fluids, to help understand geologic processes.

Fluid inclusions in minerals provide one of the best available tools to study the compositions of geological fluids. Compositions of fluid inclusions can be determined from microthermometric measurements, based on the vapor-saturated liquidus conditions of model chemical systems, or by various microanalytical techniques. The vapor-saturated liquidus relations of the system H_2O-NaCl-$CaCl_2$ have been modeled to allow estimation of fluid inclusion compositions by either microthermometric or microanalytical methods.

Carbon capture and storage (CCS) in deep saline formations represents one option for reducing anthropogenic CO_2 emissions into Earth's atmosphere. Availability of storage volume in deep saline formations is a significant component of injection and storage planning. Investigation of the volumetric properties of CO_2, brine and CO_2-saturated brine reveals that storage volume requirements are minimized when CO_2 dissolves into brine. These results suggest that a protocol involving brine extraction, CO_2 dissolution and re-injection may optimize CCS in deep saline formations.

Numerical modeling of quartz dissolution and precipitation in a sub-seafloor hydrothermal system was used to understand the role of fluid-phase immiscibility ("boiling") on quartz-fluid interactions, and to predict where in the system quartz could deposit and trap fluid inclusions. The spatial distribution of zones of quartz dissolution and precipitation is complex, owing to the many inter-related factors controlling quartz solubility. Immiscibility exerts a strong control over the occurrence of quartz precipitation in the deeper regions of fluid circulation.

ATTRIBUTION

Several colleagues participated in the research and aided in the writing of the three manuscripts that comprise this dissertation. A brief description of their contributions are included here.

Chapter 1. Numerical model to determine the composition of H_2O-NaCl-$CaCl_2$ fluid inclusions based on microthermometric and microanalytical data

Jon Naden, PhD (British Geological Survey, Keyworth, UK) is currently a Minerals Geoscientist at the British Geological Survey. Dr. Naden was a coauthor of this paper, and contributed to development of the numerical model.

Robert J. Bodnar, PhD (Fluids Research Laboratory, Virginia Tech Department of Geosciences) is currently a University Distinguished Professor and the C. C. Garvin Professor of Geochemistry at Virginia Tech. Dr. Bodnar was a coauthor of this paper, and contributed to development of the numerical model.

Chapter 2. Volumetrics of CO_2 storage in deep saline formations

Ryan Capobianco, MSc (Fluids Research Laboratory, Virginia Tech Department of Geosciences) is currently a PhD student at Virginia Tech. Mr. Capobianco was a coauthor of this paper, and contributed to the conceptual model and calculations.

Robert Dilmore, PhD (National Energy Technology Laboratory [NETL], U.S. Department of Energy) is currently a Researcher at NETL. Dr. Dilmore was a coauthor of this paper, and contributed to applications of the results to CO_2 storage modeling.

Angela Goodman, PhD (National Energy Technology Laboratory [NETL], U.S. Department of Energy) is currently a Researcher at NETL. Dr. Goodman was a coauthor of this paper, and contributed to the conceptual model and implications.

George Guthrie, PhD (National Energy Technology Laboratory [NETL], U.S. Department of Energy) is currently the Focus Area Lead for Geological and Environmental Systems at NETL. Dr. Guthrie was a coauthor of this paper, and contributed to the conceptual model and implications.

J. Donald Rimstidt, PhD (Geochemistry, Virginia Tech Department of Geosciences) is currently a Professor Emeritus of Geochemistry at Virginia Tech. Dr. Rimstidt was a coauthor of this paper, and contributed the development of the quantitative model and assessment of fluid-mineral reactions.

Robert J. Bodnar, PhD (Fluids Research Laboratory, Virginia Tech Department of Geosciences) is currently a University Distinguished Professor and the C. C. Garvin Professor of Geochemistry at Virginia Tech. Dr. Bodnar was a coauthor of this paper, and contributed to the design of the study and interpretations of results and implications.

Chapter 3. The role of fluid phase immiscibility in quartz dissolution and precipitation in sub-seafloor hydrothermal systems

Liang Han, MSc (Geophysics, Virginia Tech Department of Geosciences) is currently a PhD student at Virginia Tech. Mr. Han was a coauthor of this paper, and contributed to the fluid flow simulations and interpretations of results.

Robert P. Lowell, PhD (Geophysics, Virginia Tech Department of Geosciences) is currently a Research Professor at Virginia Tech. Dr. Lowell was a coauthor of this paper, and contributed to the experimental design and interpretations.

J. Donald Rimstidt, PhD (Geochemistry, Virginia Tech Department of Geosciences) is currently a Professor Emeritus of Geochemistry at Virginia Tech. Dr. Rimstidt was a coauthor of this paper, and contributed to the quartz dissolution and precipitation modeling and interpretations.

Robert J. Bodnar, PhD (Fluids Research Laboratory, Virginia Tech Department of Geosciences) is currently a University Distinguished Professor and the C. C. Garvin Professor of Geochemistry at Virginia Tech. Dr. Bodnar was a coauthor of this paper, and contributed to the design and implementation of the simulations.

TABLE OF CONTENTS

LIST OF FIGURES

LIST OF TABLES

PREFACE

Each chapter of this dissertation represents a published manuscript.

Chapter 1 was published in the journal *Geochimica et Cosmochimica Acta* in 2011, with coauthors Jon Naden (British Geological Survey) and Robert J. Bodnar (Virginia Tech).

Chapter 2 was published in the journal *Environmental Science & Technology* in 2013, with coauthors Ryan Capobianco (Virginia Tech), Robert Dilmore (National Energy Technology Laboratory - NETL), Angela Goodman (NETL), George Guthrie (NETL), J. Donald Rimstidt (Virginia Tech) and Robert J. Bodnar (Virginia Tech).

Chapter 3 was published in the journal *Earth and Planetary Science Letters* in 2012, with coauthors Liang Han (Virginia Tech), Robert P. Lowell (Virginia Tech), J. Donald Rimstidt (Virginia Tech) and Robert J. Bodnar (Virginia Tech).

1 Numerical model to determine the composition of H_2O-NaCl-$CaCl_2$ fluid inclusions based on microthermometric and microanalytical data[1]

Published in Geochimica et Cosmochimica Acta in 2011, with coauthors Jon Naden (British Geological Survey) and Robert J. Bodnar (Virginia Tech).

1.1 Abstract

Natural fluids approximated by the H_2O-NaCl-$CaCl_2$ system are common in a wide range of geologic environments, including sedimentary basins associated with hydrocarbon occurrences and MVT deposits, submarine hydrothermal systems, and other metamorphic, magmatic and hydrothermal environments. We present a comprehensive numerical model to determine the compositions of fluid inclusions in the H_2O-NaCl-$CaCl_2$ system based on microthermometric and microanalytical data. The model consists of six polynomial correlation equations that describe liquid salinity as a function of NaCl/$CaCl_2$ ratio and melting temperature on each of the ice, hydrohalite, halite, antarcticite, $CaCl_2{\cdot}4H_2O$ and $CaCl_2{\cdot}2H_2O$ vapor-saturated liquidus surfaces. The cotectic and peritectic boundaries are determined from the intersections of the liquidus surfaces. The model is implicitly internally consistent and topologically correct.

The model expands upon the compositional range of applicability and the data types that can be used for compositional determination. It reproduces experimental data for all compositions between pure H_2O, pure NaCl and $CaCl_2{\cdot}4H_2O$, and yields accurate reproductions of the H_2O-NaCl and H_2O-$CaCl_2$ binaries. Furthermore, in comparison to previously published

models, the one presented here eliminates systematic errors, wavy isotherms and cotectic and peritectic curves with local extrema.

1.2 List of symbols

n_i number of moles of component *i*

X_i Mole fraction of component *i*

[=(n_i)/(n_{total})]

Ψ The molar fraction of NaCl relative to NaCl + $CaCl_2$

[= (X_{NaCl})/(X_{NaCl} + X_{CaCl2})].

Φ The weight fraction of NaCl relative to NaCl + $CaCl_2$

[=(wt.% NaCl)/(wt.% NaCl + wt.% $CaCl_2$)]

Ω The molar fraction of $CaCl_2$ relative to H_2O + $CaCl_2$

[= (X_{CaCl2})/(X_{CaCl2} + X_{H2O})].

$T_{m,x}$ Temperature (°C) at which solid phase *x* melts on the one-solid-stable vapor-saturated liquidus surface.

$T_{pb,x}$ Temperature (°C) at which solid phase *x* melts on either a cotectic or peritectic phase boundary curve, in the presence of liquid plus vapor plus another solid.

Subscripts *x: ice; hh* (= hydrohalite); *h* (=halite); *ant* (= antarcticite); *Ca4h* (tetrahydrate = $CaCl_2 \cdot 4H_2O$); *Ca2h* (dihydrate = $CaCl_2 \cdot 2H_2O$ = sinjarite)

S_{mol} Total salinity on a mole fraction basis [= X_{NaCl} + X_{CaCl2}].

S_{wt} Total salinity on a wt.% basis [=(wt.% NaCl + wt.% $CaCl_2$)]

a_i Regression coefficient.

1.3 Introduction

Aqueous fluids in which NaCl and $CaCl_2$ are the two most abundant salts and which may be adequately described by the system H_2O-NaCl-$CaCl_2$ are common in many geologic environments. Fluids of this composition are commonly found in sedimentary basins (COLLINS, 1975; Lowenstein et al., 2003; Hanor and MacIntosh, 2007), Mississippi Valley-Type Pb-Zn deposits (Haynes and Kessler, 1987; Basuki and Spooner, 2002; Stoffell et al., 2008), Archean lode gold deposits (Robert and Kelly, 1987), skarn and greisen deposits (Kwak and Tan, 1981; Layne and Spooner, 1991; Samson et al., 2008), iron-oxide Cu-Au (IOCG) -type deposits (Xu, 2000), magmatic Cu-Ni deposits (Li and Naldrett, 1993), crystalline rocks of the Canadian Shield (Frape et al., 1984), mafic pegmatoids associated with platinum deposits in the Bushveld Complex (Schiffries, 1990) and elsewhere (Nyman et al., 1990), and in sub-seafloor hydrothermal systems (Vanko, 1988; Vanko et al., 1988). Thus, fluid inclusions approximated by the system H_2O-NaCl-$CaCl_2$ are common in a diverse range of geologic environments, and a methodology to interpret microthermometric data obtained from these inclusions is necessary to better understand geologic processes such as diagenesis, hydrocarbon migration, evolution of hydrothermal systems, metal transport, metamorphism and crystallization of magmas.

The best source of information concerning the compositions of paleo-geologic fluids comes from fluid inclusions (Roedder, 1984). The temperatures at which phase changes occur within a fluid inclusion during heating can be used to estimate the fluid composition, assuming that PTX phase relationships of representative fluid systems are available. In addition, the elemental ratios in saline aqueous inclusions can be determined by microanalysis, for example by laser ablation ICPMS (LA-ICPMS) (Günther et al., 1998), which provides an additional constraint for determining the fluid composition when combined with microthermometric data.

The system H_2O-NaCl-$CaCl_2$ (Fig. 1.1) is a three-component system, and the phase rule requires that two variables must be specified to determine a unique liquid composition on the vapor-saturated liquidus, whereas one variable is sufficient to determine a unique liquid composition on any vapor-saturated, two-solid-plus-liquid boundary (cotectic or peritectic curve). The temperatures of last melting of solid phases, either on a cotectic or peritectic curve ($T_{pb,x1}$) or on the one-solid liquidus ($T_{m,x2}$), are two possible sources of data; elemental ratios (Ψ or Φ, referring to molar or weight proportions, respectively) determined from LA-ICPMS represent another data source. (Note that whereas several previous studies of the H_2O-NaCl-$CaCl_2$ system have used the term "X_{NaCl}" to refer to the weight ratio of NaCl relative to NaCl+$CaCl_2$, we adopt the more common notation such that X_{NaCl} refers to the mole fraction of NaCl, and we instead denote the weight and molar ratios of NaCl relative to NaCl+$CaCl_2$ as Φ and Ψ, respectively). As discussed in detail below, depending upon which data are available, fluid inclusion compositions may be determined using a combination of either the temperature of melting on a cotectic or peritectic *and* a temperature of melting on the vapor-saturated liquidus surface ($T_{pb,x1}$+$T_{m,x2}$), or a temperature of melting on the vapor-saturated liquidus surface *and* the ratio of the amount of NaCl relative to the total amount of NaCl and $CaCl_2$, ($T_{m,x}$+ either Φ or Ψ – the two compositional ratios can be directly converted to one another via the molar masses of the species) or the temperature of melting of one phase on a cotectic or peritectic *and* the temperature of melting of a second phase on a cotectic or peritectic ($T_{pb,x1}$+$T_{pb,x2}$).

Compositions of H_2O-NaCl-$CaCl_2$ fluid inclusions can be approximated using graphically-displayed phase equilibrium data (e.g., Konnerup-Madsen, 1979; Robert and Kelley, 1987) or using empirical or theoretical data (Oakes et al., 1990; Williams-Jones and Samson, 1990; Naden, 1996; Chi and Ni, 2007), and several computer packages have been developed to

interpret data from fluid inclusions whose compositions are approximated by the system H_2O-NaCl-$CaCl_2$ (Naden, 1996; Bakker, 2003; Chi and Ni, 2007). While each model works well over a limited range of T-X conditions, none of the currently available models is equipped to calculate fluid inclusion compositions over the complete range in compositions reported for natural H_2O-NaCl-$CaCl_2$ fluid inclusions. Moreover, some of the previously published equations (Oakes et al., 1990; Naden, 1996; Chi and Ni, 2007) are characterized by structured residuals with respect to the experimental data, or have inflections ("bumps") between data points and local extrema along calculated isotherms and univariant curves, as described in more detail below. Finally, none of the previously published models provide the ability to determine fluid compositions using the complete range of possible input data, such as the temperature of melting on a cotectic or peritectic *and* a temperature of melting on the vapor-saturated liquidus surface ($T_{pb,x1}$+$T_{m,x2}$), or a temperature of melting on the vapor-saturated liquidus surface *and* the weight fraction of NaCl relative to NaCl + $CaCl_2$ ($Tm_{,x}$ +Φ), or the temperature of melting of one phase on a cotectic or peritectic *and* the temperature of melting of a second phase on a cotectic or peritectic ($T_{pb,x1}$+$T_{pb,x2}$), as described below. The model presented here incorporates those aspects of previous models that have been shown to be consistent with the phase equilibria determined from experimental data, and adds new equations and methods to expand the T-X range of applicability, remove anomalies inherent in some previous statistical models, and expand the range of input data that may be used to estimate the composition of H_2O-NaCl-$CaCl_2$ fluid inclusions.

The goal of this study is to provide a comprehensive set of empirical equations that describe the portion of the vapor-saturated H_2O-NaCl-$CaCl_2$ system that includes the range of compositions of natural fluid inclusions and the range of available experimental data. As such,

this study covers a region within the ternary system bounded by the H_2O apex, the NaCl apex and the composition of $CaCl_2 \cdot 4H_2O$ on the H_2O-$CaCl_2$ binary (1.1b).

We emphasize that the model developed in this study applies to stable equilibrium melting behavior in the system H_2O-NaCl-$CaCl_2$, but metastable melting phenomena are also frequently encountered in $CaCl_2$-bearing fluids (e.g., Potter and Clynne, 1978; Roedder, 1984; Vanko et al., 1988; Baumgartner and Bakker, 2009). For instance, Vanko et al. (1988) reported that some of their synthetic H_2O-NaCl-$CaCl_2$ fluid inclusions could not be completely frozen, while others could only be frozen to a metastable phase assemblage. Likewise, Linke (1958) and Baumgartner and Bakker (2009) report the occurrence of several metastable phase assemblages in the H_2O-$CaCl_2$ binary system. While we acknowledge that metastable behavior in the H_2O-NaCl-$CaCl_2$ system does occur, the model presented in this study specifically represents only the *stable* phase relations on the vapor-saturated H_2O-NaCl-$CaCl_2$ liquidus.

1.4 Vapor-saturated phase relations in the H_2O-NaCl-$CaCl_2$ system

Phase relations on the vapor-saturated liquidus of the H_2O-NaCl-$CaCl_2$ ternary system are shown in Figure 1.1. The system is characterized by at least eight fields in which a single solid phase is in equilibrium with liquid and vapor. Six of these fields are described in this study; two additional fields in the high salinity, $CaCl_2$-rich, low weight fraction NaCl (Φ) part of the system (near the $CaCl_2$ apex; Fig. 1.1a) are not considered here because experimental data are not available in that part of the ternary system (although these phases have been characterized along the H_2O-$CaCl_2$ binary, e.g. Linke, 1958). Figure 1.1 shows phase relationships in the part of the system that includes the range of reported compositions of natural fluid inclusions. The phase boundaries shown in Figure 1.1c were calculated using the equations derived in this study and below we compare these calculated phase boundaries with experimental data.

Each field shown Figure 1.1 is labeled according to the solid phase that is in equilibrium with liquid and vapor. At low salinity, near the H_2O apex, the stable solid phase on the liquidus surface is H_2O ice (Fig. 1.1a, c). At intermediate to high salinity and $R_{wt} > 0.04$, halite (NaCl) is the stable solid phase (Fig. 1.1a, c). A field in which hydrohalite ($NaCl \cdot 2H_2O$) is the stable solid phase separates the ice- and halite-stable fields (Fig. 1.1a, c). At intermediate to high salinity and $R_{wt} < 0.04$, calcium chloride hydrates are the stable solid phases: antarcticite ($CaCl_2 \cdot 6H_2O$) is the stable phase from about 30 to 50 wt.% total salt, "tetrahydrate" ($CaCl_2 \cdot 4H_2O$) is the stable solid from 50 to about 57 wt.% salt, and "dihydrate" ($CaCl_2 \cdot 2H_2O$ = sinjarite) is stable from about 57 to 75 wt.% salt (Fig. 1.1a, c). To our knowledge, ternary experimental data are not available for the H_2O-NaCl-$CaCl_2$ system at salinities above 75 wt.% total salt, thus the $CaCl_2 \cdot H_2O$ and $CaCl_2$ (anhydrous) stable fields are not included in this study (area near the $CaCl_2$ apex on Fig. 1.1a labeled with a question mark, ?). Also shown in Figure 1.1a are the compositions of hydrohalite (61.86 wt.% NaCl on the H_2O-NaCl binary), antarcticite (50.07 wt.% $CaCl_2$ on the H_2O-$CaCl_2$ binary), $CaCl_2 \cdot 4H_2O$ (60.63 wt.% $CaCl_2$ on the H_2O-$CaCl_2$ binary) and $CaCl_2 \cdot 2H_2O$ (75.49 wt.% $CaCl_2$ on the H_2O-$CaCl_2$ binary).

The fields in which one solid is in equilibrium with liquid and vapor are separated from each other by peritectic or cotectic boundary curves. Ice and hydrohalite are separated by the ice + hydrohalite (I+HH) cotectic, which extends from the ternary eutectic point (E) at -52°C (Yanatieva, 1946) to the binary H_2O-NaCl eutectic (E') at -21.2°C (HALL et al., 1988). Ice and antarcticite are separated by the ice + antarcticite (I+A) cotectic, which extends from the ternary eutectic (E) to the binary H_2O-$CaCl_2$ eutectic (E") at -49.8°C (Yanatieva, 1946). The hydrohalite and antarcticite fields are separated from each other by the hydrohalite + antarcticite (HH+A) cotectic curve, which extends from the ternary eutectic (E) to the first ternary peritectic (P_1) at -

22.4°C (Yanatieva, 1946). The hydrohalite field is separated from the halite field by the hydrohalite + halite (HH+H) peritectic curve, which extends from the first ternary peritectic (P_1) to the binary H_2O-NaCl peritectic (P') at +0.1°C (Linke, 1958). The halite field is separated from the antarcticite field by the halite + antarcticite (H+A) cotectic curve, which extends from the first ternary peritectic (P_1) to the second ternary peritectic (P_2) at +29°C (Schiffries, 1990). The halite field is separated from the tetrahydrate field by the halite + tetrahydrate (H+Ca4h) cotectic, which extends from the second ternary peritectic (P_2) to the third ternary peritectic (P_3) at approximately +45°C (estimated from the data of Linke, 1958). The halite field is separated from the dihydrate field by the halite + dihydrate (H+Ca2h) cotectic curve, which extends from the third ternary peritectic (P_3) to the fourth ternary peritectic (P_4) at >110°C (Linke, 1958). The antarcticite field is separated from the tetrahydrate field by the antarcticite + tetrahydrate (A+Ca4h) peritectic curve, which extends from the second ternary peritectic point (P_2) to the first binary H_2O-$CaCl_2$ peritectic (P_1") at +30.1°C (Linke, 1958). Tetrahydrate is separated from dihydrate by the tetrahydrate + dihydrate (Ca4h+Ca2h) peritectic curve, which extends from the third ternary peritectic point (P_3) to the second binary H_2O-$CaCl_2$ peritectic (P_2") at +45.1°C (Linke, 1958). The locations of other boundary curves that occur at higher salinity conditions close to the H_2O-$CaCl_2$ binary and near the $CaCl_2$ apex are not known.

1.5 Sources of experimental data

The experimental data used in the regression analysis are summarized in Table 1.1 and Figure 1.2.

1.5.1 Phase boundaries

Phase boundaries on the vapor-saturated liquidus in the system H_2O-NaCl-$CaCl_2$ are broadly characterized by either cotectic relationships or peritectic relationships. Note that on a cotectic boundary, the phase change behavior that is observed upon heating is always "solid1+solid2→solid2+liquid →liquid", whereas on a peritectic boundary, the reaction observed upon heating is "solid1+liquid→solid2+liquid→liquid". In other words, as a fluid inclusion is heated, the inclusionist would observe two solids shrinking (melting) along a cotectic curve until one disappeared leaving behind the second solid and liquid, whereas s/he would observe one solid growing at the expense of the other along a peritectic curve.

In addition to the T-X data along the cotectic and peritectic phase boundaries summarized in Table 1.1 and Figure 1.3, Schiffries (1990) reported the temperature at the second peritectic point (P_2) of +29°C, which provides an additional constraint on the location of the A+Ca4h, A+H and Ca4h+H phase boundary curves.

1.5.2 Liquidus surfaces

In addition to compositions that lie on each divariant liquidus surface, data for the univariant boundary curves (peritectics or cotectics) adjacent to the surface were included in the regression for each liquidus surface. For example, in modeling the hydrohalite field, data from the I+HH, HH+A and HH+H phase boundaries were used in addition to the hydrohalite-only liquidus data. For each liquidus field, the number of data points that have been used in the regression, including data within the field and those on the phase boundary curves, are listed in Table 1.1.

For the halite liquidus, the high temperature data of Chou (1987) were omitted from the regression analysis, but these data are in excellent agreement with those of Sterner et al. (1988). In addition, the experimental data analyzed in this study include several liquidus temperature

measurements along the anhydrous NaCl-$CaCl_2$ binary (Zhang et al., 1995), but those data are not included in the data set for regression.

For the tetrahydrate liquidus, Linke (1958) reports multiple polymorphs of $CaCl_2 \cdot 4H_2O$ coexisting with different salinity liquids. We have followed the suggestion of Potter and Clynne (1978), who point out that consideration of the phase rule indicates that the "beta" and "gamma" polymorphs are metastable, and so we have included only the "alpha" polymorph solubility data of Linke (1958).

1.6 Equations describing the liquidus and phase boundary curves

The liquidi in a ternary system are divariant surfaces, and thus the total salinity (S_{wt}) can be represented as a function of the weight fraction of NaCl relative to NaCl + $CaCl_2$ (Φ) and the temperature of melting of the last solid phase on the vapor-saturated liquidus ($T_{m,x}$). The cotectic and peritectic curves are univariant lines and therefore both Φ and S_{wt} can be represented as a function of the temperature of melting of solid phase *x* on the cotectic or peritectic ($T_{pb,x}$). Previous studies have generally approached the problem of regression modeling of the vapor-saturated liquidi of ternary systems by fitting separate univariant regression equations to the experimental data on the phase boundary curves (e.g., Sterner et al., 1988; Naden, 1996). While that approach often produces a system of equations with small errors with respect to the experimental data, it also generally yields a model that is not internally consistent because predicted phase boundary curves will not necessarily intersect at the invariant points (eutectic and peritectic points) and predicted isotherms of adjacent fields will not always intersect at the univariant curves as they should. The approach taken in this study has been to regress the data for each liquidus surface, and weight the cotectic and peritectic curve appropriately to ensure that univariant curves represent the intersection of the adjacent liquidus surfaces. This approach has

two advantages: First, it yields a model that is implicitly internally consistent, and secondly, it provides additional constraints on liquidus fields that are represented by sparse experimental data. For example, the only data available for the tetrahydrate field are along the H_2O-$CaCl_2$ binary (as described above). However, isotherms are available at the intersections of the tetrahydrate field with the adjacent antarcticite, halite and dihydrate fields, and these data, combined with data along the H_2O-$CaCl_2$ binary, provide reasonable constraints on the locations of isotherms within the tetrahydrate field.

Regression analyses were conducted using SAS© JMP 8 statistical software. The experimental data on each liquidus surface were regressed to find the equation that best satisfied three criteria: First, the equation was required to accurately reproduce the experimental data; secondly, the resulting isotherms were required to be smooth and monotonic, meaning free of local extrema and inflections; and thirdly, the equations for adjacent liquidus surfaces were required to intersect such that the cotectic and peritectic phase boundaries predicted by the intersection were consistent with experimental data. The percent residuals of each equation with respect to the experimental data were calculated by the expression {(1 - calculated/measured)*100%}.

1.6.1 Ice field

Salinities of fluid inclusions for which H_2O ice is the final solid to melt are described by the following equation, modified from Naden (1996):

$$S_{wt} = \sum_{i=0}^{5} a_i T_{m,ice}^{i} + \sum_{i=6}^{7} a_i \Phi^{(i-5)} + a_8 \Phi\, T_{m,ice}^{2} + a_9 \Phi\, T_{m,ice}^{5} - 0.185 \exp(-T_{m,ice} - 52) \qquad (1.1)$$

where $T_{m,ice}$ is the final ice melting temperature in degrees Celsius and the a_i's are fitting parameters given in Table 1.2. We have added the exponential term at the end of the equation originally provided by Naden (1996) to improve the intersection with the antarcticite field, as discussed below. The equation for the ice liquidus surface of Chi and Ni (2007) (their Eqn. (4)) is based upon extrapolation from their I+HH boundary, and is therefore valid only at high salinity ($T_{m,ice} \leq$ -21°C), and it shows significant structure in the residuals as a function of salinity (Fig. 1.3). The equation of Oakes et al. (1990) (their Eqn. (2)) fits the data well at salinities from 0 to 25 wt. %, but provides a poorer fit to the higher salinity data of Yanatieva (1946), with a negative-sloped, apparently linear structure in the residuals in this range (Fig. 1.3). Equation (1.1) does not reproduce the lowest salinity experimental data as well as the equation of Oakes et al. (1990), but it provides a better fit in general over the entire salinity range of the ice field (Fig. 1.3). For these reasons, Eqn. (1.1) is recommended as the general equation for the ice field, and is adopted for all figures and examples herein, while the equation of Oakes et al. (1990) may be preferable if all data to be analyzed have a $T_{m,ice} \geq$ -15°C.

1.6.2 Hydrohalite field

The salinity of fluid inclusions in which hydrohalite is the final solid phase to melt is described by:

$$S_{mol} = \sum_{i=0}^{2} a_i (T_{m,hh} + 52)^i + a_3 \Psi^{-1} + \sum_{i=4}^{5} a_i \Psi^{i-2} + \sum_{i=6}^{7} a_i \Psi \, (T_{m,hh} + 52)^{i-4} + a_8 \Psi^2 (T_{m,hh} + 52) \qquad (1.2)$$

with the a_i's listed in Table 1.2. Residuals associated with calculation of the total salinity in terms of weight percent (S_{wt}) using Eqn (1.2) are generally within ± 5 % of experimental values,

excluding one outlier (Fig. 1.3). Equation (2) does not significantly improve on the residuals associated with the equation of Naden (1996) for the hydrohalite field (Fig. 1.3); however, the equation of Naden (1996) tends to over-fit the data, and isotherms generated using Naden's equation have local extrema between data points, (at some temperatures crossing the H+HH peritectic curve to predict compositions that are within the halite field) (Fig. 1.4). Isotherms generated using Eqn. (1.2) are smooth and without local extrema (Fig. 1.4), and thus better reflect the geometry of the hydrohalite liquidus surface.

1.6.3 Halite field

The liquid salinity on the halite liquidus is described by:

$$S_{mol} = \sum_{i=0}^{3} a_i (T_{m,h} + 52)^i + a_4 \Psi^{-1} + \sum_{i=5}^{6} a_i \Psi \, (T_{m,h} + 52)^{i-3} + \sum_{i=7}^{9} a_i \Psi^2 (T_{m,h} + 52)^{i-7} + \exp(-T_{m,h} - 52) \quad (1.3)$$

Values of the fitting cofficients a_i are listed in Table 1.2. Residuals for Eqn. (1.3) are shown in Figure 1.3. In addition, the data of Zhang et al. (1995) along the NaCl-$CaCl_2$ binary are predicted by Eqn. (1.3) to within ± 4 %, even though the Zhang et al. data were not included in the regression analysis. In comparison to Eqn. (1.3), the equation of Naden (1996) for the halite liquidus surface predicts wavy isotherms with local extrema, compared to the smooth, monotonic isotherms generated using Eqn. (1.3) and shown on Fig. 1.5. The equation of Naden (1996) also does not adequately reproduce the high salinity H_2O-NaCl binary data of Sterner et al. (1988) (Fig. 1.3). Williams-Jones and Samson (1990) developed a theoretical equation to calculate halite solubility on the halite liquidus surface, and they report their results graphically as

isotherms on the ternary phase diagram. Williams-Jones and Samson (1990) do not provide an error analysis of their model, and their model cannot be compared directly to our results because they do not provide the values for the Pitzer parameters, which they obtained from graphical interpolation. However, based on visual inspection, the isotherms presented by Williams-Jones and Samson (1990) appear to be in good agreement with those predicted by our Eqn. (1.3).

1.6.4 Antarcticite field

The salinity on the antarcticite liquidus surface is described by the following relationship:

$$S_{mol} = \sum_{i=0}^{5} a_i (T_{m,ant} + 52)^i + \sum_{i=6}^{7} a_i \Psi^{i-5} (T_{m,ant} + 52)^{i-6} \qquad (1.4)$$

Residuals associated with Eqn. (1.4) are all within ± 5 % of the experimental values (Fig. 1.3). Values of the fitting parameters, a_i, are listed in Table 1.2. To our knowledge, no equations have been published previously that describe the relationship between salinity and temperature on the H_2O-NaCl-$CaCl_2$ ternary antarcticite liquidus surface.

1.6.5 Tetrahydrate and dihydrate fields

Quantitative representation of the tetrahydrate and dihydrate fields is limited by the scarcity of available experimental data; however, the narrow compositional range of these fields (Fig. 1.1c) limits the absolute error in the weight fraction of NaCl in the solution (Φ) to <0.058. The form of each of the equations for the tetrahydrate and dihydrate fields was based in part on the requirement that the cotectic and peritectic curves bounding these fields must be predicted by the intersection of the equations for the adjacent liquidus fields, because the locations of isotherms in those fields are better constrained than those in the tetrahydrate and dihydrate fields

and thus provide a means of checking the validity of the expressions for those fields. The salinity on the tetrahydrate liquidus surface is described by

$$S_{mol} = \sum_{i=0}^{2} a_i (T_{m,Ca4h} + 52)^i + \sum_{i=3}^{4} \Psi \, (T_{m,Ca4h} + 52)^{i-3} + \exp(100\Psi - 10) \tag{1.5}$$

and the salinity on the dihydrate liquidus surface is described by

$$S_{mol} = \sum_{i=0}^{3} a_i (T_{m,Ca2h} + 52)^i + a_4 \Psi \tag{1.6}$$

The a_i parameters listed in Table 1.2. Residuals of Eqn. (1.5) are all within ± 2 % of experimental values, and those for Eqn. (1.6) are within ± 3 %.

1.6.6 Comparison with data for the binary systems

The equations described above for modeling the ternary H_2O-NaCl-$CaCl_2$ system may also be used to predict liquidi for the binary H_2O-NaCl and H_2O-$CaCl_2$ systems using Eqns. (1.1) to (1.6), as shown on Figure 1.6. The predicted H_2O-NaCl eutectic (E') is at -21.18°C, compared to the experimentally determined -21.2°C (Hall et al.,1988). The predicted H_2O-NaCl peritectic point (P') is at +0.14°C, compared to the experimental value of +0.1°C (Linke, 1958). The predicted H_2O-$CaCl_2$ eutectic point (E") is at -49.9°C, compared to the experimentally determined temperature of -49.8°C (Yanatieva, 1946). The predicted first and second H_2O-$CaCl_2$ peritectic points (P_1" and P_2") are at +30.0°C and +44.7°C, compared to the experimental values of +30.1°C and +45.1°C (Linke, 1958).

While the equations developed in this study for the ternary system may also be used for the binaries, the numerical model described later offers the user the option to use previously published models for the binary systems. The equations for the binaries that may be selected include the equation of Bodnar (1993) for the ice liquidus on the H_2O-NaCl binary, the equation of Sterner et al (1988) for the halite liquidus on the H_2O-NaCl binary, and the equations of Baumgartner and Bakker (2009) for the ice, antarcticite, tetrahydrate and dihydrate liquidi on the H_2O-$CaCl_2$ binary.

1.6.7 Phase boundary curves

Each univariant curve is represented by the intersection of the adjacent divariant surfaces, rather than by a separate equation, as discussed above. For example, the liquid composition on the I+HH cotectic is represented by the intersection of the ice and hydrohalite liquidi, or in other words by the collection of T-X conditions that simultaneously satisfy Eqns. (1.1) and (1.2). Metastable extensions are not represented in this model. Residuals associated with determining the total salinity in weight percent (S_{wt}) and the weight fraction of NaCl (Φ) along the phase boundary curves by this method are shown in Figures 8 and 9, respectively. Residuals associated with salinity estimation are all within ± 4 % for the I+HH and HH+A cotectics, and within ± 6 % for the HH+H peritectic curve and H+$CaCl_2 \cdot nH_2O$ cotectics (Fig. 1.7). Percent residuals associated with estimation of Φ on the phase boundary curves are generally larger, with ± 20 % for the I+HH curve, ± 5 % for the HH+A curve, ± 60 % for the HH+H curve, and ± 50 % for the H+ $CaCl_2 \cdot nH_2O$ curves (Fig. 1.8). These large percent errors in part reflect the fact that Φ is a small number (< 1), such that small absolute errors yield large percent errors. It also reflects some scatter in the experimental data that we intentionally did not attempt to over-fit, owing to

our requirement that the phase boundary curves predicted by the equations must be smooth and monotonic.

Identifying pairs of liquidus equations that provided smooth cotectic and peritectic curves that accurately reproduced the experimental values involved some trial and error. In some cases, while the individual equations for the liquidus fields adequately reproduced data in those fields, their intersections sometimes showed significant offset in isotherms on the cotectic or peritectic curves, or did not intersect at experimentally-determined T-X conditions on these curves, or produced topologies for the curves that were not supported by experimental data. As an example, we found that the equation for the H+HH peritectic curve from Naden (1996) that describes the weight fraction of NaCl (Φ) as a function of the melting temperature of hydrohalite on the peritectic curve ($T_{pb,hh}$) is over-fitted and predicts an unrealistic curvature, whereas the intersection of Eqns. (1.2) and (1.3) from this study is comparably much smoother (Fig. 1.9). Bakker (2003) incorporated the equations of Oakes et al. (1990) and Naden (1996), without modification, into a computer package that added the option to model the univariant curves by the intersections of the adjacent liquidus surfaces (the same approach taken in this study). However, the equations of Naden (1996) for the hydrohalite and halite liquidi intersect along a wavy curve with local extrema in salinity, which causes anomalous predictions from the computer package of Bakker (2003), whereas Eqns. (1.1) and (1.3) from the present study intersect more smoothly and without extrema (Fig. 1.10).

Some structure is observable in the residuals associated with the H+$CaCl_2 \cdot nH_2O$ cotectics and the HH+A cotectic (Figs. 1.8 and 1.9). This structure could be reduced or eliminated by adjusting equations for the adjacent fields; however, this approach would then compromise the degree to which those equations for the adjacent fields would reproduce experimental data for

those fields. As such, we chose to give preference to achieving the most accurate fit on the I+HH and HH+H boundaries, because phase changes along those boundaries are reported more commonly in studies of natural fluid inclusions. Thus, we have to some extent sacrificed the fidelity with which data along the less commonly reported HH+A and H+$CaCl_2 \cdot nH_2O$ curves are reproduced. However, we believe that this approach is justified because the antarcticite, tetrahydrate and dihydrate fields encompass a very narrow range of weight fraction NaCl ($\Phi <$ 0.05), and the liquid salinity on each of those liquidi surfaces is not very sensitive to the weight fraction of NaCl. Furthermore, since Φ is always < 0.05 in this part of the system, relatively large percent errors translate into small absolute errors in the weight fraction of NaCl in the inclusion.

1.7 Methods for determining inclusion bulk compositions

The model presented here allows fluid inclusion compositions to be determined using a variety of input data, including the melting temperature of a phase on a cotectic or peritectic boundary *and* the temperature of melting of the last solid on the liquidus surface ($T_{pb,x1}$+$T_{m,x2}$), or the temperature of melting of the last solid on the liquidus surface *and* the weight ratio of NaCl in the inclusion determined from microanalysis ($T_{m,x}$+Φ), or the melting temperature of two phases on a cotectic or peritectic boundary, either melting simultaneously ($T_{pb,x1}$=$T_{pb,x2}$) or at different temperatures ($T_{pb,x1}$+$T_{pb,x2}$). The following sections describe the methodologies to determine bulk composition using the various types of input data.

1.7.1 Final melting on a cotectic curve ($T_{pb,x1}$=$T_{pb,x2}$, two solid phases dissolve simultaneously)

In the simplest case where two solids dissolve simultaneously on a cotectic curve, the bulk composition is uniquely specified by the melting temperature in accordance with the phase rule. The measured melting temperature can be used to calculate the fluid inclusion composition

by solving for the intersection of the adjacent surfaces at that temperature, in other words by finding the value of the weight fraction of NaCl (Φ) for which the two adjacent liquidus surface salinity equations yield the same salinity at the measured temperature of melting. For example, consider a fluid inclusion in which ice and hydrohalite dissolve simultaneously at -25°C. The salinity in the ice field at -25°C and a given weight fraction of NaCl (Φ) can be found from Eqn. (1.1), while the salinity in the hydrohalite field at -25°C and Ψ can be estimated from Eqn. (2). By iteration, we find that a weight fraction of NaCl, Φ, of 0.57 yields a liquid salinity of 24.7 wt.% at -25°C in both Eqns. (1.1) and (1.2). Thus, the intersection of the ice and hydrohalite liquidus surfaces occurs at a salinity of 24.7 wt.% (NaCl + $CaCl_2$) and a weight fraction of NaCl of 0.57, and this represents the bulk composition of the fluid inclusion.

1.7.2 Last melting temperature ($T_{m,x}$) and NaCl weight fraction (Φ)

If available data include the melting temperature of the last solid obtained from microthermometry, and the weight fraction of NaCl (Φ) determined by microanalysis (e.g., LA-ICPMS), the fluid bulk composition is determined by finding the intersection of the isotherm of the final melting temperature with the pseudobinary defined by the NaCl weight fraction (Φ). Those two variables may be input directly into the appropriate equation (with Φ converted to Ψ where required). As an example, consider a fluid inclusion that contains a halite daughter mineral that dissolves at 200°C, and has a weight fraction of NaCl relative to NaCl + $CaCl_2$ (Φ) of 0.7 based on LA-ICPMS analysis of the inclusion. Φ of 0.7 equals a molar fraction, Ψ, of 0.815, and substituting those values of Ψ (0.815) and $T_{m,h}$ (200°C) into Eqn. (1.3) yields a total salinity on a mole fraction basis, S_{mol}, of 0.116, which corresponds to a total salinity of 33.1 wt.%.

1.7.3 Two unique melting temperatures, $T_{pb,x1}$+$T_{m,x2}$ or $T_{pb,x1}$+$T_{pb,x2}$

If available data include two unique melting temperatures from microthermometry – either a cotectic (or peritectic curve) melting temperature ($T_{pb,x1}$) plus the temperature of melting of the last solid phase on the liquidus ($T_{m,x2}$), or a cotectic melting temperature ($T_{pb,x1}$) plus a univariant peritectic melting temperature ($T_{pb,x2}$) – various calculation procedures may be used depending on which solid phases and phase changes are involved. On Figure 1.11, the ternary system is divided into several numbered fields that identify compositions within the H_2O-NaCl-$CaCl_2$ ternary that involve the same phase changes as input data or follow similar calculation procedures.

1.7.4 Field 1 – $T_{pb,hh} < T_{m,ice}$

During heating from the eutectic temperature, fluids with compositions in field 1 lose hydrohalite along the I+HH cotectic and ice is the last solid phase to melt on the ice liquidus surface. The composition of the liquid at the temperature of hydrohalite dissolution on the cotectic is determined from the intersection of the hydrohalite and ice liquidi at the temperature of hydrohalite melting ($T_{pb,hh}$), from Eqns. (1.1) and (1.2). After hydrohalite disappears, because the last remaining solid is pure H_2O ice (solid solution between solid phases in this system is negligible), the weight fraction of NaCl (Φ) of the liquid phase does not change during continued heating and ice melting, and the liquid composition moves directly towards the H_2O apex. Thus, the weight fraction of NaCl (Φ) determined from the temperature of hydrohalite melting on the cotectic and the final ice melting temperature ($T_{m,ice}$), can be input directly into Eqn. (1.1) to determine the bulk salinity.

1.7.5 Field 2 – $T_{pb,ant}<T_{m,ice}$

The calculation procedure to determine the composition of fluids that exhibit antarcticite dissolution on the I+A cotectic, followed by final melting of ice on the ice liquidus surface is analogous to that for fluids in field 1, substituting $T_{pb,ant}$ for $T_{pb,hh}$, and substituting Eqn. (1.4) for Eqn. (1.2)..

1.7.6 Field 3 – $T_{pb,ice}<T_{m,hh}$

For fluid inclusions in which ice is the phase that disappears along the I+HH cotectic and which subsequently show hydrohalite as the last solid to melt on the hydrohalite liquidus, the liquid composition at the temperature of ice melting on the I+HH cotectic is determined from the intersections of Eqns. (1.1) and (1.2), as described previously for field 1. After ice melts on the ice-hydrohalite cotectic curve, with further heating the liquid composition evolves along a straight line extending from the composition of the liquid at $T_{pb,ice}$ to the composition of hydrohalite (61.86 wt.% NaCl). The intersection of that line with the isotherm of hydrohalite dissolution yields the unique bulk fluid composition. As an example, consider a fluid inclusion in which ice melts on the I+HH cotectic at -25°C and hydrohalite is the last solid to melt at -10°C. At the last ice melting temperature, the liquid contains 14.3 wt.% NaCl and 10.4 wt.% $CaCl_2$, from the intersection of Eqns. (1.1) and (1.2) at $T_{pb,ice}$ = -25°C. The fluid inclusion bulk composition lies on a mixing line between the composition of the liquid on the I+HH cotectic and the composition of hydrohalite. The equation of the mixing line can be determined using the slope and intercept method, where the *x*- and *y*-axes are wt.% NaCl and wt.% $CaCl_2$, respectively, and the input *xy* coordinates are the compositions of liquid (14.3 wt.% NaCl, 10.4 wt.% $CaCl_2$) and hydrohalite (61.9 wt.% NaCl, 0 wt.% $CaCl_2$). The equation of this line (in *xy* coordinates) is also the equation of the vertical plane containing the line (in *xyz* coordinates,

where the *z*-axis is temperature), because the linear equation of the mixing line is independent of temperature. Thus by iteratively solving for the pair of values of wt.% NaCl and wt.% $CaCl_2$ that satisfy both this linear equation and Eqn. (1.2), we find the bulk composition. In our example, a composition of 16.4 wt.% NaCl and 9.9 wt.% $CaCl_2$ satisfies both equalities, and is thus the bulk fluid composition of the inclusion.

1.7.7 Field 4 – $T_{pb,ant}<T_{m,hh}$

For fluid inclusions that exhibit antarcticite melting in the presence of hydrohalite along the HH+A cotectic, followed by hydrohalite final melting, the calculation procedure is analogous to that for field 3, the only difference being that $T_{pb,ant}$ is substituted for $T_{pb,hh}$, and the liquid composition on the HH+A boundary is determined from the intersections of Eqns. (1.2) and (1.5).

1.7.8 Field 5 – $T_{pb,hh}<T_{m,h}$

Fluid inclusions that have compositions within field 5 show halite as the last solid phase to melt, and hydrohalite as the next-to-last solid phase to melt. The calculation procedure for fluid inclusion compositions in this field depends on the input data that are available.

For fluid inclusions in field 5 with compositions to the high-salinity side of the line extending from $CaCl_2 \cdot 6H_2O$ to $NaCl \cdot 2H_2O$ (Figs. 1.1 and 1.11) (field 5a), the sub-solidus assemblage is halite+hydrohalite+antarcticite, and first melting occurs at the first peritectic P_1 (Fig. 1.1). At this temperature (-22.4°C), antarcticite is consumed and the liquid composition subsequently evolves along the HH+H peritectic curve, until hydrohalite is consumed at $T_{pb,hh}$. The liquid composition at $T_{pb,hh}$ is determined from the intersection of Eqns. (1.2) and (1.3). The

liquid composition on the peritectic curve is recast in terms of the molar proportion of $CaCl_2$ relative to $CaCl_2$+H_2O (Ω) according to:

$$\Psi' = \frac{S_{mol} - S_{mol}\Psi_{mol}}{1 - S_{mol}\Psi_{mol}} \tag{1.7}$$

Upon departure from the HH+H peritectic curve, the value of Ω of the liquid remains constant with further heating, as the liquid composition evolves along a straight line towards the NaCl apex. The fluid inclusion bulk composition is found as the intersection of the vertical plane containing that line of constant Ω with the isotherm of final halite melting.

For fluid inclusions in field 5 that lie within the ice-hydrohalite-antarcticite triangle (fields 5b and 5c) (Fig. 1.11), first melting occurs at the eutectic and the liquid composition evolves along either the HH+A or HH+I curve until either ice or antarcticite is consumed, after which the liquid composition evolves across the hydrohalite field along a straight line towards the composition of hydrohalite. Upon intersecting the HH+H peritectic curve, halite nucleates and the liquid composition evolves along the HH+H curve until hydrohalite is consumed. The liquid composition then evolves along a straight line towards the NaCl apex with further heating until halite is completely consumed. For each of the fields 5b and 5c, there are thus three melting temperatures that may be observed and recorded ($T_{pb,ice}$ (or $T_{pb,ant}$) + $T_{pb,hh}$ + $T_{m,h}$), and any pair of these is sufficient to fix the bulk fluid composition. Vanko et al. (1988) describe the methods by which either pair of these data may be used to determine the fluid bulk composition. If the data available are $T_{pb,hh}$ and $T_{m,h}$, the method used to calculate the inclusion composition is the same as outlined above for field 5a. However, as discussed by Roedder (1984) and Vanko et al. (1988), the final melting of hydrohalite can be difficult to observe, and hydrohalite may persist

metastably for several degrees Celsius above the equilibrium melting temperature. For those reasons, it is sometimes more practical to measure $T_{pb,ice}$+$T_{m,h}$ (Vanko et al., 1988). In that case, the liquid composition is determined at $T_{pb,ice}$ using Eqns. (1.1) and (1.2), and the equation of the straight line that extends from the cotectic liquid composition at $T_{pb,ice}$ to the composition of hydrohalite (as described above for field 3) (Fig. 1.12). The intersection of the vertical plane containing that line with the isotherm of $T_{m,h}$ on the halite liquidus (Eqn. (1.3)) represents the bulk fluid composition (Vanko et al., 1988) (Fig. 1.12).Fluid inclusions with compositions in field 5c are treated in a similar manner to those in field 5b, substituting $T_{pb,ant}$ for $T_{pb,ice}$, and substituting Eqn. (1.4) for Eqn. (1.1).

1.7.9 Field 6 – $T_{pb,ant,\ Ca4h\ or\ Ca2h} < T_{m,h}$

The calculation method for fluid inclusions that exhibit cotectic melting of one of the three $CaCl_2$ hydrates in the presence of halite, followed by halite dissolution as the last solid phase, is similar for each of the three halite+$CaCl_2 \cdot nH_2O$ cotectics. Field 6a includes fluid inclusion compositions for which antarcticite disappears on the H+A cotectic, field 6b includes those that lose tetrahydrate along the H+Ca4h cotectic, and field 6c includes those that lose dihydrate on the H+Ca2h cotectic. The method employed for each of these fields is to determine the liquid composition (Ω) on the cotectic at the temperature of last hydrate melting from the intersection of Eqn (1.3) with either Eqn. (1.4), Eqn. (1.5) or Eqn. (1.6) (depending on the last hydrate to melt). The fluid inclusion bulk composition is found as the intersection of the vertical plane containing the line of constant Ω with the isotherm of final halite melting ($T_{m,h}$).

1.7.10 Field 7 – $T_{pb,x}<T_{m,ant}$, Ca4h or Ca2h

Field 7 includes a narrow compositional range near the $CaCl_2$ binary, and is characterized by at least seven possible melting sequences and pairs of input data, although observation of melting sequences in this part of the system has yet to be reported unequivocally for natural fluid inclusions.

Because the weight fraction of NaCl (Φ) in this part of the system is everywhere less than 0.05, the fluid bulk composition can be estimated with reasonable precision from $T_{m,CaCl2\cdot nH2O}$ alone. The liquid Φ on the appropriate cotectic or peritectic curve can be determined directly as outlined for the other fields, by the intersection of the adjacent liquidi, and the bulk composition lies on the straight line that extends from that composition to the composition of the final melting of solid $CaCl_2$ hydrate. Again, the weight fraction of NaCl (Φ) in the bulk fluid in this part of the system does not significantly affect the calculated total salinity and, in the absence of a next-to-last melting temperature, Φ must be between 0-0.05.

1.8 References

Bakker, R. J., 2003. Package FLUIDS; 1, Computer programs for analysis of fluid inclusion data and for modelling bulk fluid properties. *Chemical Geology* **194**, 3-23.

Basuki, N. I., Spooner, E. T. C., 2002. A review of fluid inclusion temperatures and salinities in Mississippi valley-type Zn-Pb deposits; identifying thresholds for metal transport. *Exploration and Mining Geology* **11**, 1-17.

Baumgartner, M., Bakker, R. J., 2009. $CaCl_2$-hydrate nucleation in synthetic fluid inclusions. *Chemical Geology* **265**, 335-344.

Bodnar, R. J., 1993. Revised equation and table for determining the freezing point depression of H_2O-NaCl solutions. *Geochimica et Cosmochimica Acta* **57**, 683-684.

Bodnar, R. J., 1994. Synthetic fluid inclusions; XII, The system H_2O-NaCl; experimental determination of the halite liquidus and isochores for a 40 wt% NaCl solution. *Geochimica et Cosmochimica Acta* **58**, 1053-1063.

Chi, G., Ni, P., 2007. Equations for calculation of NaCl/(NaCl + $CaCl_2$) ratios and salinities from hydrohalite-melting and ice-melting temperatures in H_2O-NaCl-$CaCl_2$ system. *Yanshi Xuebao* **23**, 33-37.

Chou, I-Ming, 1987. Phase relations in the system NaCl-KCI-H_2O. Part III: Solubilities of halite in vapor-saturated liquids above 445°C and redetermination of phase equilibrium properties in the system NaCl-H_20 to 1000°C and 1500 bars. *Geochimica et Cosmochimica Acta **51**, 1965-1975.*

Collins, A. G., 1975. *Geochemistry of oilfield waters*. Elsevier Scientific Publishing Company, Amsterdam; New York.

Dubessy, J., Audeoud, D., Wilkins, R., Kosztolanyi, C., 1982. The use of the Raman microprobe MOLE in the determination of the electrolytes dissolved in the aqueous phase of fluid inclusions. *Chemical Geology* **37**, 137-150.

Frape, S. K., Fritz, P., McNutt, R. H., 1984. Water-rock interaction and chemistry of groundwaters from the Canadian Shield. *Geochimica et Cosmochimica Acta* **48**, 1617-1627.

Günther, D., Audétat, A., Frischknecht, R., Heinrich, C. A., 1998, Quantitative analysis of major, minor and trace elements in fluid inclusions using laser ablation - inductively coupled plasma mass spectrometry: *Journal of Analytical Atomic Spectroscopy* **13**, p. 263-270.

Hall, D.L., Sterner, S.M., Bodnar, R.J., 1988, Freezing point depression of NaCl-KCl-H_2O solutions. *Economic Geology* **83**, 197-202.

Hanor, J. S., McIntosh, J. C., 2007. Diverse origins and timing of formation of basinal brines in the Gulf of Mexico sedimentary basin. *Geofluids* **7**, 227-237.

Haynes, F. M., Kesler, S. E., 1987. Chemical evolution of brines during Mississippi valley-type mineralization; evidence from East Tennessee and Pine Point. *Economic Geology* **82**, 53-71.

Konnerup-Madsen, J., 1979. Fluid inclusions in quartz from deep-seated granitic intrusions, south Norway. *Lithos* **12**, 13-23.

Kwak, T. A. P., Tan, T. H., 1981. The importance of $CaCl_2$ in fluid composition trends; evidence from the King Island (Dolphin) skarn deposit. *Economic Geology* **76**, 955-960.

Layne, G. D., Spooner, E. T. C., 1991. The JC tin skarn deposit, southern Yukon Territory; I, Geology, paragenesis, and fluid inclusion microthermometry. *Economic Geology* **86**, 29-47.

Li, C., Naldrett, A. J., 1993. High chlorine alteration minerals and calcium-rich brines in fluid inclusions from the Strathcona deep copper zone, Sudbury, Ontario. *Economic Geology* **88**, 1780-1796.

Linke, W. F., 1958. *Solubilities, inorganic and metal organic compounds; a compilation of solubility data from the periodical literature*. Van Nostrand, Princeton, NJ.

Lowenstein, T. K., Hardie, L. A., Timofeeff, M. N., Demicco, R. V., 2003. Secular variation in seawater chemistry and the origin of calcium chloride basinal brines. *Geology* **31**, 857-860.

Naden, J., 1996. CalcicBrine; a Microsoft Excel 5.0 add-in for calculating salinities from microthermometric data in the system NaCl-$CaCl_2$-H_2O. In: Brown, P. E. and Hagemann, S. G. Eds.) *PACROFI VI Extended Abstracts*, Madison, WI.

National Research Council, 1928. *International critical tables of numerical data, physics, chemistry and technology*. McGraw-Hill, New York.

Nyman, M. W., Sheets, R. W., Bodnar, R. J., 1990. Fluid-inclusion evidence for the physical and chemical conditions associated with intermediate-temperature PGE mineralization at the New Rambler Deposit, southeastern Wyoming. *The Canadian Mineralogist* **28**, 629-638.

Oakes, C. S., Bodnar, R. J., Simonson, J. M., 1990. The system NaCl-$CaCl_2$-H_2O; 1, The ice liquidus at 1 atm total pressure. *Geochimica et Cosmochimica Acta* **54**, 603-610.

Oakes, C. S., Sheets, R. W., Bodnar, R. J., 1992. (NaCl + $CaCl_2$)[aq]; phase equilibria and volumetric properties. In: Hall, D. S. and Sterner, S. M. Eds.) *PACROFI IV Extended Abstracts*, Lake Arrowhead, CA.

Potter, R. W., Clynne, M. A., 1978. Solubility of highly soluble salts in aqueous media; Part 1, NaCl, KCl, $CaCl_2$, Na_2SO_4 , and K_2SO_4 solubilities to 100°C. *Journal of Research of the U. S. Geological Survey* **6**, 701-705.

Robert, F., Kelly, W. C., 1987. Ore-forming fluids in Archean gold-bearing quartz veins at the Sigma Mine, Abitibi greenstone belt, Quebec, Canada. *Economic Geology* **82**, 1464-1482.

Roedder, E., 1967. Metastable superheated ice in liquid water inclusions under high negative pressure. *Science* **155**, 1412-1417.

Roedder, E., 1984. Fluid inclusions. *Reviews in Mineralogy* **12**, 644.

Samson, I. M., Walker, R. T., 2000. Cryogenic Raman spectroscopic studies in the system NaCl-$CaCl_2$-H_2O and implications for low-temperature phase behavior in aqueous fluid inclusions. *The Canadian Mineralogist* **38**, 35-43.

Samson, I. M., Williams-Jones, A. E., Ault, K. M., Gagnon, J. E., Fryer, B. J. (2008). Source of fluids forming distal Zn-Pb-Ag skarns: Evidence from laser ablation-inductively coupled plasma-mass spectrometry analysis of fluid inclusions from El Mochito, Honduras. *Geology* **36**, 947-950.

Schiffries, C. M., 1990. Liquid-absent aqueous fluid inclusions and phase equilibria in the system $CaCl_2$-NaCl-H_2O. *Geochimica et Cosmochimica Acta* **54**, 611-619.

Sterner, S. M., Hall, D. L., Bodnar, R. J., 1988. Synthetic fluid inclusions. V. Solubility relations in the system NaCl-KCl-H_2O under vapor-saturated conditions. *Geochimica et Cosmochimica Acta* **52**, 989-1005.

Stoffell, B., Appold, M. S., Wilkinson, J. J., McClean, N. A. Jeffries, T. E. (2008). Geochemistry and evolution of Mississippi valley-type mineralizing brines from the Tri-State and

Northern Arkansas Districts determined by LA-ICP-MS microanalysis of fluid inclusions. *Economic Geology* **103**, 1411-1435.

Ulmer-Scholle, D. S., Scholle, P. A., Brady, P. V., 1993. Silicification of evaporites in Permian (Guadalupian) back-reef carbonates of the Delaware Basin, West Texas and New Mexico. *Journal of Sedimentary Petrology* **63**, 955-965.

Vanko, D. A., 1988. Temperature, pressure, and composition of hydrothermal fluids, with their bearing on the magnitude of tectonic uplift at mid-ocean ridges, inferred from fluid inclusions in oceanic layer 3. *Journal of Geophysical Research* **93**, 4595-4611.

Vanko, D. A., Bodnar, R. J., Sterner, S. M., 1988. Synthetic fluid inclusions; VIII, Vapor-saturated halite solubility in part of the system NaCl-$CaCl_2$-H_2O, with application to fluid inclusions from oceanic hydrothermal systems. *Geochimica et Cosmochimica Acta* **52**, 2451-2456.

Williams-Jones, A. E., Samson, I. M., 1990. Theoretical estimation of halite solubility in the system NaCl-$CaCl_2$-H_2O; applications to fluid inclusions. *The Canadian Mineralogist* **28**, 299-304.

Xu, G., 2000. Fluid inclusions with NaCl-$CaCl_2$-H_2O composition from the Cloncurry hydrothermal system, NW Queensland, Australia. *Lithos* **53**, 21-35.

Yanatieva, O. K., 1946. Solubility polytherms in the systems $CaCl_2$-$MgCl_2$-H_2O and $CaCl_2$-NaCl-H_2O. *Zhurnal Prikladnoi Khimii* **19**, 709-22.

Zhang, Y., Han, Y., Wang, S, 1995. Phase diagram of the ternary system $SmCl_3$-NaCl-$CaCl_2$. *Thermochimica Acta* **254**, 383-90.

1.9 Tables

Table 1.1. Summary of the number of published experimental T-X data points for the H_2O-NaCl-$CaCl_2$ system used in this study.

	Solid phase(s) on cotectic and peritectic curves and on liquidus surfaces[a]											
Source	I+HH	I+A	HH+H	HH+A	H+A	H+Ca2h	I	HH	H	A	Ca4h	Ca2h
National Research Council (1928)									19			
Yanatieva (1946)	9	3	6	7	8		57	30	13	20		
Linke (1958)			4		1	2	21	1	57	15	7	12
Potter and Clynne (1978)									11	4	5	5
Vanko et al. (1988)									10			
Oakes et al. (1990)	1						168					
Oakes et al. (1992)	3											
Sterner et al. (1988)									8			
Sub-total							246	31	118	39	12	17
Total[b]	13	3	10	7	9	2	262	61	137	58	12	19

(a) I = ice; HH = hydrohalite; H = halite; A = antarcticite; Ca4h = tetrahydrate; Ca2h = dihydrate
(b) For each one-solid liquidus surface, the total number of data points used in the regression analysis is the sum of the subtotal (data on the one-solid surface) plus the number of data points for the adjacent boundary curves.

Table 1.2. Coefficients for Equations 1.1-1.6.

a_i	Ice (Eqn. 1)	Hydrohalite (Eqn. 2)	Halite (Eqn. 3)	Antarcticite (Eqn. 4)	Tetrahydrate (Eqn. 5)	Dihydrate (Eqn. 6)
a_0	0.46685	0.06039097042	0.0586472647	0.06467408472	1.041627135	0.096475342
a_1	-2.0508125	-2.967800E-5	2.2759389E-4	6.9903747E-4	-0.02232533	1.677838E-3
a_2	-0.08997493	7.0463278E-6	0	-2.607825E-5	1.3792920E-4	-1.3572629E-5
a_3	-2.5468641E-3	1.237133E-3	8.8841217E-9	1.0162876E-6	-2.95841861	4.5571671E-8
a_4	-3.7319837E-5	-1.290978E-3	1.2272697E-3	4.3288357E-9	0.032785047	-0.11534086
a_5	-2.1478861E-7	-5.219129E-3	-3.9989511E-6	1.1648119E-10		
a_6	-1.138304	-3.178747E-6	-6.680437E-9	0.06779525838		
a_7	0.269882	-1.408898E-7	0.0284636532	-1.0833486E-3		
a_8	6.8878422E-3	1.0353807E-3	0			
a_9	1.37774273E-8		3.1094576E-6			

1.10 Figures

Figure 1.1. Vapor-saturated liquidus phase relations in the H_2O-NaCl-$CaCl_2$ system. (a) A distorted, schematic representation of the ternary H_2O-NaCl-$CaCl_2$ system showing the relative locations of the liquidus fields. (b) The shaded region on the ternary diagram shows the part of the system that is modeled in this study. The numbered triangles show fields of sub-solidus phase assemblages. Bulk compositions within triangle "1" contain the equilibrium assemblage ice+hydrohalite+antarcticite when frozen; those in triangle "2" contain hydrohalite+halite+antarcticite when frozen; and those compositions in triangle "3" contain halite+antarcticite+tetrahydrate when frozen. (c) Phase boundaries (cotectic and peritectic curves) and isotherms calculated using the equations developed in this study (see text for discussion). The invariant points and univariant curves are labeled according to the terminology described in the text. Arrows on the univariant curves point up-temperature.

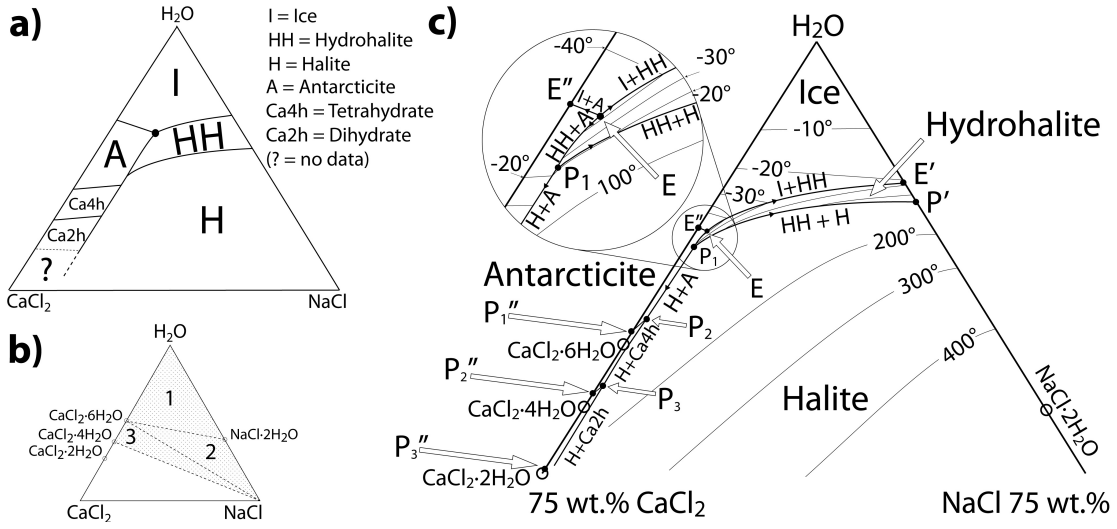

Figure 1.2. Summary of experimental data for the H_2O-NaCl-$CaCl_2$ system used in this study. The data are sorted according to the phase assemblage on the vapor-saturated liquidus, and the source of the data (see the legend). The phase boundary curves were calculated from the equations derived in this study (described in detail in the text).

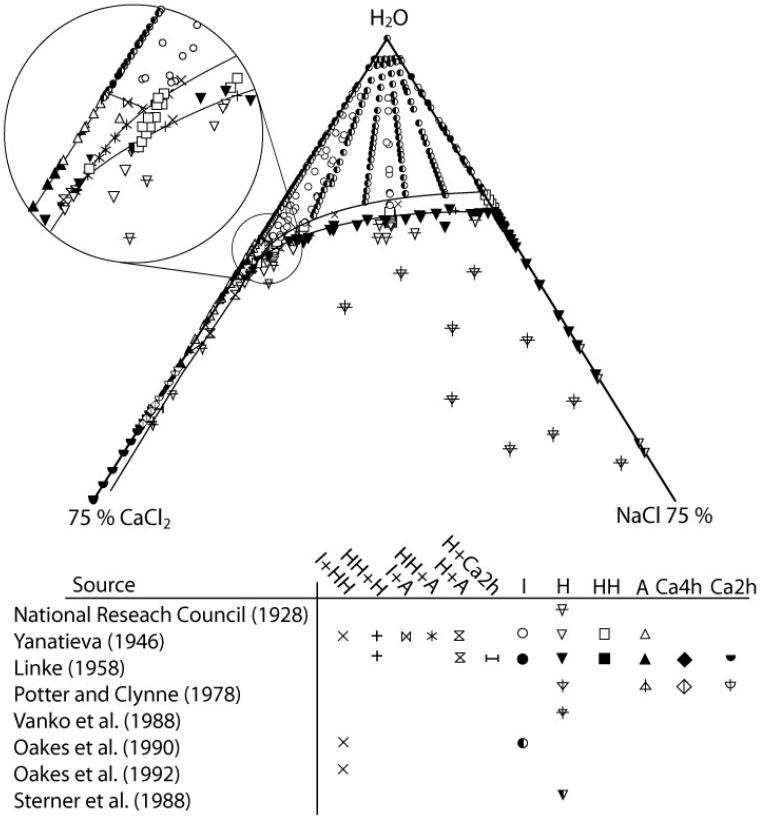

Figure 1.3. Residuals, in percent difference between experimental and calculated values. Residuals are expressed by the formula {(1 - calculated/measured)*100%}, associated with the liquid salinity on the vapor-saturated liquidi of ice (a), hydrohalite (b), halite (c) and antarcticite (d) as a function of the melting temperature of the last solid on the liquidus ($T_{m,x}$) and the weight ratio of NaCl relative to NaCl + $CaCl_2$ (Φ) calculated from Eqns. (1) to (4), plotted against the experimental salinity. The symbols used for the residuals correspond to the equation used and the source of experimental values to which the predicted values are compared (see the legend).

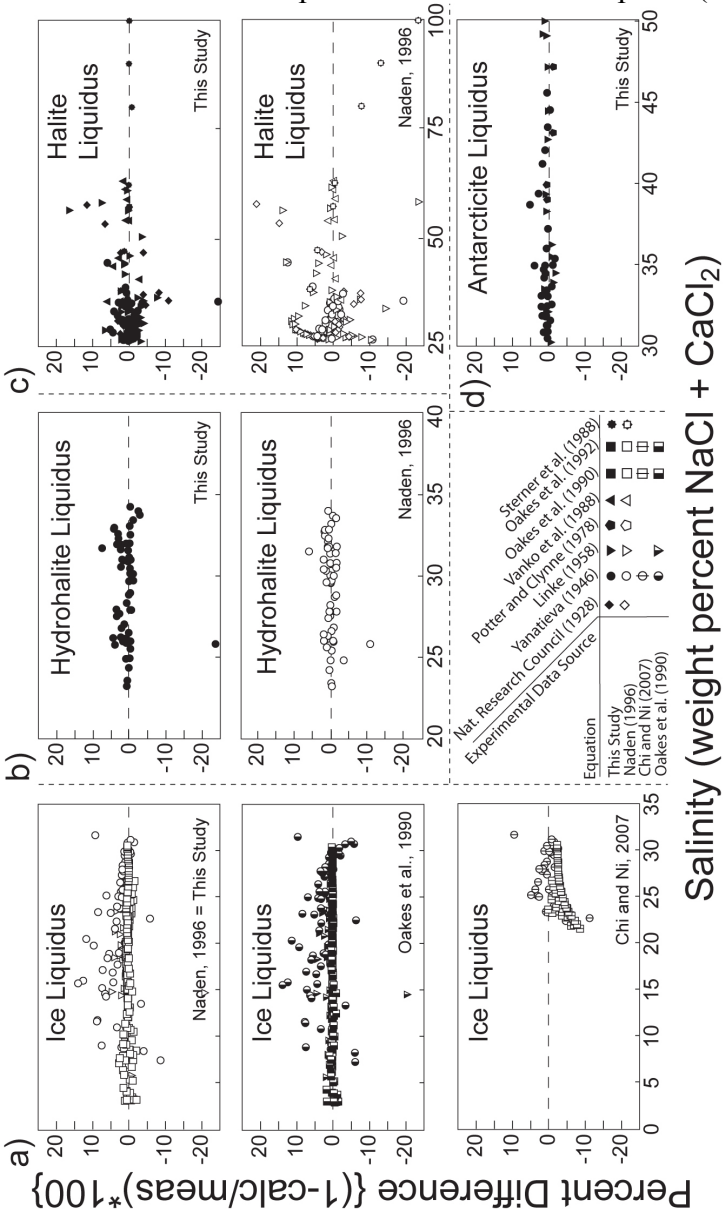

Figure 1.4. Comparison of the composition (salinity vs. NaCl weight ratio) on the -10°C isotherm on the vapor-saturated hydrohalite liquidus predicted by the equation of NADEN (1996) (dashed line) and by equation (1.4) from this study (solid line).
Experimental data on the -10°C isotherm from Yanatieva (1946) are shown as open circles.

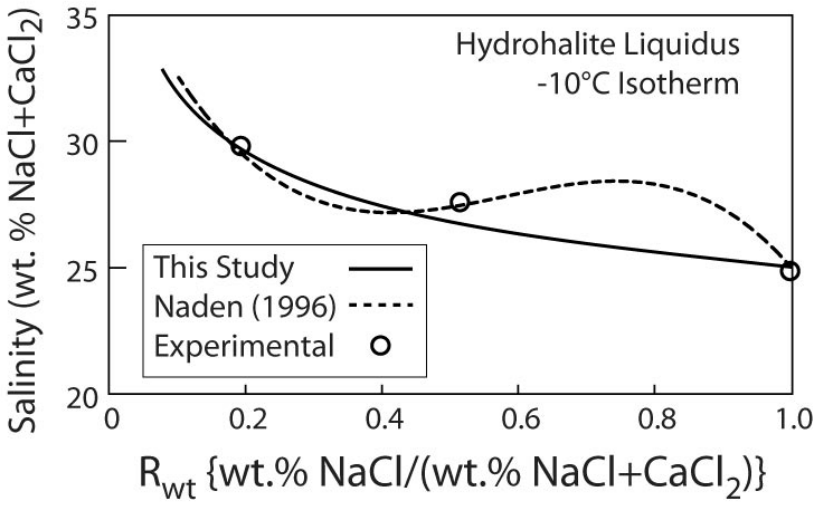

Figure 1.5. Comparison of the salinity on the +94.5°C isotherm on the vapor-saturated halite liquidus predicted by the equation of Naden (1996) (dashed line) and by equation (1.5) from this study (solid line).
Experimental data on the +94.5°C isotherm from the National Research Council (1928) are shown as open circles. These experimental data were chosen for comparison because of the large number of data points extending over a wide range of compositions along the +94.5°C isotherm in the NRC report.

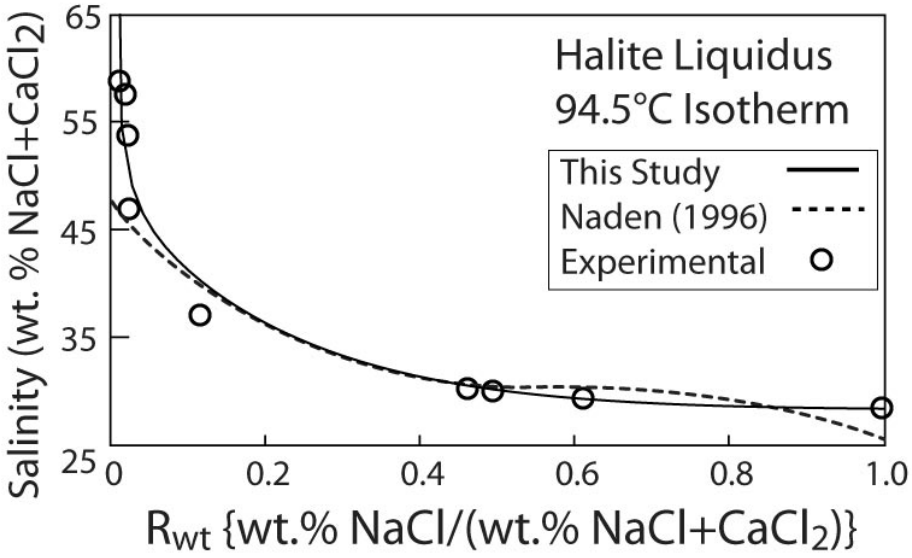

Figure 1.6. Liquidus curves for the H_2O-NaCl *(top)* and H_2O-$CaCl_2$ *(bottom)* binary systems, calculated from Eqns. (1) to (6).
Experimental data are from National Research Council (1928) (halite); Yanatieva (1946) (ice, hydrohalite, halite, antarcticite); Linke (1958) (ice, hydrohalite, halite, antarcticite, tetrahydrate, dihydrate); Potter and Clynne (1978) (halite, antarcticite, tetrahydrate, dihydrate); Sterner et al. (1988) (halite); and Oakes et al. (1990) (ice).

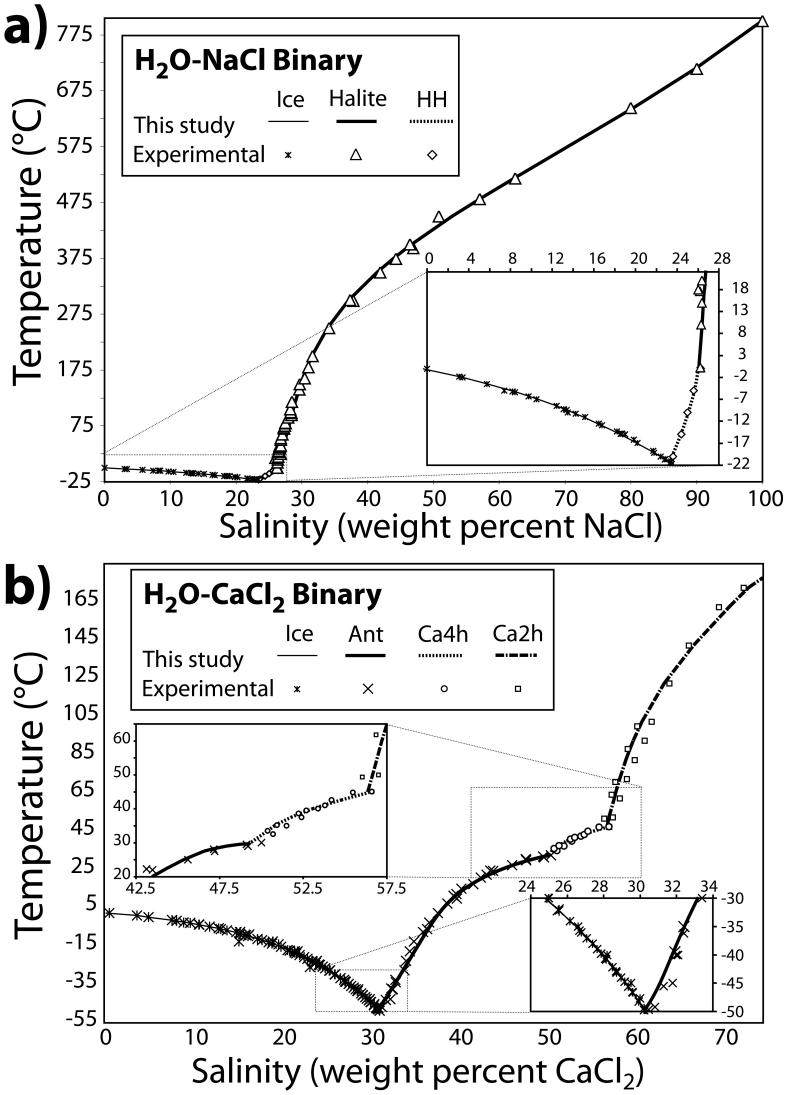

Figure 1.7. Residuals of salinity on the univariant curves.
Residuals are expressed in percent difference between experimental and calculated values {(1 - calculated/measured)*100%}, associated with liquid salinity on the I+HH, HH+H, HH+A and H+$CaCl_2$·*n*H_2O phase boundary curves as a function of temperature from Eqns. (1), (2), (3), (4) and (6), plotted against the experimental salinity. Symbols used are the same as for Figure 1.3.

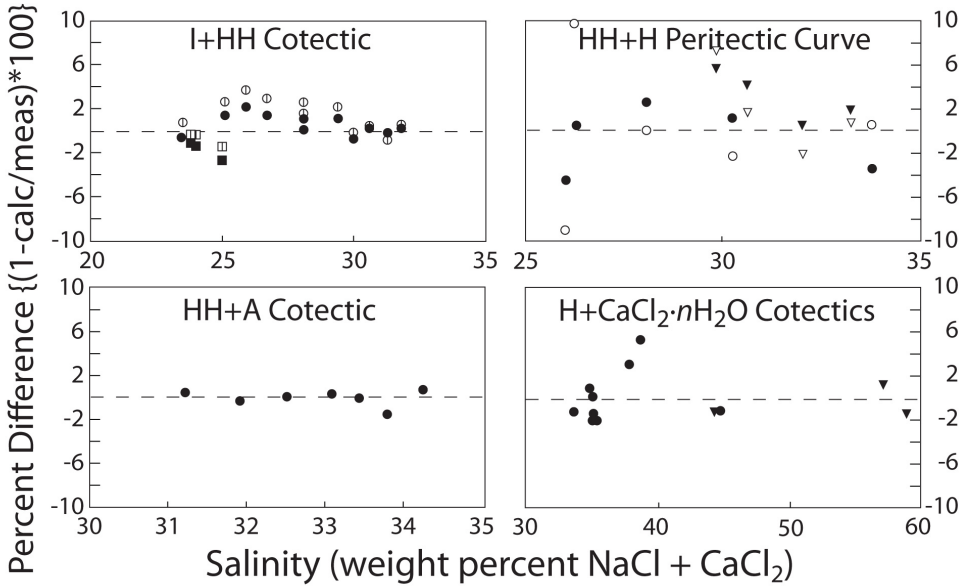

Figure 1.8. Residuals of salt ratios on the univariant curves.
Residuals are expressed as percent difference between experimental and calculated values {(1 - calculated/measured)*100%}, associated with Φ on the I+HH, HH+H, HH+A and H+$CaCl_2$·nH_2O phase boundary curves as a function of temperature from Eqns. (1), (2), (3), (4) and (6), plotted against the experimental weight fraction of NaCl (Φ). The dashed vertical line in the I+HH residuals plot (upper left) shows the eutectic composition. Symbols used are the same as for Figure 1.3.

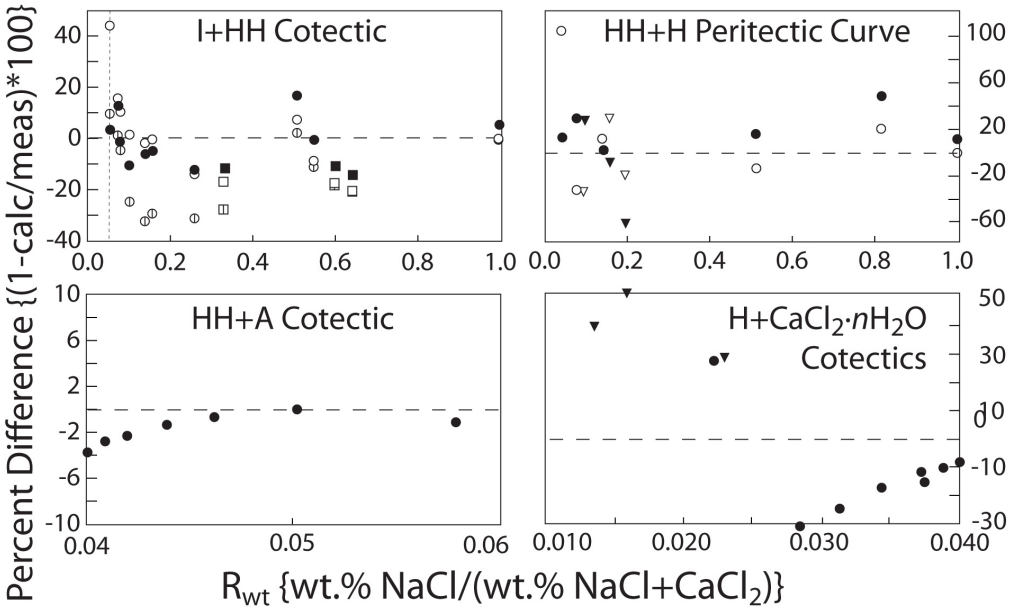

Figure 1.9. Salt ratios on the HH+H peritectic curve.
Comparison of the weight fraction of NaCl in the liquid (Φ) as a function of temperature on the HH+H peritectic curve predicted by the equation of Naden (1996) (dashed line) and by the intersection of equations (1.4) and (1.5) from this study (solid line). Experimental data (solid triangles) are from Yanatieva (1946) and Linke (1958).

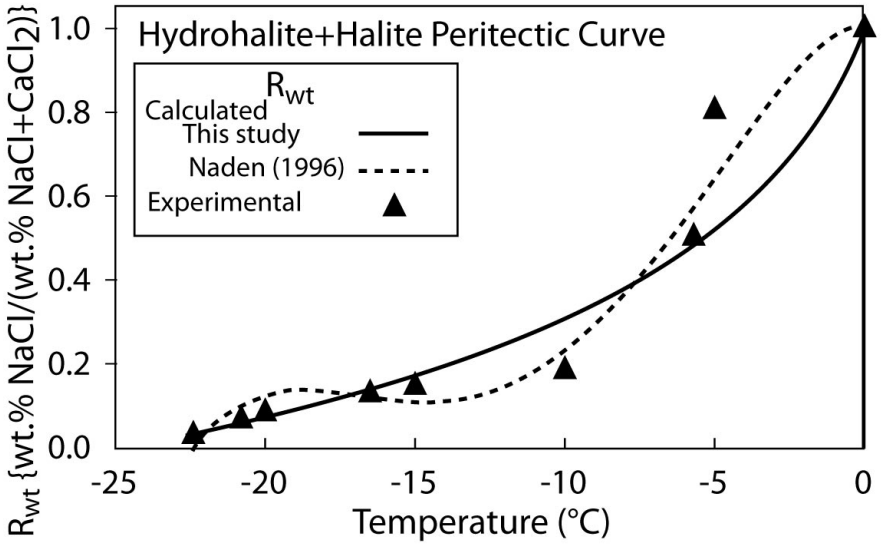

Figure 1.10. Liquid salinity on the HH+H curve from this study and previous studies. Comparison of the liquid salinity as a function of temperature on the HH+H peritectic curve predicted by the method of intersection of adjacent liquidus surfaces from Naden (1996), implemented by Bakker (2003) (dashed line) and by the Equations (1.4) and (1.5) from this study (solid line). Experimental data (solid triangles) are from Yanatieva (1946) and Linke (1958).

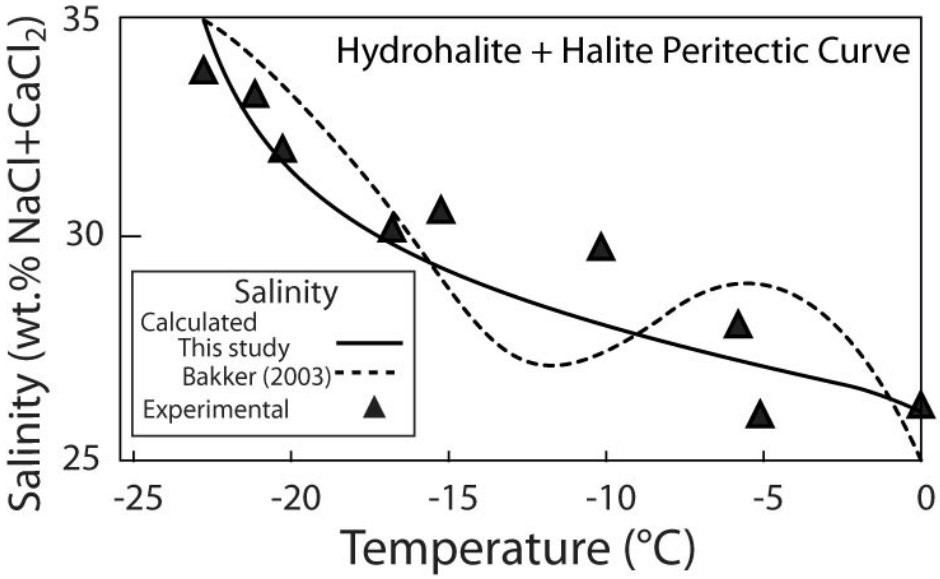

Figure 1.11. Phase diagram for H_2O-NaCl-$CaCl_2$ fluids divided into regions based on melting sequence.

Phase relations in the H_2O-NaCl-$CaCl_2$ system under vapor-saturated conditions showing the eleven different fluid inclusion composition fields, based on the sequence and temperatures of the final two (or three) solids to melt during heating. See text for discussion of phase changes corresponding to each field and identification of symbols.

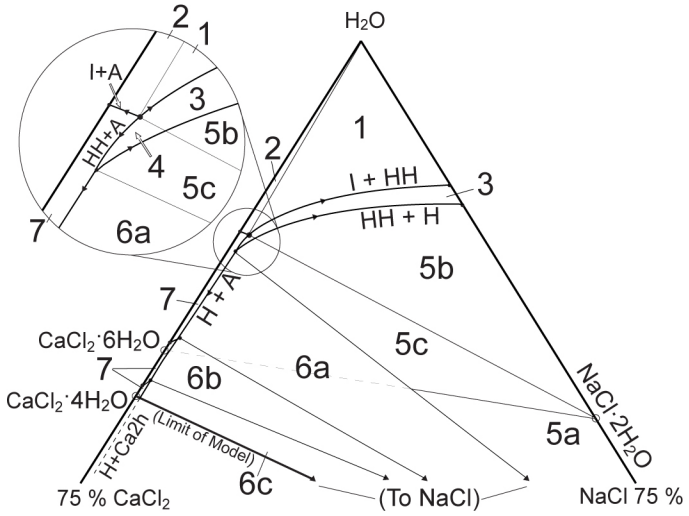

Figure 1.12. Example heating sequence for a halite-bearing fluid inclusion.
Schematic heating sequence for a fluid inclusion with a composition within field 5b (Fig. 1.11), showing the melting events that may be observed during microthermometry. Isotherms of the relevant phase changes are shown as dotted lines. Antarcticite is lost at the eutectic (point "E"), . The liquid composition then evolves along the I+HH cotectic with further heating until ice is consumed at point "a" ($T_{pb,ice}$). At this point, because hydrohalite is the only solid phase present, the liquid composition evolves along a straight line towards the composition of hydrohalite with further heating (segment a→b). The HH+H curve is intersected at point "b," where halite nucleates ($T_{pb,hh*}$). On further heating, the liquid composition evolves along the HH+H peritectic curve (segment b→c), until hydrohalite is consumed at point "c" ($T_{pb,hh}$). At this point, halite is the only remaining solid phase, so with further heating the liquid composition evolves towards the NaCl apex until intersecting the $T_{m,h}$ isotherm at point "d," which is the bulk fluid inclusion composition. Note that the bulk composition lies along the mixing line "a-NaCl·2H_2O" (between the liquid composition at $T_{pb,ice}$ and pure hydrohalite), andthe mixing line "c-NaCl" (between the liquid composition at $T_{pb,hh}$ and pure halite), therefore any pair of $T_{pb,ice}$, $T_{pb,hh}$ or $T_{m,h}$, is sufficient to fix the bulk composition.

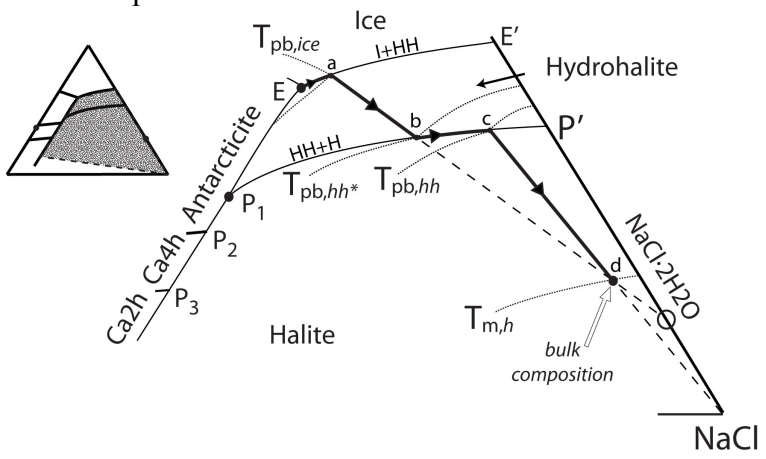

[1]Reprinted from *Geochimica et Cosmochimica Acta*, 75, Steele-MacInnis, M., Bodnar, R.J. & Naden, J., Numerical model to determine the composition of H_2O-NaCl-$CaCl_2$ fluid inclusions based on microthermometric and microanalytical data, 21-40, Copyright (2011), with permission from Elsevier.

2 Volumetrics of CO_2 storage in deep saline formations[2]

Published in Environmental Science & Technology in 2013, with coauthors Ryan Capobianco (Virginia Tech), Robert Dilmore (National Energy Technology Laboratory - NETL), Angela Goodman (NETL), George Guthrie (NETL), J. Donald Rimstidt (Virginia Tech) and Robert J. Bodnar (Virginia Tech).

2.1 Abstract

Concern about the role of greenhouse gases in global climate change has generated interest in sequestering CO_2 from fossil-fuel combustion in deep saline formations. Pore space in these formations is initially filled with brine, and space to accommodate injected CO_2 must be generated by displacing brine, and to a lesser extent by compression of brine and rock. The formation volume required to store a given mass of CO_2 depends on the storage mechanism. We compare the equilibrium volumetric requirements of three end-member processes: CO_2 stored as a supercritical fluid (structural or stratigraphic trapping); CO_2 dissolved in pre-existing brine (solubility trapping); and CO_2 solubility enhanced by dissolution of calcite. For typical storage conditions, storing CO_2 by solubility trapping reduces the volume required to store the same amount of CO_2 by structural or stratigraphic trapping by about 50%. Accessibility of CO_2 to brine determines which storage mechanism (structural/stratigraphic versus solubility) dominates at a given time, which is a critical factor in evaluating CO_2 volumetric requirements and long-term storage security.

2.2 Introduction

Managing climate-altering CO_2 emissions by carbon capture and storage (CCS) presents significant economic, political and technological challenges (Alberts, 2010; IPCC, 2005; Kerr and Kintisch, 2010; Schiermeier, 2006). One option for mitigating CO_2 emissions is to capture and inject CO_2 into confined saline formations. Pore space in deep saline formations is initially filled with brine, and no "free" volume is available to accommodate injected CO_2. Injection of CO_2 must, therefore, be accompanied by increase in formation pressure (Buscheck et al., 2011), compression of fluid and rock, and/or displacement of brine (Buscheck et al., 2011) (Fig. 2.1). Whereas natural subsurface accumulations of CO_2 (e.g., Gilfillan et al., 2008) in environments similar to those proposed for CCS formed slowly and equilibrated with their surroundings over long periods, captured CO_2 will be injected at high volumetric rates over short time spans (tens of years). Numerical modeling has assessed the rate and magnitude of pressure build-up, brine migration and the potential for CO_2 injection-induced seismicity (Cappa and Rutqvist, 2011) associated with rapid injection of large volumes of CO_2 into the subsurface (Zhou and Birkholzer, 2011). Here, we assess equilibrium fluid volume changes in a confined formation after CO_2 injection, based on volumetric properties of the system CO_2-H_2O-NaCl-$CaCO_3$. The results are relevant to estimates of end-point storage capacity and potential long-term security of CO_2 sequestration in saline formations.

Estimates of reservoir CO_2 storage capacity depend on the storage mechanism(s) being considered (IPCC, 2005; Bradshaw et al., 2007). Previous studies estimated CO_2 storage capacity based on structural or stratigraphic trapping of CO_2, without including the effects of CO_2 or calcite dissolution (Goodman et al., 2011; Bradshaw et al., 2007). However, multiple CO_2

trapping mechanisms define the ultimate long-term storage capacity (IPCC, 2005; Bachu and Adams, 2003; Benson and Cole, 2008). Analyses of fluids from natural CO_2 accumulations indicate that, in at least some cases, the total CO_2 capacity is largely determined by solubility trapping (Gilfillan et al., 2009), and thermodynamic modeling has quantified the capacity for CO_2 dissolution into formation waters (Spycher et al., 2003; Spycher and Pruess, 2005). Recent studies have emphasized potential benefits of CO_2 injection protocols designed to promote CO_2-brine dissolution, in order to enhance storage security (Buscheck et al., 2011; Leonenko and Keith, 2010). The effect of CO_2 dissolution and mineral reaction on storage capacity estimates is not yet fully characterized (Bradshaw et al., 2007).

This study compares the sub-surface volume required to store an amount of CO_2 as a supercritical fluid with that required to store the same amount of CO_2 as a dissolved component in brine. We apply thermodynamic modeling of the system CO_2-H_2O-NaCl-$CaCO_3$ to assess the volumetric properties of 1) supercritical CO_2 coexisting with formation brine, 2) CO_2-saturated brine, and 3) CO_2+calcite-saturated brine. Thus, we characterize the volumetric effects of CO_2 dissolution and reaction with calcite, so that these results can be used to refine storage capacity estimates and to design effective protocols to maximize storage capacity and long-term storage security.

2.3 Methods

Various mechanisms are recognized for geological storage of CO_2, including structural or stratigraphic trapping, trapping as a dissolved component in brine, and trapping by reaction with carbonate minerals (IPCC, 2005). Our conceptual model for volumetrics of CO_2 storage in saline formations considers the equilibrium endpoints of these three processes in a stepwise fashion. The total system is represented by an initial mass of CO_2 and a known mass of brine filling the

formation pore space (Fig. 2.1). In the first step, the pore space contains only brine. Supercritical CO_2 is injected into the reservoir and a volume of brine equal to the volume of injected CO_2 is displaced from the reservoir (Fig. 2.1; s_1). In this scenario, we do not consider possible changes in reservoir volume owing to compressibility or deformation. In the second step, CO_2 dissolves into the brine to produce a CO_2-saturated solution (Fig. 2.1; s_2). The volume occupied by the CO_2-saturated solution is less than the volume of the injected CO_2 plus brine at step s_1 because the apparent molar volume of dissolved CO_2 is less than the molar volume of supercritical CO_2 at the storage pressure-temperature (PT) conditions (Gallagher et al., 1993). Thus, fluid volume decreases as the system evolves from s_1 to s_2, enhancing the storage capacity of the reservoir. In step three, some CO_2 and water react with calcite to form Ca^{2+} and HCO_3^-. Because of the fast dissolution rates of carbonate minerals compared to silicates, dissolution of calcite will be the most important mineral reaction initially, but additional mineral solution reactions are expected as the system evolves (Rimstidt, 1997).

Fluid volumetric properties were estimated using published equations of state (EOS) (Duan et al., 2008; Duan et al., 1992; Duan and Sun, 2003; Hu et al., 2007). The density of supercritical CO_2 is represented by a virial-type EOS (Duan et al., 1992). The solubility of CO_2 in water and brine is modeled based on Pitzer's formalism (Pitzer, 1973; Duan and Sun, 2003). The density of the aqueous fluid is calculated from the apparent molar volumes of CO_2 (Duand et al., 2008) and NaCl (Rogers and Pitzer, 1982) and the molar volume of H_2O (Hu et al., 2007). The CO_2 solubility model (Duan and Sun, 2003) has been tested by modeling CO_2 storage in natural brines, and yielded good results (Dilmore et al., 2008). To compare the volume required to store CO_2 as a supercritical fluid (structural or stratigraphic trapping) with the volume required to store the same amount of CO_2 as a dissolved component in brine (solubility trapping), we

selected initial amounts of brine and CO_2 such that all injected CO_2 could be dissolved to produce CO_2-saturated brine. Next, we added increments of calcite and as much additional CO_2 as can be dissolved by reaction with calcite. This approach allows comparison of volumetric changes for three trapping processes – s_1 in which all CO_2 is stored as a supercritical fluid, s_2 in which all CO_2 is stored as a dissolved component in brine, and s_3 in which additional CO_2 is dissolved via the calcite dissolution reaction. All calculations assume constant pressure, although in real-world scenarios, pressure and fluid volume will both increase somewhat upon injection.

Based on various economic and geological constraints, the storage horizon in saline formations will likely be between 1.0-4.5 km depth, with temperature of 50-140 °C, and pressure before injection of 10-75 MPa (IPCC, 2005; Nordbotten et al., 2005; Benson and Cole, 2008). The minimum pressure represents hydrostatic pressure, and the maximum pressure represents 0.6 × lithostatic pressure at the depth of interest. At pressure above this value, vertically oriented hydrofractures may develop (Hubert and Willis, 1957; Bredehoeft et al., 1976). This PT range is highlighted in grey on the PT plots displaying the results. Previous studies considered the feasibility of injecting large volumes of CO_2 into deep saline formations (Ghaderi et al., 2009; Ehlig-Economides and Economides, 2010; Zhou and Birkholzer. 2011), including various economic and engineering constraints not considered here. Briefly, these studies suggest that pressure build-up during injection may be a limiting factor in determining storage capacity of a formation, but that both passive (diffuse leakage) and active (brine extraction) methods can attenuate pressure and allow large-scale injection to proceed (Zhou and Birkholzer, 2011).

In the following sections, volumetric changes accompanying s_1) CO_2 injection (physical trapping), s_2) dissolution in brine, and s_3) reaction with calcite are described at discrete times following injection. The motivation for presenting results at discrete stages is to differentiate the

volumetric contributions of each mechanism. We emphasize that during and after injection, several trapping mechanisms will likely contribute to the overall storage capacity simultaneously (IPCC, 2005). However, as a first approximation it is reasonable to separate the various processes based on the different time scales at which each is dominant. Field and laboratory experiments and numerical simulations have semi-quantitatively constrained the times required for CO_2 dissolution and mineral reactions in saline aquifers. Although time estimates show wide variability (owing mainly to differences in local reservoir conditions and hydrology), a compilation of those results (IPCC, 2005) suggests overall agreement that physical trapping dominates in the first years to decades while dissolution of CO_2 and calcite becomes significant over decades to centuries. Other mineral reactions contribute centuries to millennia *after* injection (Fig. 1)(IPCC, 2005).

Immediately following CO_2 injection, the system consists of brine and supercritical CO_2, and the system volume equals the initial volume of brine plus the volume of injected supercritical CO_2 (Fig. 2.1, s_1). The increase in fluid volume when CO_2 is injected into an H_2O- or H_2O-NaCl-filled formation is

$$\%\ \text{volume increase} = \frac{\overline{V}_{CO_2} m_{CO_2}}{\overline{V}_{H_2O-NaCl}\left(m_{NaCl} + \frac{1000\ {}^{g}\!/_{kg}}{M_{H_2O}}\right)} \times 100\ \% \qquad (2.1)$$

where $\overline{V}_{CO_2}$ and $\overline{V}_{H_2O-NaCl}$ are the molar volumes of the CO_2 phase and aqueous phase, respectively (cm^3/mol), m_{CO_2} and m_{NaCl} are the CO_2 solubility and brine salinity, respectively (mol/kg H_2O), and M_{H_2O} is the molar mass of H_2O (g/mol). Equation (2.1) is based on constant mass of H_2O in the system during and after CO_2 injection, representing the pre-existing brine in

the pore volume, and the total fluid volume implicitly includes any brine displaced or extracted during injection. Thus, equation (2.1) (and the subsequent equations) computes volumes in units of *cm^3 per kg H_2O*. Whereas the total amount (number of moles) of fluid in the system is not constant (it increases, as CO_2 is injected), the total mass of H_2O in the system is constant. Therefore, volume changes per kg H_2O represent changes in total fluid volume.

The injected CO_2 phase and aqueous brine are not in chemical equilibrium. Over time CO_2 dissolves into the aqueous phase. The volume change as the system evolves from CO_2-free brine to CO_2-saturated brine is

$$\%\ \text{volume increase} = \frac{\left(\frac{\overline{V}_{H_2O-NaCl-CO_2}}{X_{H_2O} M_{H_2O}} \times 1000\ {}^{g}\!/_{kg}\right)}{\overline{V}_{H_2O-NaCl}\left(m_{NaCl} + \frac{1000\ {}^{g}\!/_{kg}}{M_{H_2O}}\right)} \times 100\ \% \qquad (2.2)$$

where $\overline{V}_{H_2O-NaCl-CO_2}$ is the molar volume of the CO_2-saturated aqueous phase (cm^3/mol) and X_{H_2O} is the mole fraction of H_2O in the aqueous phase.

Reaction with calcite allows dissolution of additional CO_2, according to the reaction

$$CO_2(v) + H_2O(l) + CaCO_3(cal) = Ca^{2+} + 2HCO_3^-(aq) \qquad (2.3)$$

The equilibrium constant for equation (2.3) was calculated based on the Henry's Law constant for CO_2 dissolution, the calcite solubility product, and the first and second H_2CO_3*(aq)* dissociation constants. The solubility of calcite (and resulting enhanced CO_2 solubility) was calculated by extrapolating the temperature functions for the relevant equilibrium constants

(Plummer and Busenberg, 1982) over the PT range of the model. The volume change of the aqueous phase resulting from calcite dissolution is estimated by approximating the volume occupied by dissolved Ca^{2+} and HCO_3^- ions based on the apparent molar volume of dissolved $CaCl_2$ (Oakes et al., 1995). The volume change is expressed as

$$\% \text{ volume change} = \frac{S_{\text{cal}} V_{\text{Ca(HCO}_3)_2(aq)}}{V_{\text{CO}_2\text{-saturated solution}} + S_{\text{cal}} V_{\text{Ca(HCO}_3)_2(aq)}} \times 100\ \% \tag{2.4}$$

where $V_{\text{Ca(HCO}_3)_2(aq)}$ is the apparent molar volume of dissolved calcium and bicarbonate ions and S_{cal} is the solubility of calcite (mol/kg H_2O).

Our model considers the system H_2O-NaCl-CO_2-$CaCO_3$, whereas natural saline brines contain other salts, and injected CO_2 may contain other gaseous species. Lack of experimental data over the complete PT range of interest limits our ability to quantitatively model these effects. However, we expect that overall trends in solubility and volumetric properties are reasonably approximated by the H_2O-NaCl-CO_2-$CaCO_3$ system. For example, CO_2 solubility experiments in natural connate brines from the Oriskany formation (eastern USA) showed good agreement with the CO_2 solubility model used here (Duan and Sun, 2003; Dilmore et al., 2008).

2.4 Results and discussion

At PT conditions of CO_2 storage in saline formations, CO_2 density ranges from about 0.4 to 0.8 g/cm^3 (Fig. 2.2). At the same conditions, the solubility of CO_2 in H_2O ranges from about 2 to 3.4 mol% (Fig. 2.3a & b), and CO_2 solubility in 15 wt% NaCl brine (throughout this section, the term "brine" refers to an aqueous fluid of 15 wt% NaCl) ranges from about 1.1 to 1.8 mol% (Fig.

2.3c & d) (Takenouchi and Kennedy, 1964; Duan and Sun, 2003; Spycher et al., 2003; Spycher and Pruess, 2005).

When an amount of CO_2 equal to the amount required to saturate the aqueous phase (i.e., the amount of CO_2 that could be stored as a dissolved component in the brine) is injected, its volume is between 75-140 cm^3 per kg water, or 50-70 cm^3 per kg brine. During injection, the total fluid volume (*before* dissolution) increases by approximately 7.3 to 10 percent for pure H_2O (Fig. 2.4a & b), or by about 3.9 to 5.4 percent for brine (Fig. 2.4c & d). The larger volume increase for H_2O compared to brine reflects higher solubility of CO_2 in pure H_2O compared to brine at the same PT conditions (requiring injection of a greater amount of CO_2 to saturate pure H_2O, Fig. 2.3).

The maximum amount of CO_2 that can be dissolved in brine is limited by the CO_2 solubility at the formation PT conditions (Fig. 2.3). The apparent volume of dissolved CO_2 at saturation is between 40-80 cm^3 per kg water, or 25-55 cm^3 per kg brine. Therefore, the volume occupied by the CO_2-saturated aqueous phase is greater than the brine (H_2O) volume before injection (Fig. 2.1). Within the PT range considered here, the volume increases by about 3.5 to 8 percent if the pore fluid is pure H_2O (Fig. 2.5a), and by about 2.2 to 4 percent if the pore fluid is brine (Fig. 2.5b).

Owing to the low solubility of calcite, dissolution of calcite increases the volume of the aqueous phase by only 0.01-0.04 percent (Fig. 2.6). Thus, the contribution of calcite dissolution to the net volume change is insignificant compared to the contributions of supercritical CO_2 or dissolved CO_2.

The volume changes described above (Figs. 2.4-2.6) are compared to the initial fluid volume before CO_2 injection (Fig. 2.1). We also compared volume change as the CO_2 phase (s_1;

Fig 2.1) dissolves into the brine (s_2; Fig. 2.1). As shown by the reduced area of the displaced brine box between s_1 and s_2 (Fig. 2.1), dissolution of CO_2 into brine reduces the net fluid volume (compared to the sum of the volumes of brine and CO_2 immediately following injection). Throughout most of the PT region of CO_2 storage, the apparent volume of dissolved CO_2 is about half of the volume of the same mass of supercritical CO_2. Therefore, the volume decrease from s_1 to s_2 is between 45 and 65 percent, independent of whether the pore fluid is H_2O or brine (Fig. 2.7c & d). In other words, although the volume required to store injected CO_2 is greater than the initial brine volume regardless of whether CO_2 is dissolved or is present as a separate supercritical fluid, solubility trapping requires only 50% of the volume required for structural or stratigraphic trapping of the same amount of CO_2.

Previous studies have emphasized that dissolution of CO_2 increases the density of the brine, making CO_2-saturated brine negatively buoyant compared to CO_2-free brine (Lu et al., 2009). Thus, CO_2-saturated brine will sink in the reservoir (Lu et al., 2009), enhancing storage security. Based on volumetric modeling, we show that this mechanism has the additional advantage of enhancing storage capacity (Fig. 2.7). The rate of CO_2 dissolution depends on the contact area between the CO_2 and brine phases, and how quickly aqueous CO_2 diffuses into the brine. Unassisted, the contribution of solubility trapping becomes significant only after centuries (Fig. 2.1). Some studies have suggested reservoir engineering approaches to accelerate the dissolution of CO_2 into brine, with the aim of enhancing storage security (Leonenko and Keith, 2010; Buscheck et al., 2011). Our results suggest such procedures will also enhance storage capacity.

As a simple example, consider a target formation at a depth of 2 km, with an injection interval of 50 m. If 28 million tonnes of CO_2 were injected over 30 years, based on simplifying

assumptions for formation properties, injection rate and fluid characteristics, then the maximum estimated plume radius is 7.4 km (Nordbotten et al., 2005). A reasonable estimate of microscopic brine displacement efficiency (the proportion of brine that is swept out of the CO_2 plume during injection) for a clastic reservoir is ~50% (Goodman et al., 2011). Therefore, about 50% of the brine initially present in the pore volume within the plume remains available to dissolve CO_2. The residual brine volume accessible for CO_2 dissolution within the plume is 4×10^7 m^3. The volume of brine outside the plume but within the cylindrical volume of the maximum plume radius is 8×10^8 m^3. The proportion of brine outside the plume that is accessible for CO_2 dissolution is unconstrained, although we can reasonably expect that this proportion will increase with time (as CO_2 diffuses outward from the plume). We consider two endmember scenarios, assuming either 10% or 100% of available brine outside the plume is accessible for CO_2 dissolution.

If CO_2 is injected to a maximum pressure of 90% of the fracture pressure (~54% of lithostatic pressure) and after injection the pressure is allowed to relax back to hydrostatic (~20 MPa in this example), and 10% of the brine outside the plume is accessible for CO_2 dissolution, then about 10% of the injected CO_2 can be dissolved in the available brine (~3% dissolved in residually trapped brine, and ~7% dissolved in brine outside the plume). This reduces the total CO_2 volume by ~5%. If 100% of the brine outside of the plume (but within the plume maximum radial extent) were available for CO_2 dissolution, then the proportion of CO_2 that can dissolve increases to about 70%. This results in a reduction in the apparent volume of CO_2 of ~45%. Thus, the accessibility of brine for CO_2 dissolution is a critical parameter in reducing volumetric requirements associated with solubility trapping. Ultimately, reservoir simulations incorporating

lithological and hydrological parameters are required to predict the capacity of solubility trapping in saline formations (Bradshaw et al., 2007).

Our results indicate that the CO_2 storage capacity of a formation is influenced by the volumetric changes associated with CO_2 dissolution into brine. We have not attempted comparisons with previous storage capacity estimates from literature because previous comparisons have shown large variations and sometimes contradictory results, making such comparisons uninformative (Bradshaw et al., 2007).

The present study considers final equilibrium states and does not consider effects of fluid flow, pressure gradients, or other factors associated with injection. Figure 2.1 shows the approximate time intervals over which various trapping mechanisms are expected to become significant, based on reservoir studies and simulations (IPCC, 2005), but the actual time scales depend on the formation geometry and rock properties (Bradshaw et al., 2007). For example, dissolution of CO_2 into brine in a low permeability unit will take significantly longer compared to a high permeability unit (Bradshaw et al., 2007). Elucidating the time scales of CO_2-brine-mineral interactions during and after injection requires site-specific reservoir simulations on a case-by-case basis (Bradshaw et al., 2007). Regardless of the time needed to reach equilibrium, these results document that storing CO_2 as a dissolved component in brine reduces the volume required to store a given amount of CO_2.

2.5 Implications

There appear to be significant advantages to solubility trapping for CO_2 storage in brine-filled formations. Our results document that storage volume requirements are reduced by about 50% if CO_2 is dissolved in the brine (solubility trapping), rather than a separate supercritical fluid (structural or stratigraphic trapping). In addition, CO_2-bearing brine is denser than CO_2-free

brine, so that CO_2 -saturated brine will migrate downwards within the formation, thus enhancing long-term storage security. Although the present study does not permit rigorous evaluation of the timescales required to achieve these advantages, the results suggest that storage volume requirements may be reduced by sequestration protocols involving extraction of brine, dissolution of CO_2 into the extracted brine at the surface, followed by reinjection of the CO_2-saturated brine into the formation (Leonenko and Keith, 2010; Buscheck et al., 2011) To fully evaluate this alternative operational paradigm for geologic CO_2 storage requires comprehensive reservoir simulations that consider pressure evolution, fluid flow and temporal changes in CO_2 trapping mechanisms. In addition, associated process requirements including characterization of life cycle energy, emissions and economic implications must be considered.

2.6 References

Alberts, B., 2010. Policy-Making Needs Science. *Science* **330**, 1287-1287.

Bachu, S., Adams, J. J., 2003. Sequestration of CO_2 in geological media in response to climate change: capacity of deep saline formations to sequester CO_2 in solution. *Energy Conversion and Management* **44**, 3151–3175.

Benson, S. M., Cole, D. R., 2008. CO_2 Sequestration in Deep Sedimentary Formations. *Elements* **4**, 325-331.

Bradshaw, J., Bachu, S., Bonijoly, D., Burruss, R., Holloway, S., Christensen, N. P., Mathiassen, O. M., 2007. CO_2 storage capacity estimation: Issues and development of standards. *International Journal of Greenhouse Gas Control* **1**, 62-68.

Bredehoeft, J. D., Wolff, R. G., Keys, W. S., Shuter, E., 1976. Hydraulic fracturing to determine the regional in situ stress field, Piceance Basin, Colorado. *Geological Society of America Bulletin* **87***,* 250-258.

Buscheck, T. A., Sun, Y., Hao, Y., Wolery, T., Bourcier, W., Thompson, A. F. B., Jones, E. D., Friedmann, S. J., Aines, R. D., 2011. Combining brine extraction, desalination, and residual-brine reinjection with CO_2 storage in saline formations: Implications for pressure management, capacity, and risk mitigation. *Energy Procedia* **4**, 4283-4290.

Cappa, F., Rutqvist, J., 2011. Impact of CO_2 geological sequestration on the nucleation of earthquakes. *Geophysical Research Letters* **38**, L17313.

Dilmore, R. M., Allen, D. E., McCarthy Jones, J. R., Hedges, S. W., Soong, Y., 2008. Sequestration of dissolved CO_2 in the Oriskany formation. *Environmental Science and Technology* **42**, 2760-2766.

Duan, Z. H., Hu, J. W., Li, D. D., Mao, S. D., 2008. Densities of the CO_2-H_2O and CO_2-H_2O-NaCl systems up to 647 K and 100 MPa. *Energy and Fuels* **22**, 1666-1674.

Duan, Z. H., Moller, N., Weare, J. H., 1992. An Equation of State for the CH_4-CO_2-H_2O System: I. Pure Systems from 0 to 1000°C and 0 to 8000 Bar. *Geochimica et Cosmochimica Acta* **56**, 2605-2617.

Duan, Z. H., Sun, R., 2003. An improved model calculating CO_2 solubility in pure water and aqueous NaCl solutions from 273 to 533 K and from 0 to 2000 bar. *Chemical Geology* **193**, 257-271.

Ehlig-Economides, C., Economides, M. J., 2010. Sequestering carbon dioxide in a closed underground volume. *Journal of Petroleum Science and Engineering* **70**, 123-130.

Gallagher, J. S., Crovetto, R., Levelt Sengers, J. M. H., 1993. The thermodynamic behavior of the CO_2-H_2O system from 400 to 1000 K, up to 100 MPa and 30% mole fraction of CO_2. *Journal of Physical Chemistry Reference Data* **22**, 431-513.

Ghaderi, S. M., Keith, D. W., Leonenko, Y., 2009. Feasibility of injecting large volumes of CO_2 into aquifers. *Energy Procedia* **1**, 3113-3120.

Gilfillan, S. M., Ballentine, C. J., Holland, G., Blagburn, D., Sherwood Lollar, B., Stevens, S., Schoell, M., Cassidy, M., 2008. The noble gas geochemistry of natural CO_2 gas reservoirs from the Colorado Plateau and Rocky Mountain provinces, USA. *Geochimica et Cosmochimica Acta* **72**, 1174-1198.

Gilfillan, S. M. V., Sherwood Lollar, B., Holland, G., Blagburn, D., Stevens, S., Schoell, M. Cassidy, M., Ding, Z., Zhou, Z., Lacrampe-Couloume, G., Ballentine, C. J., 2009. Solubility trapping in formation water as dominant CO_2 sink in natural gas fields. *Nature* **458**, 614-618.

Goodman, A., Hakala, A., Bromhal, G., Deel, D., Rodosta, T., Frailey, S., Small, M., Allen, D., Romanov, V., Fazio, J., Huerta, N., McIntyre, D., Kutchko, B., Guthrie, G., 2011. U.S. DOE methodology for the development of geologic storage potential for carbon dioxide at the national and regional scale. *International Journal of Greenhouse Gas Control* **5**, 952-965.

Hu, J. W., Duan, Z. H., Zhu, C., Chou, I. M., 2007. PVTx properties of the CO_2-H_2O and CO_2-H_2O-NaCl systems below 647 K: Assessment of experimental data and thermodynamic models. *Chemical Geology* **238**, 249-267.

Hubbert, M. K., Willis, D. G., 1957. Mechanics of hydraulic fracturing. *Transactions of A. I. M. E.* **210**, 153-166.

Intergovernmental Panel on Climate Change, 2005. Underground geological storage. In Metz, B., Davidson, O., de Coninck, H. C., Loos, M., Meyer, L. A., (Eds.): *IPCC Special Report on Carbon Dioxide Capture and Storage*. Cambridge University Press: New York. pp 195-276.

Kerr, R. A., Kintisch, E., 2010. Climatologists feel the heat as science meets politics. *Science* **330**, 1623.

Leonenko, Y., Keith, D. W., 2010. Reservoir engineering to accelerate the dissolution of CO_2 stored in formations. *Environmental Science and Technology* **42***,* 2742-2747.

Lu, C., Han, W. S., Lee, S. Y., McPherson, B. J., Lichtner, P. C., 2009. Effects of density and mutual solubility of a CO_2-brine system on CO_2 storage in geological formations: "Warm" vs. "cold" formations. *Advances in Water Resources* **32**, 1685-1702.

Nordbotten, J. M., Celia, M. A., Bachu, S., 2005. Injection and storage of CO_2 in deep saline aquifers: Analytical solution for CO_2 plume evolution during injection. *Transport in Porous Media* **58***,* 339-360.

Oakes, C. S., Simonson, J. M., Bodnar, R. J., 1995. Apparent molar volumes of aqueous calcium chloride to 250°C, 400 bars, and from molalities of 0.242 to 6.150. *Journal of Solution Chemistry* **24**, 897-916.

Pitzer, K. S., 1973. Thermodynamics of electrolytes: I. Theoretical basis and general equations. *Journal of Physical Chemistry* **77**, 268–277.

Plummer, L. N., Busenberg, E., 1982. The solubilities of calcite, aragonite and vaterite in CO_2-H_2O solutions between 0 °C and 90 °C, and an evaluation of the aqueous model for the system $CaCO_3$-CO_2-H_2O. *Geochimica et Cosmochimica Acta* **46***,* 1011-1040.

Rimstidt, J. D., 1997. Gangue mineral transport and deposition. In Barnes, H. L. (Ed.) *Geochemistry of Hydrothermal Ore Deposits*. John Wiley & Sons: New York, pp 487-515.

Rogers, P. S. Z., Pitzer, K. S., 1982. Volumetric properties of aqueous sodium chloride solutions. *Journal of Physical Chemistry Reference Data* **11**, 15-81.

Schiermeier, Q., 2006. Putting the carbon back: The hundred billion tonne challenge. *Nature* **442**, 620-623.

Spycher, N., Pruess, K., 2005. CO_2-H_2O mixtures in the geological sequestration of CO_2. II. Partitioning in chloride brines at 12-100°C and up to 600 bar. *Geochimica et Cosmochimica Acta* **69**, 3309-3320.

Spycher, N., Pruess, K., Ennis-King, J., 2003. CO_2-H_2O mixtures in the geological sequestration of CO_2. I. Assessment and calculation of the mutual solubilities from 12 to 100°C and up to 600 bar. *Geochimica et Cosmochimica Acta* **67**, 3015-3031.

Takenouchi, S., Kennedy, G. C., 1964. The binary system H_2O-CO_2 at high temperatures and pressures. *American Journal of Science* **262**, 1055-1074.

Zhou, Q., Birkholzer, J. T., 2011. On the scale and magnitude of pressure build-up induced by the large-scale storage of CO_2. *Greenhouse Gases in Science and Technology* **1**, 11-20.

2.7 Figures

Figure 2.1. Conceptual model of volume changes associated with various CO_2 storage mechanisms following injection of CO_2 into a saline formation.
At s_0 the system is represented by a volume of CO_2 captured from flue gases (yellow box) and a subsurface saline formation in which all of the pore volume is filled with brine (blue box). As a result of injection of supercritical CO_2 into the formation (s_1), an equal volume of brine is displaced from the formation. Some of the CO_2 dissolves into the brine. The volume of the CO_2-saturated brine (green box at s_2) is less than that of the supercritical CO_2 plus brine (s_1), but greater than the original brine volume before CO_2 injection (s_0). Bottom: Approximate time scales over which various trapping mechanisms become significant (modified from the IPCC 2005 report).

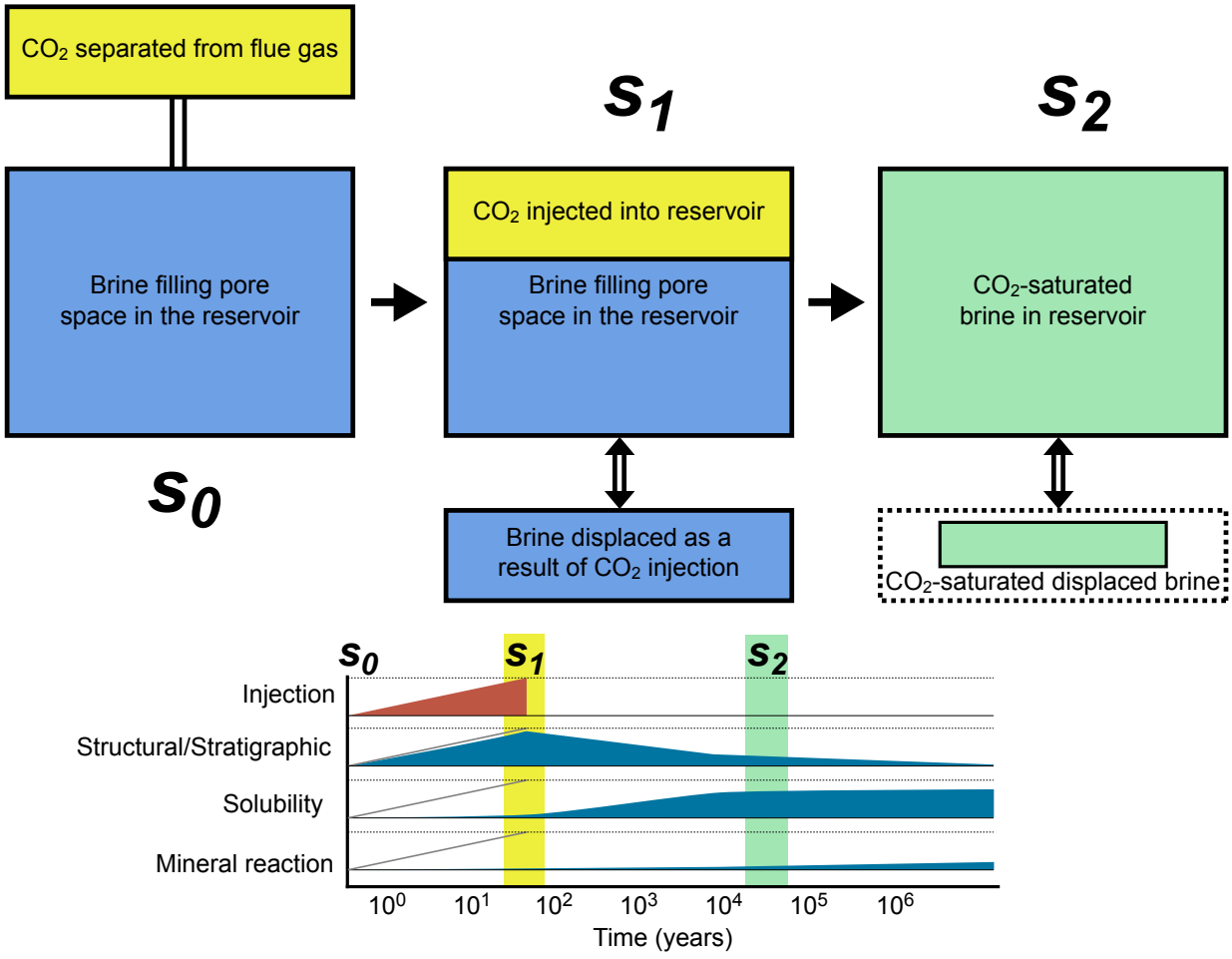

Figure 2.2. Density of CO_2 (in g/cm^3) as a function of pressure and temperature. Shown in pressure-temperature space (a) and in depth-fraction of lithostatic pressure space (b). Hydrostatic and lithostatic pressure gradients shown in (a) assume a geothermal gradient of 25 °C/km. The shaded area represents the PT conditions technologically and economically accessible for CO_2 storage in saline formations. Notice that A and B contain the same data presented on different axes.

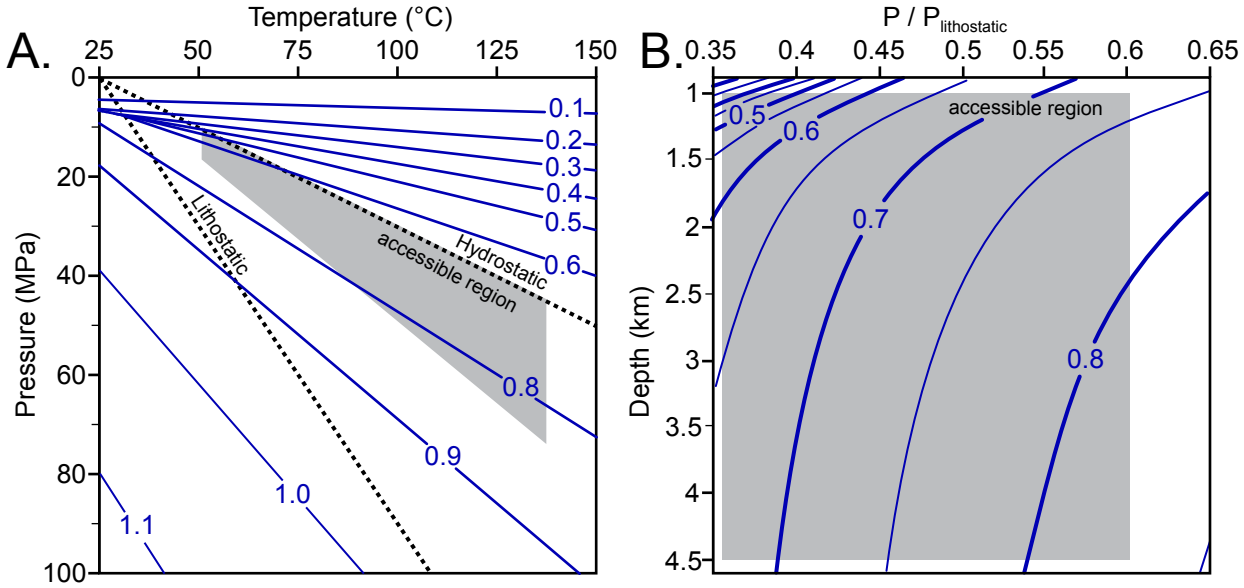

Figure 2.3. Solubility of CO_2 (mol%) as a function of pressure and temperature. Solubility of CO_2 in H_2O (a & b) and in 15 wt% NaCl brine (c & d). The data are plotted in pressure-temperature space (a & c) and in depth-fraction of lithostatic pressure space (b & d). The shaded area represents the PT conditions accessible for CO_2 storage in saline formations.

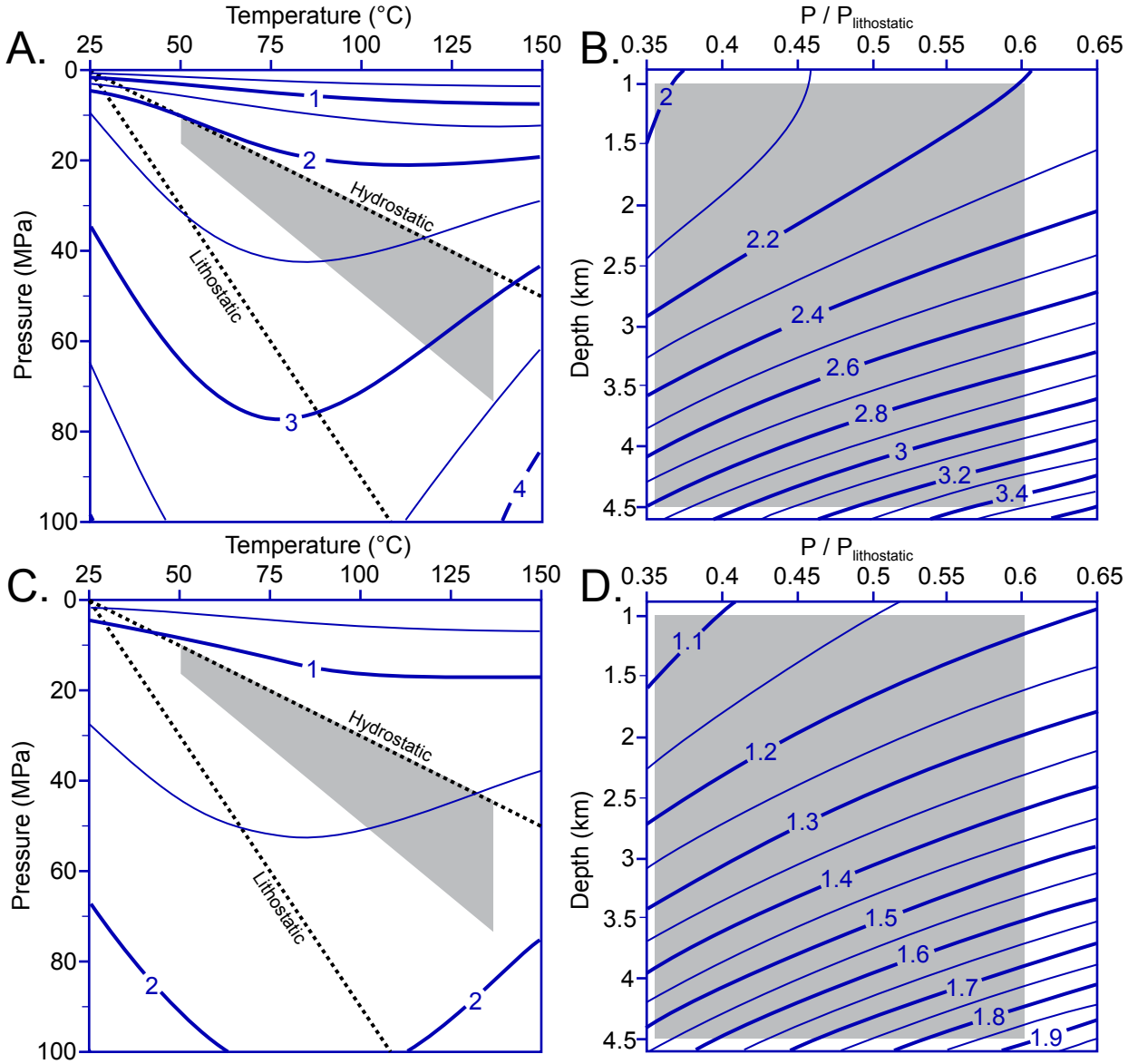

Figure 2.4. Percent increase in fluid volume when CO_2 is stored in a subsurface reservoir as a separate supercritical fluid.
The volume increase represents the percent difference between the volume of the brine *plus* the volume supercritical CO_2 injected (Fig. 2.1, s_1), compared to the volume of brine before injection (Fig. 2.1, s_0). The data are plotted in pressure-temperature space (a & c) and depth-fraction of lithostatic pressure space (b & d). The shaded area represents the PT conditions accessible for CO_2 storage in saline formations. Figures a & b are for H_2O and c & d are for 15 wt% NaCl brine.

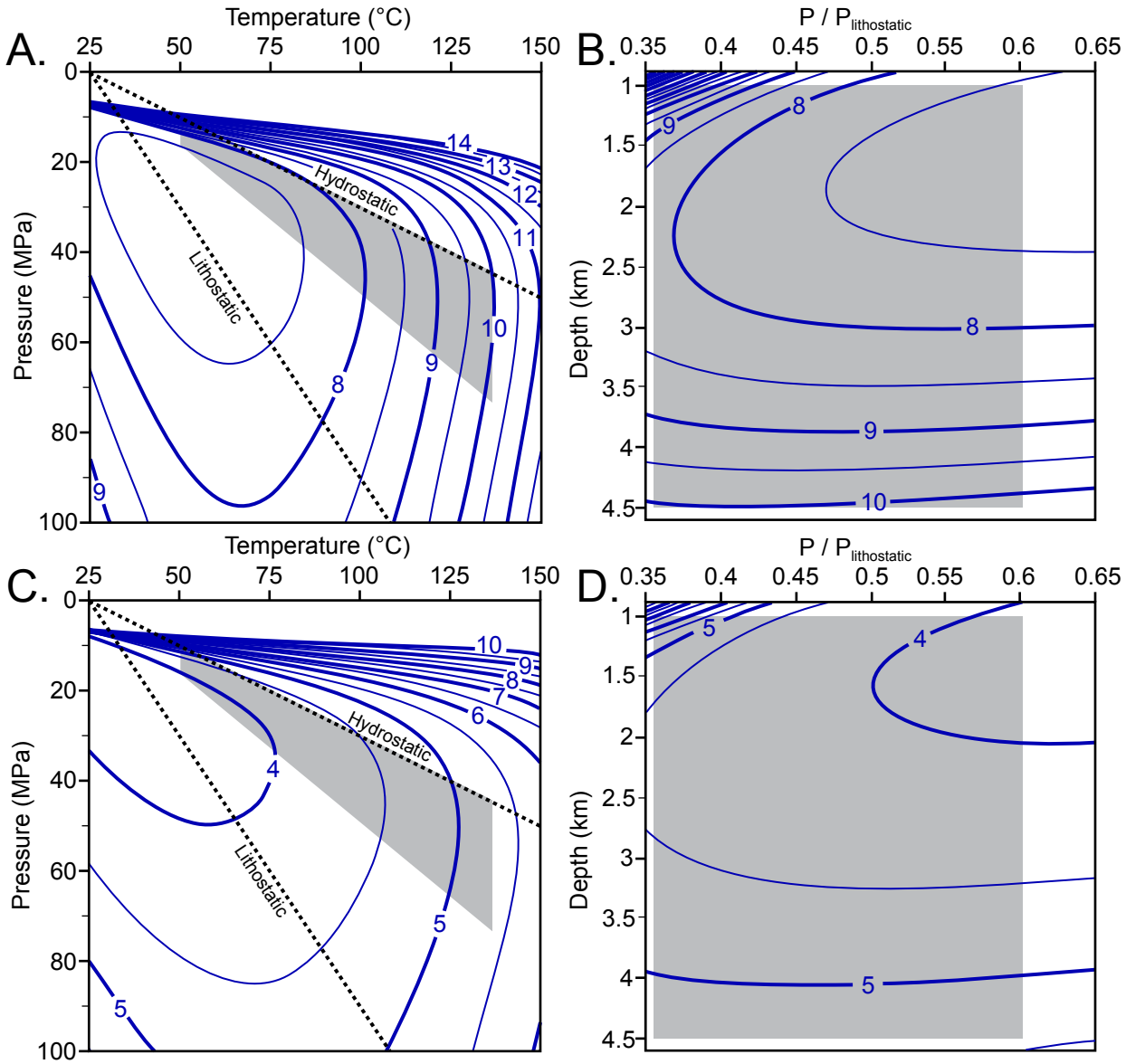

Figure 2.5. Percent increase in fluid volume after injected CO_2 has dissolved to produce a single-phase, CO_2-saturated brine.
Shown as percent difference between the volume of CO_2-bearing brine at s_2 compared to the volume of brine before injection (Fig. 2.1, s_0). The data are plotted in pressure-temperature space (a & c) and depth-fraction of lithostatic pressure space (b & d). The shaded area represents the PT conditions accessible for CO_2 storage in saline formations. Figures a & b are for H_2O and c & d are for a 15 wt% NaCl brine.

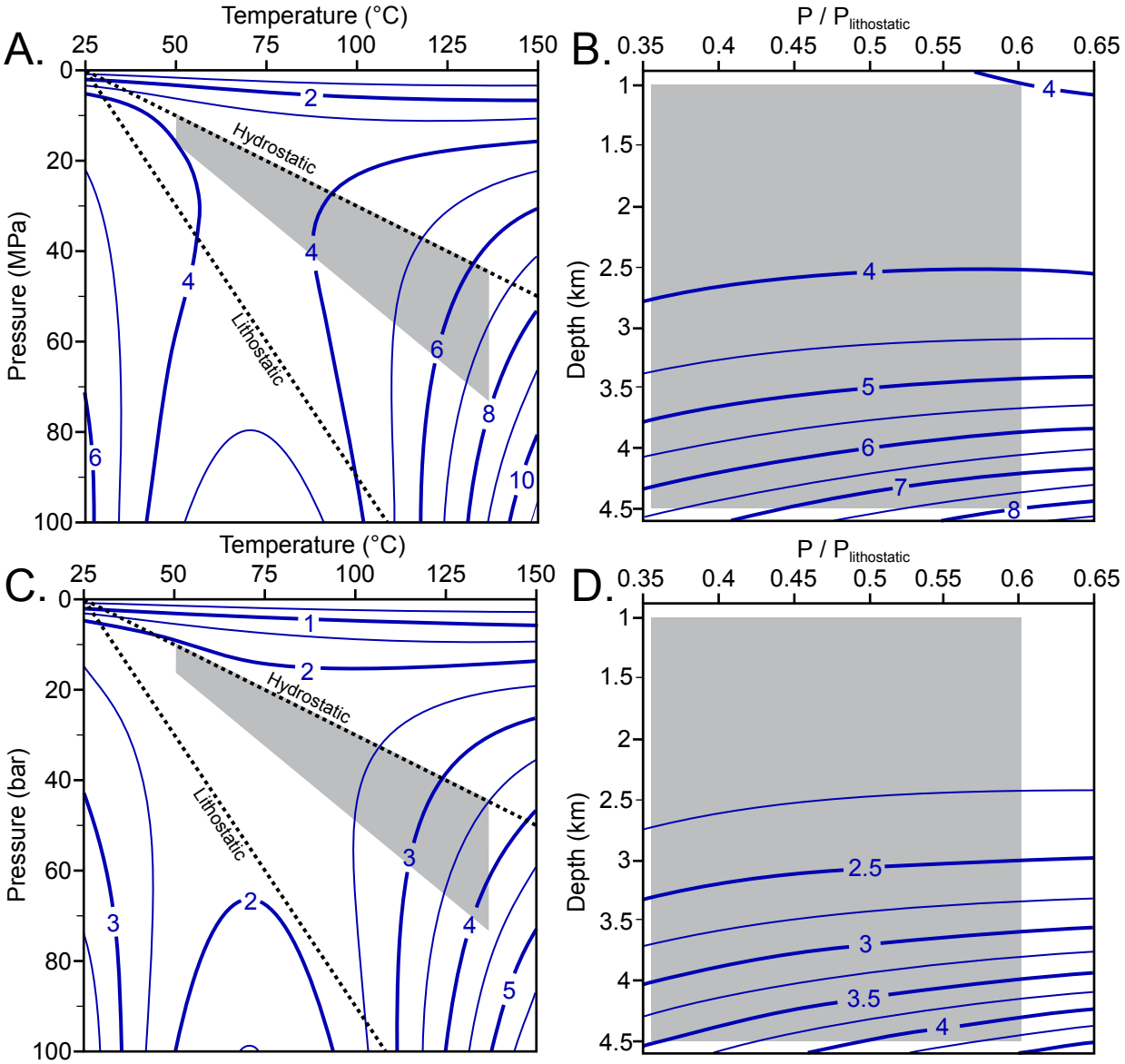

Figure 2.6. Percent fluid volume change as a result of CO_2-promoted calcite dissolution, relative to the initial volume of pore water.
The data are plotted in pressure-temperature space (a) and depth-fraction of lithostatic pressure space (b). The shaded area represents the PT conditions accessible for CO_2 storage in saline formations.

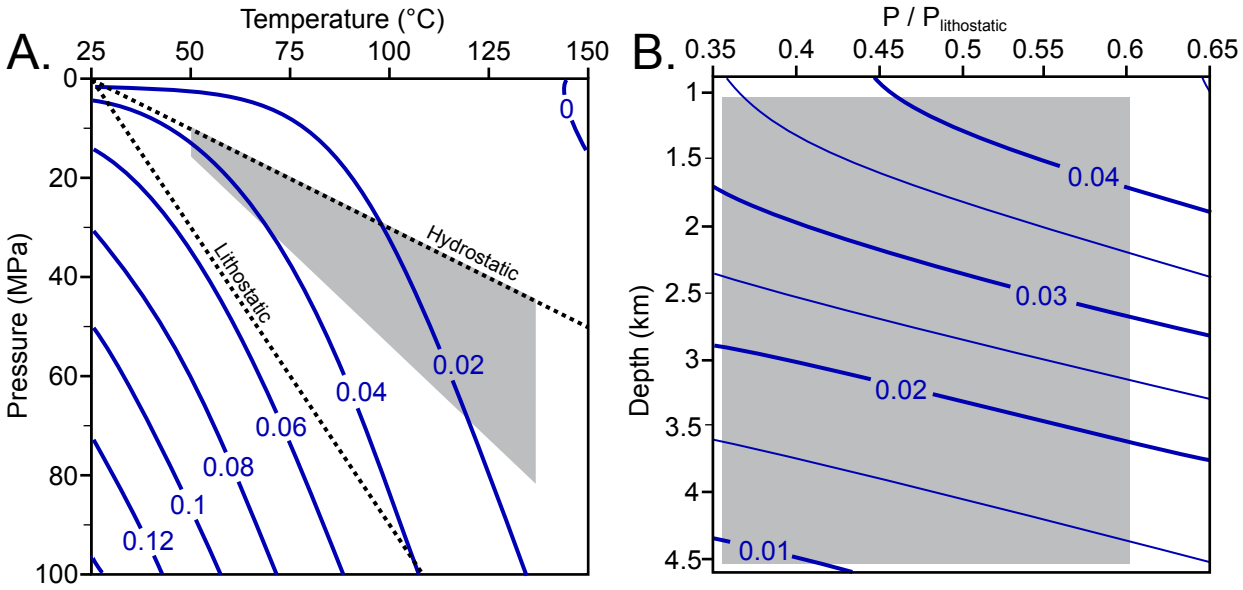

Figure 2.7. Percent difference in CO_2 apparent volume for CO_2 storage as a supercritical fluid, compared to storage as a dissolved component in brine.
The values represent the difference in volume increase between s_2 (Fig. 2.5) and s_1 (Fig. 2.4). The data are plotted in pressure-temperature space (a & c) and depth-fraction of lithostatic pressure space (b & d). The shaded area represents the PT conditions accessible for CO_2 storage in saline formations. Figures a & b are for H_2O and represent the percent difference between values shown in Figures 2.5a & b for CO_2 storage as a supercritical fluid, compared to volume required for CO_2 storage as a dissolved component in the brine shown in Figures 2.4a & b). Figures c & d show the same comparison for 15 wt% NaCl brine (Figures 2.5c & d compared to 2.4c & d).

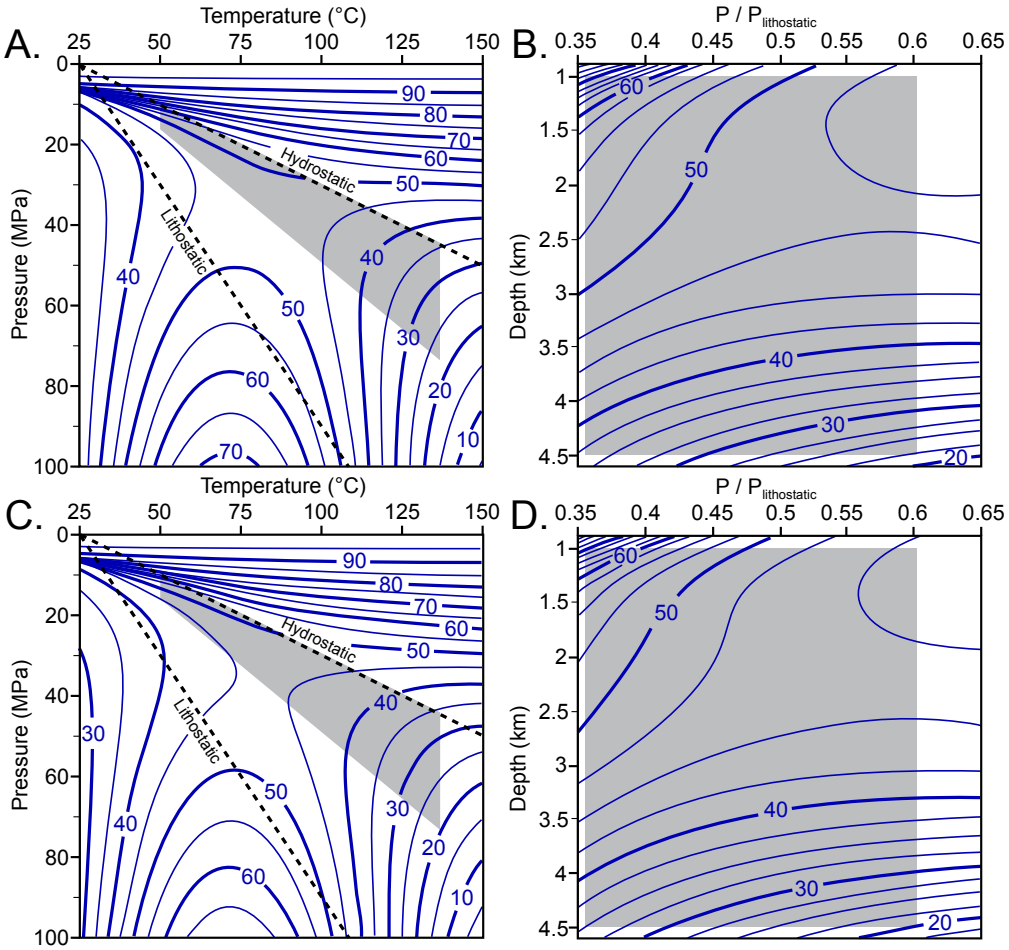

[2]Reprinted with permission from *Environmental Science & Technology*, 47, Steele-MacInnis, M., Capobianco, R.M., Dilmore, R., Goodman, A., Guthrie, G., Rimstidt, J.D. & Bodnar, R.J., Volumetrics of CO2 storage in Deep Saline Formations, 79-86. Copyright (2013), American Chemical Society.

3 The role of fluid phase immiscibility in quartz dissolution and precipitation in sub-seafloor hydrothermal systems[3]

Published in Earth and Planetary Science Letters in 2012, with coauthors Liang Han (Virginia Tech), Robert P. Lowell (Virginia Tech), J. Donald Rimstidt (Virginia Tech) and Robert J. Bodnar (Virginia Tech).

3.1 Abstract

A numerical model describing quartz dissolution and precipitation in sub-seafloor hydrothermal systems has been developed that documents the effects of retrograde quartz solubility and fluid phase immiscibility on the transport and deposition of silica in this environment. Rates of dissolution and precipitation increase with increasing permeability and with increasing maximum temperature at the base of the system. At the most optimal conditions considered in this study (425°C, permeability of 10^{-13} m^2), quartz is precipitated at rates up to 10^{-6} $mol/m^3 \cdot s$ (equivalent to 700 cubic centimeters of quartz per cubic meter of rock per year). Immiscibility at the base of the system creates a zone in which large amounts of quartz precipitate as a result of phase separation. The high rate of quartz precipitation at the one-fluid-phase/two-fluid phase boundary is consistent with the location of highly silicified zones found beneath volcanogenic massive sulfide deposits. Rapid quartz deposition at this boundary may affect the heat transfer efficiency at the base of the upflow zone and may contribute to immobilizing the brine layer so that it does not rise towards the surface. The process of rapid quartz precipitation at the base of the upflow zone, and its effects on the dynamics of these systems, is only observed under conditions of liquid-vapor immiscibility.

3.2 Introduction

3.2.1 Sub-seafloor processes in submarine hydrothermal systems

A major goal in the study of submarine hydrothermal systems, including their seafloor manifestations, (*e.g.*, "black smokers") is to understand the physical and chemical processes occurring beneath the seafloor at mid-ocean ridges (Alt, 1995). In the late 1970s Welhan and Craig (1979) suggested that liquid-vapor phase separation likely occurred in the sub-seafloor at 21°N on the East Pacific Rise (EPR), before the fluids vented onto the seafloor at about 2,600 m below the ocean surface. While this hypothesis was questioned by many workers, subsequent analytical and experimental studies supported the hypothesis that hydrothermal fluids in the sub-seafloor experienced immiscibility or phase separation (often referred to as "boiling" in the literature) (Bischoff and Pitzer, 1985; Delaney et al., 1987; Kelley et al., 1992; Vanko, 1988; Vanko et al., 2004). In particular, fluid inclusion studies of seafloor samples provided compelling evidence of the occurrence of phase separation in these environments (Delaney et al., 1987; Kelley et al., 1992; Stakes and Vanko, 1986; Vanko, 1988; Vanko et al., 2004; Vanko et al., 1992). Today it is generally accepted that sub-seafloor phase separation is common in submarine hydrothermal systems, and various analytical and computational methods have been used to characterize mineral-fluid reactions occurring in the sub-seafloor environment and the *P-T-X* conditions under which they occur (e.g., Fontaine et al., 2009; Mottl et al., 2011; Reeves et al., 2011; Seyfried et al., 2011; Von Damm, 2004). These studies document the important role of fluid-phase immiscibility on the heat and mass fluxes of these systems (e.g., Coumou et al., 2009; Fontaine and Wilcock, 2006; Foustoukos and Seyfried, 2007a; Foustoukos and Seyfried, 2007b; Lewis and Lowell, 2009a; Von Damm, 2004). Reeves et al. (2011) also observed

simultaneous venting of immiscible liquid and vapor at the seafloor, providing direct evidence of phase separation.

One of the more commonly used methods to infer sub-surface conditions involves measuring the silica content of pristine fluids collected from vents in the seafloor. The assumption employed is that the fluids were in equilibrium with quartz in the subsurface and that the fluids traversed from depth to the seafloor sufficiently fast to prevent any deposition of silica (quartz). As such, the measured silica content of the vent fluids is compared to the known quartz solubility as a function of temperature to infer the subsurface conditions (Bowers et al., 1988; Fontaine et al., 2009; Foustoukos and Seyfried, 2007a; Foustoukos and Seyfried, 2007b; Von Damm, 1995; Von Damm, 2004). For example, Bowers et al. (1988) used the dissolved silica content of vent fluids from 11°-13°N on the East Pacific Rise (EPR) to deduce that those fluids were likely in equilibrium with quartz in the subsurface. Von Damm et al. (1991) determined the solubility of quartz in hydrothermal seawater and Von Damm (2004) used the dissolved silica content of vent fluids from 9°50'N on the EPR to estimate the subsurface pressure (depth) at which quartz-fluid equilibrium occurred. Fontaine et al. (2009) refined this method by incorporating experimental work on silica partitioning between liquid and vapor phases (Foustoukos and Seyfried, 2007b), to show that when the salinity and dissolved silica concentration of seafloor vent fluids are used in combination, a unique sub-surface *P*-*T* point of liquid-vapor-quartz equilibrium can be identified.

To interpret sub-seafloor processes using vent fluid silica concentrations requires understanding the factors that control quartz solubility. The solubility of quartz in saline fluids varies with temperature, pressure and salinity (Fournier et al., 1982; Foustoukos and Seyfried, 2007b; Kennedy, 1950; Von Damm et al., 1991) (Fig. 3.1). At pressures up to about 200 MPa,

quartz solubility first increases with increasing salinity, then decreases if salinity is raised above a certain temperature and pressure-dependent value (Fournier et al., 1982; Foustoukos and Seyfried, 2007b; Von Damm et al., 1991). For example, at 350 °C and 30 MPa, quartz solubility increases with increasing salinity up to ~ 25 wt% NaCl, above which quartz solubility decreases with increasing salinity (in the present study, salinity never exceeds the local quartz solubility maximum, such that quartz solubility always increases with increasing salinity). At pressures less than about 200 MPa, quartz solubility increases with increasing temperature up to about 375 °C (this value increases somewhat with both pressure and salinity), above which the quartz solubility decreases with increasing temperature (Fournier, 1985) (Fig. 3.1). A decrease in solubility with increasing temperature at constant pressure is referred to as retrograde solubility. In sub-seafloor hydrothermal systems, the range of reaction-zone temperatures and pressures estimated from geochemical data (Fontaine et al., 2009) partly overlaps with the temperature and pressure range of retrograde quartz solubility.

Fluid phase immiscibility may have a significant impact on the dissolution, transport and precipitation of quartz (Cline et al., 1992). When fluid immiscibility occurs, dissolved silica is partitioned between liquid and vapor (Foustoukos and Seyfried, 2007b), with quartz solubility being higher in the higher-salinity liquid and lower in the lower-salinity vapor (Fig. 3.1). As a result of the different physical properties of liquid versus vapor, the two phases have different flow dynamics (Bischoff and Rosenbauer, 1989; Coumou et al., 2009; Fontaine and Wilcock, 2006; Lewis and Lowell, 2009a, b), which in turn may affect the mass transport of dissolved silica in two-phase fluids.

Numerical modeling of hydrothermal circulation in sub-seafloor hydrothermal systems (Ingebritsen et al., 2010; Lowell, 1991) has been applied to investigate many of the fundamental

processes that occur in this environment. Several modeling studies have focused on the re-distribution of silica in these systems (see Section 3.2.2, below). However, to date no study has addressed the interaction of quartz with a multi-component (H_2O-NaCl) immiscible fluid. Recent advances have allowed quantitative investigation of multi-component, multi-phase hydrothermal processes (Coumou et al., 2009; Geiger et al., 2006a; Geiger et al., 2006b; Lewis and Lowell, 2009b). In this study, we incorporate a recent model for the solubility of quartz in H_2O-NaCl fluids at elevated temperature and pressure conditions (Akinfiev and Diamond, 2009) with a numerical fluid flow model for H_2O-NaCl fluids, including the effects of liquid-vapor immiscibility and multi-phase flow (Lewis and Lowell, 2009b). In this way, we can account for the effects of varying fluid composition and chemical partitioning between liquid and vapor on quartz dissolution and precipitation in sub-seafloor systems. To understand the controls on silica transport, we employ a "de-coupled" fluid flow model and quartz dissolution/precipitation model, in which permeability (and therefore fluid flow) is not affected by the dissolution and precipitation of quartz. In reality, quartz deposition and/or dissolution will change the permeability of the system and this, in turn, will affect fluid flow behavior. Future studies are planned to better understand the role of these feedback mechanisms in the thermal and chemical evolution of sub-seafloor hydrothermal systems.

3.2.2 Background and previous studies

Studies of volcanogenic massive sulfide deposits (the "fossil" analogues of active seafloor vents) have shown that quartz is a common hydrothermal mineral in these systems (Galley et al., 2007). At the Troodos systems in Cyprus, Richardson et al. (1987) described highly silicified zones in the basal part of the sheeted dykes beneath the ore zones. These quartz-rich bodies were interpreted as relicts of the high-temperature reaction zone, where metals were leached by

hydrothermal fluid, to be later deposited as ore in the more shallow parts of the system. In addition to field evidence of quartz mineralization from VMS deposits and their associated country rocks, dredge samples from active seafloor vents sometimes contain hydrothermal quartz, and fluid inclusions hosted in this quartz have been used to study the fluid evolution in sub-seafloor hydrothermal systems (Delaney et al., 1987; Stakes and Vanko, 1986; Vanko, 1988; Vanko et al., 1992). These quartz-hosted fluid inclusions commonly show evidence of fluid-phase immiscibility (Delaney et al., 1987; Stakes and Vanko, 1986; Vanko, 1988; Vanko et al., 1992). Evidence for phase separation in sub-seafloor hydrothermal systems has also been observed in fluid inclusions in anhydrite (Vanko et al., 2004).

Cathles (1983) modeled the dissolution and precipitation of silica in sub-seafloor hydrothermal systems in a back-arc environment similar to the Kuroko volcanogenic massive sulfide deposits. Note that the geometry of the system modeled by ~~of~~ Cathles (1983) is different than that used in our simulations in that Cathles assumes a heat source along the side of the system (analogous to a dike-like intrusion) whereas in our model the heat source is on the bottom. The simulations of Cathles (1983) predict a zone of quartz dissolution near the base of the intrusive body in the fluid inflow zone, where the fluid is moving from a cooler to a hotter region, and a zone of quartz precipitation at shallower depths along the side of the intrusion and just below the seafloor. The thickness of the intrusive body used in the model by Cathles (1983) was probably too large in light of more recent seismic evidence (e.g., Canales et al., 2006; Turner et al., 1999). The model also used the properties of pure H_2O for the hydrothermal fluid, and thus did not include the effects of fluid phase immiscibility on silica transport and deposition.

Wells and Ghiorso (1991) investigated the kinetics of quartz precipitation in the upflow

zone of a sub-seafloor hydrothermal system. Their results indicated that quartz-fluid equilibrium might not be attained in the low-temperature part of a single-phase hydrothermal system wherein measured seafloor vent fluid velocities were assumed to represent the fluid velocities at depth (Wells and Ghiorso, 1991). However, mass flux estimates constrained by surface heat flow measurements imply sub-surface flow velocities several orders of magnitude less than the vent fluid velocities (Lewis and Lowell, 2004), similar to predictions from other numerical fluid flow models (e.g., Coumou et al., 2008). Similar calculations as done by Wells and Ghiorso (1991), but assuming lower flow velocities as constrained by measured heat flow, indicate that quartz-fluid equilibrium can generally be maintained throughout the system except near the surface vent.

Cline et al. (1992) studied quartz transport and deposition in boiling, pure H_2O fluids along a 1-D vertical fracture, simulating an epithermal Au system. The results showed that boiling generates a much larger amount of quartz deposition compared to non-boiling fluids flowing along the same temperature gradient (Cline et al., 1992). The enhanced quartz deposition was a result of the large mass proportion of vapor in the two-phase system.

Lowell et al. (1993) investigated the relative rate of sealing of vertical fractures by either silica precipitation or thermo-elastic stress. That study used equations describing quartz solubility in pure water and in NaCl-equivalent seawater-composition fluid. The results showed that fracture sealing and concomitant permeability reduction can occur on short time scales by both thermo-elastic closure and silica precipitation, and the relative rates of those two processes depend on the rate of fluid mass flux (Lowell et al., 1993).

Martin and Lowell (2000) studied the kinetic rate control on quartz precipitation in cracks beneath black-smoker systems. High fluid flow rates and steep temperature gradients, associated

with the discharge at and near the seafloor, result in significant differences between the equilibrium quartz precipitation (the rate controlled only by mass flux and solubility gradient) and the kinetics-controlled rate. In the present study, we focus on the deeper part of the system and restrict our analysis to fluid flow velocities that favor thermodynamic equilibrium.

3.3 Methods

3.3.1 Numerical fluid flow modeling

Fluid flow modeling was done using the package FISHES (Lewis and Lowell, 2009a, b). FISHES solves the equations for conservation of mass, momentum, energy and salt, and uses lookup tables to characterize the thermodynamic properties of the hydrothermal fluid (liquid and/or vapor) (Lewis and Lowell, 2009b). FISHES can simulate both single-phase and multi-phase fluid flow.

To illustrate the effect of vertical flow of vapor and brine on quartz dissolution and precipitation, we conducted one-dimensional (1-D) fluid flow simulations in a 2 × 50 m pipe consisting of one column divided into 25 nodes with a cell size of 2 × 2 m cells. This small cell size permits a high-resolution image of the effects of immiscibility on quartz dissolution and precipitation. The geometry and boundary conditions were similar to those used by Bai et al. (2003) and by Lewis and Lowell (2009b). The 1-D model assumed constant pressure of 28 MPa at the top of the pipe and constant heat flux of 1 W/m^2 at the bottom of the pipe. The bottom and side boundaries allowed no flow, while the top boundary allowed flow in or out of the pipe. Initially the salinity was set to 3.2 wt% NaCl (seawater salinity) and the temperature was set to 400 °C and throughout the pipe, such that the fluid was within a few degrees Celsius of the liquid-vapor immiscibility field. The 1-D model was run for several years of simulated time to

observe the effect of fluid phase immiscibility on the quartz solubility of the fluid in the pipe, to infer the dissolution and precipitation of quartz. The results of a 1-D simulation are described in section 3.4.1.

In addition to the one-dimensional simulations, we conducted 2-D simulations to investigate dissolution and precipitation of quartz in sub-seafloor hydrothermal systems. The geometry of the 2-D simulations and the starting and boundary conditions used are shown in Figure 3.2. The 2-D model consists of a 1000 m deep, 1500 m wide grid, divided into 41 by 61 nodes with a cell size of 25 × 25 m. The system depth represents the depth from the seafloor to the base of the hydrothermal convection regime, and is consistent with seismic observations of the depth to the magma chamber beneath the East Pacific Rise (Detrick et al., 1987). The depth from the ocean surface to the seafloor is assumed to be 2500 m, or a pressure of 25 MPa, at the seafloor.

The bottom boundary condition of the 2-D simulations assumes constant temperature with no mass flux. The temperature along the bottom left-most 500 m is held constant at either 400 °C or 425 °C, depending on the experiment. This range of maximum boundary temperature is consistent with results of Seyfried et al. (1991), which indicate that the reaction-zone temperatures at sub-seafloor hydrothermal systems are around 400 °C at both fast and slow spreading centers. The 500 m wide high-temperature zone represents one half of the width of the sub-axial magma chamber (AMC), and this width is consistent with seismic observations (Detrick et al., 1987; Turner et al., 1999). The bottom left of the cross-section represents the top of the conductive boundary layer above the AMC. The top of the thin conductive boundary layer is thus at a depth of 1000 m beneath the seafloor, near the top of the AMC. The depth to the AMC at seafloor spreading centers is variable, but typically on the order of 1 km (Canales et al.,

2006; Detrick et al., 1987; Turner et al., 1999). To the right of the maximum temperature zone representing the conductive boundary layer, the temperature decreases linearly from left to right to 300°C at the bottom-right corner (Fig. 2).

The boundary conditions for the sides of the 2-D grid are insulating with no mass flux. The top boundary condition is constant pressure of 25 MPa (an approximate pressure at the seafloor at a mid-ocean ridge), with temperature and salinity controlled by either the fluid from the node beneath the boundary if flow is upward (venting), or the external "ocean" water (10 °C, 3.2 wt% NaCl) if flow is downward (recharge).

All 2-D simulations were made using a homogeneous permeability distribution. The permeability of the system was set to either 10^{-14} m^2 or 10^{-13} m^2, depending on the simulation. Permeabilities of this magnitude are somewhat higher than in terrestrial hydrothermal systems (Norton, 1982) and in the continental crust in general (Manning and Ingebritsen, 1999), but appear to be reasonable for sub-seafloor systems (Lewis and Lowell, 2004). Han (2011) has conducted extensive modeling using a geometry similar to that used in the present study, but with a variety of permeabilities from 10^{-14} to 10^{-12} m^2. A qualitative assessment of the effect of varying permeability on quartz dissolution and precipitation, based on the results of Han (2011) will be discussed in Section 3.6.2.

Four 2-D simulations were conducted to examine the influence of maximum bottom temperature (400 °C or 425 °C) and permeability (10^{-14} m^2 or 10^{-13} m^2) on fluid phase immiscibility and silica transport and deposition. All simulations were continued for at least 100 years of simulated time, and the 10^{-14} m^2 simulations were run up to > 200 years. For the 10^{-13} m^2 simulations, quasi-steady state was achieved in about 30-50 years, whereas in the 10^{-14} m^2 runs quasi-steady state was reached only after about 100 years. The time-scale of the simulations, of

100-200 years, was selected because the typical lifespan of a seafloor vent field is ~ decades (Lalou et al., 1993). For example at the TAG field on the mid-Atlantic ridge, hydrothermal activity has occurred episodically for 10^5 years, but the duration of any individual period of venting was 100 years or less (Lalou et al., 1993). Thus the model time-scale reflects the approximate lifetime of a seafloor hydrothermal system.

The quartz solubility distribution and dissolution/precipitation of quartz were calculated at selected time steps from each simulation. Individual time steps were used in order to investigate the mechanisms responsible for quartz dissolution and precipitation at various locations within the convection cell. For example, at some locations quartz may precipitate as a result of cooling through the prograde temperature range, whereas in other regions quartz may precipitate as a result of heating through the retrograde solubility range. Furthermore, inspection of individual time intervals can be used to infer processes of quartz dissolution and precipitation within the region of fluid phase immiscibility. Although the quartz dissolution and precipitation modeling was conducted under quasi-steady state conditions, in all simulations hot plumes periodically detached from the bottom and drifted upward, creating transient local temperature maxima. For the quartz dissolution/precipitation modeling (Section 3.3.2), we did not include the episodes of transient plume migration to the surface in the quartz dissolution and precipitation calculations. In such cases quartz dissolution and precipitation resulting from the migrating plume were transient features that were relatively quickly overprinted by the quasi-steady state "background" dissolution and precipitation. Time slices were selected such that there were no detached plumes rising from the bottom.

For each selected time interval, the thermal profile, fluid densities and salinities (for both liquid and vapor, where present), and velocity components were used in the subsequent calculations.

3.3.2 Quartz solubility distribution, gradients and dissolution/precipitation

For each 2-D simulation, a single time interval was used to characterize the potential for quartz dissolution and precipitation. Our model assumes chemical equilibrium, so dissolution and precipitation of quartz are controlled by changes in quartz solubility. We note that in the inflow region where cold seawater enters the sub-seafloor, the basalts do not contain quartz. However, as the seawater is heated and interacts with glass and other phases in the basalts, the activity of silica in solution will increase until equilibrium with quartz is achieved. While it is clear that fluids entering the sub-seafloor are not in equilibrium with quartz and that fluids existing at vents were in equilibrium with quartz at depth, we cannot predict where along the flow path the change occurs. This could be determined using a completely coupled fluid flow and water-rock interaction model that can accommodate immiscibility in the H_2O-NaCl system. The solubility of quartz was calculated at each node in the grid as a function of temperature, salinity and density, using the semi-empirical model of Akinfiev and Diamond (2009). Where two fluid phases (liquid and vapor) were present, the quartz solubility was calculated in both the liquid and the vapor phases. The bulk quartz solubility, in this case, was found from mass balance based on the mass fractions of liquid and vapor present. This calculation yielded a distribution of quartz solubility in the system, which was contoured to identify regions in which quartz solubility was higher or lower than in surrounding areas. Dissolution or precipitation of quartz was determined by the gradient in quartz solubility between nodes and by the fluid flux across that gradient.

Mass fluxes across each interface were found by multiplying the Darcy velocity (m/s) by the density (kg/m^3) of the fluid on the upstream side, i.e. the side from which fluid flows. For example, if the flow direction across an interface is from a cell with density *x* into a cell with density *y*, then the fluid has density *x*, but if the flow direction were reversed then the fluid would have density *y*. Likewise, the quartz solubility gradient was calculated *in the direction of the mass flux* between two cells. For example, if fluid is flowing from cell *p* into cell *q*, then the quartz solubility gradient should be calculated as *solubility in cell q minus the solubility in cell p,* over the distance between cells, etc. This method ensured consistent assignment of positive values if quartz is being dissolved and negative values if quartz is being precipitated. The rate of quartz dissolution or precipitation at a node (center of each cell) is the sum of the rates at each adjacent interface (four per cell in most cases) that has the flow direction *into* the cell (flow out of the cell does not contribute to the dissolution/precipitation in the cell, but rather contributes to the neighboring cell).

The rate of quartz dissolution or precipitation is expressed as

$$R = \rho_f \vec{u} \cdot \nabla c_e(T, P, S) \tag{3.1}$$

where R is the volume-normalized rate in mol/m^3·s, ρ_f is the fluid density in kg/m^3, $\vec{u}$ is the Darcian velocity vector in m/s, ∇ is the gradient operator (m^{-1}), and c_e is the equilibrium concentration of quartz in solution (molality, mol/kg) as a function of temperature, pressure and salinity (e.g., Phillips, 1991). Note that the calculated rate is *not* related to the kinetic rate of quartz-fluid interaction, instead representing the rate at which quartz would be dissolved or precipitated to maintain equilibrium at the given flow rates as fluid moves along pressure,

temperature, and/or salinity gradients. Over most of the range of P-T conditions considered here, this assumption is reasonable.

Quartz dissolution and precipitation in the two-phase region and at the interface between single-phase and two-phase conditions represent a special case in that vapor and brine each flow separately. Thus the transport of silica must be monitored in each of the two fluid phases. Therefore where two fluid phases coexist in our simulations, the solubility gradient term in Equation (3.1) is modified to reflect the transport of silica by both vapor and brine. For example, where single-phase fluid enters *P-T* conditions of immiscibility, quartz solubility gradients are functions of the quartz solubilities of the vapor and brine and the mass-balanced proportions of vapor and brine produced during phase separation. Where vapor and brine coexist, silica transport is influenced by the different flow dynamics of vapor versus brine. The lower-density vapor is more buoyant than brine, thus the quartz solubility gradient across the two-phase to single-phase interface is largely controlled by the increase in quartz solubility resulting from condensation of vapor (e.g., Fig. 3.1). The separate contributions to silica transport by vapor and brine are explicitly accounted for in determining dissolution and precipitation of quartz, by computing quartz solubility gradients individually for each of the liquid and vapor phases.

The rate of change of porosity was calculated from the rate of dissolution or precipitation of quartz using the expression

$$\frac{d\phi}{dt} = R\frac{M_{SiO_2}}{\rho_{quartz}} \tag{3.2}$$

where ϕ is porosity, t is time in seconds, ρ_{quartz} is the density of quartz in kg/m^3 and M_{SiO_2} is the molar mass of SiO_2 in kg/mol. Equation (3.2) is equivalent to the expression for rate of porosity change described by Wood and Hewett (1982), neglecting any contribution from diffusion.

3.4 Results

3.4.1 One-dimensional simulation of dissolution and precipitation in two-phase flow regime

Figure 3 shows the results of the one-dimensional fluid flow model during ten years of simulation time. After the first year, a ~4 m thick region of two-phase conditions has developed at the bottom of the pipe (see the liquid saturation at one year, Fig. 3.3). The two-phase region is a result of gradual temperature increase, resulting from the constant heat flux boundary condition. As soon as two-phase conditions are established, the lower-density vapor phase preferentially ascends to the upper part of the two-phase region whereas the higher-density brine accumulates towards to base of the pipe (Fig. 3.3). The two-phase region expands upwards as time progresses, and meanwhile the base of the pipe becomes increasingly liquid-rich whereas the upper portion of the two-phase region becomes increasingly vapor dominated with time (Fig. 3.3). Consequently, the quartz solubility at any point within the two-phase region (with the exception of the bottom two meters) decreases with time (Fig. 3.3), as the liquid descends and vapor ascends through the two-phase region.

As a result of quartz solubility evolution with time, quartz is precipitated and dissolved at various regions in the pipe at different time intervals. The dominant mechanisms of quartz precipitation and dissolution are phase-separation of descending liquid and condensation of ascending vapor, respectively (Fig. 3.3). Consider the dynamics of the 1-D simulation at a single time interval. At the interface between two-phase conditions (below) and single-phase conditions

(above), low-density vapor tends to rise and condense. Condensation of vapor promotes a significant increase in the quartz solubility in that fluid, thus quartz can be dissolved by condensing vapor even if the fluid is cooled in the process (Fig. 3.1). Meanwhile, the relatively higher-density single-phase liquid above the interface may tend to descend, intersecting the P-T conditions of phase separation. When phase separation occurs, the brine salinity increases to greater than 10 wt% NaCl within a few degrees Celsius, while the vapor salinity is mostly less than 1 wt% NaCl. Because the initial salinity in the 1-D (and 2-D) simulations is 3.2 wt% NaCl, phase separation produces a large mass fraction of vapor and comparatively little liquid, thus the bulk quartz solubility is initially dominated by the vapor fraction (Figs. 3.1 & 3.3). The same process occurs not only at the interface between single-phase and two-phase conditions, but also within the upper several meters of the two-phase field itself, where descending liquid phase-separates further to yield yet more vapor. Thus quartz is precipitated as a result of phase-separation of descending liquid. However, in the deeper part of the two-phase region, descending liquid evolves comparatively little vapor, and the very bottom of the pipe is dominated by accumulated high-salinity brine (Fig. 3.3).

3.4.2 Thermal profiles and velocity vectors

The geometry and boundary conditions used in the 2-D model promote quasi-steady state circulation after a few decades in the case of the 10^{-13} m^2 simulations and after about 100 years in the 10^{-14} m^2 simulations. At quasi-steady state, fluid flow vectors may shift slightly with time and hot plumes may periodically detach from the bottom and migrate upwards (as discussed in Section 3.3.1), but the overall convection cell and thermal profile remain more or less constant over several 10's to 100's of years (also see Section 3.6.1, below). In the present study, all the quartz dissolution and precipitation modeling in the 2-D simulations was conducted under quasi-

steady state conditions. Thus the fluid flow vectors and quartz solubility distributions shown here for specific time intervals have the same general features as other (earlier or later) time intervals. In addition, static spatial gradients of temperature and quartz solubility in the 2-D cross-sections reflect the dynamic spatial and temporal fluid evolution at quasi-steady state conditions.

The patterns of fluid circulation for the four simulations are shown in Figure 3.4. In the lower permeability runs ($k = 10^{-14}$ m^2), the fluid flows mostly horizontally along the bottom from the cooler side to the hotter side (Fig. 3.4, left-hand side). In comparison, the higher permeability runs ($k = 10^{-13}$ m^2) show more irregular upward movement of the horizontally flowing fluid, as pulses of fluid rise away from the bottom as they are heated, and then descend a short horizontal distance away when they cool slightly (Fig. 3.4, right-hand side).

The main effect of varying the maximum bottom temperature from 400 °C to 425 °C is that liquid-vapor immiscibility occurs when the bottom temperature is 425 °C (Fig. 3.4, white vectors), but liquid-vapor immiscibility is not observed when the bottom temperature is 400 °C. In all simulations, the bottom pressure exceeds 30 MPa, which is the critical pressure of seawater. In the immiscibility region the bulk salinity increases rapidly to about 15 wt% NaCl once phase separation begins, as predicted by Bischoff and Rosenbauer (1989), and as a result the seawater critical point is not relevant to characterizing the nature of phase separation. Because the terms sub- and supercritical are ambiguous when considering a multi-component system, we avoid using these terms here to describe phase separation in the H_2O-NaCl system.

In all four of the 2-D simulations, the boundary conditions and permeability are such that the rate of heat extraction exceeds the rate at which heat is supplied by crustal construction as a result of seafloor spreading. Modeling by Liu and Lowell (2009) has shown that heat extraction from a crystallizing magma chamber by overlying hydrothermal convection would result in vent

fluid temperature reduction of hundreds of degrees Celsius in a matter of years. Vent fluid temperatures would be reduced to less than the lower limit of black smoker venting within about one decade without magma replenishment. Thus Liu and Lowell argued that magma replenishment is required to explain observed high-temperature hydrothermal systems, which persists for several decades. Nooner and Chadwick (2009) monitored seafloor uplift at Axial seamount and linked the observed inflation rates to influx of magma from below. Similar rates of magma replenishment were inferred by Liu and Lowell (2009) based on heat flow constraints, and by Nooner and Chadwick (2009) based on seafloor inflation observations. Rates of magma replenishment in both cases exceed the rate of crustal production (Liu and Lowell, 2009; Nooner and Chadwick, 2009). The high heat-extraction rates in the present study are consistent with these modeling and observational studies of mid-ocean ridge hydrothermal systems.

3.5 Quartz solubility distribution and evolution along channels of high fluid mass flux

Figures 3.5 and 3.6 show quartz solubility variations throughout the hydrothermal system (upper plot) and the variation in quartz solubility (middle) and temperature (bottom plot) along the main channels of hydrothermal fluid flow. The arrows on Figures 3.5 and 3.6 represent pathways in which the magnitude of mass flux is significantly higher than in the surroundings. These paths account for about 50 % of the horizontal mass flux through any vertical slice and about 50 % of the vertical mass flux through any horizon within the cross-section. The simulations in Figures 3.5 and 3.6 assume a permeability of 10^{-13} m^2 and bottom temperature of 400 °C (Fig. 3.5) or 425 °C (Fig. 3.6). The vector arrows on each diagram trace the paths along which the fluid mass flux is at a maximum (other vector arrows outside the main flow channels, as seen in Fig. 3.4, have been removed for clarity). These main arteries of fluid flow can be used to infer how quartz solubility varies with temperature along the length of the convective cell.

Fluid phase immiscibility (Fig. 3.6, middle, pink-shaded box) occurs only in the simulations with a maximum bottom temperature of 425 °C. In the simulations with a maximum bottom temperature of 400 °C, where immiscibility does not occur (Fig. 3.5), the salinity remains constant at seawater salinity (3.2 wt% NaCl) throughout, and quartz solubility variation is due almost entirely to temperature, with only a slight effect of pressure. In the simulations in which immiscibility occurs, the salinities of the two coexisting phases differ from seawater salinity as a result of phase separation, and quartz solubility is affected by both temperature and salinity. The difference in maximum bottom temperature (25 °C) between the two simulations was deliberately chosen to be small, so that any differences observed between the two simulations could be attributed to the effects of immiscibility. In other words, fluid temperature controls the quartz solubility variation along the flow path in the 400 °C simulation, whereas differences between the 400 °C simulation and the 425 °C simulation can be attributed to the effect of immiscibility and the concomitant effect on salinities and densities of the coexisting phases.

The fluid flux vectors shown on Figures 3.5 and 3.6 show the directions of fluid flow from each cell into its adjacent cell during a short time interval, although they do not necessarily reflect the long-term flow directions throughout the whole convection cell. Because the model assumes quartz-fluid equilibrium, local mass fluxes between adjacent cells determine the magnitude of quartz dissolution and precipitation rates over the selected time interval. Thus we consider how quartz solubility evolves as fluid flows from one cell to the next, but we are not concerned with the long-distance fate of any particular fluid aliquot. In the simulation in which the maximum bottom temperature is 400 °C (Fig. 3.5), fluid is heated as it flows laterally from right to left along the bottom. Thus fluid temperature along the bottom is lowest at point a (far right) and increases in the direction of point c (above the heat source) (Fig. 3.5, bottom).

Consequently, the solubility of quartz in the fluid increases as a result of leftward flow and heating within the interval between points a and b, but then decreases as fluid flows left and is heated between points b and c owing to the retrograde solubility of quartz in this *P-T* region (Fig. 3.5, middle – the yellow-shaded areas). The temperature is constant between points c and d, because this part of the bottom boundary represents the top of the conductive boundary layer above the AMC. Where the fluid rises away from the bottom, it begins to cool (Fig. 3.5, bottom, point d), and the solubility of quartz first increases slightly (owing to retrograde solubility) then decreases more or less steadily in the interval from point d to point e (Fig. 3.5, middle).

In the simulation in which the maximum bottom temperature is 425 °C (Fig. 3.6), the temperature profile and especially the silica transport are affected by phase separation (shown in pink in Fig. 3.6, middle). As in the 400 °C simulation, the fluid heats up as it flows to the left within the interval from point a to point c. Meanwhile the solubility of quartz increases as a result of temperature increase between points a and b. Quartz solubility decreases as the fluid flows leftward and is heated in the region between points b and c owing to the retrograde solubility of quartz in this *P-T* region. At point c, the temperature and pressure are such that the liquid-vapor field is intersected and the fluid separates into a higher-salinity liquid (brine) coexisting and in equilibrium with a lower-salinity vapor. The quartz solubility in the brine (black curve) is higher than the quartz solubility in the vapor (green curve), while the bulk quartz solubility is found from the mass fractions of each of those phases present (the intermediate blue curve in the pink box, Fig. 3.6 middle). Also note that there is a discontinuity between the quartz solubility in the single-phase fluid and that in the vapor, whereas there is no discontinuity between the quartz solubility in the single-phase fluid and that in the brine. This reflects the fact that phase separation occurs below the critical temperature for the bulk composition, which is

well above seawater salinity owing to brine sinking, as discussed in Section 3.4.1 and by Fontaine and Wilcock (2006). As fluid rises (in different proportions depending on the relative permeability and relative buoyancy) away from the bottom and cools, it goes back into the single-phase field at point d (Fig. 3.6) and a narrow zone of retrograde quartz solubility develops and quartz dissolves. Finally, quartz solubility decreases more or less steadily as fluid ascends and cools within the region between point d and the seafloor.

As mentioned in Section 3.4.1, fluid phase immiscibility has significant effects on the quartz solubility trends. Owing to the separate flow of the brine and vapor phases, the bulk quartz solubility gradients on Figure 3.6 are not necessarily representative of the changes in quartz solubility related to vapor and brine flow. Two thin black arrows are sketched on Figure 3.6 to highlight the effects of vapor versus liquid flow. First, low-density vapor is relatively buoyant and tends to rise out of the two-phase region (curve *i* on Fig. 3.6). Rising vapor condenses, thus the quartz solubility increases significantly as a result of vapor ascent. Conversely, single-phase liquid from above the two-phase region may tend to descend in response to vapor ascent (curve *ii* on Fig. 3.6). Descending low-salinity liquid separates into a large fraction of vapor and a small fraction of liquid, such that the bulk quartz solubility in that descending fluid aliquot decreases significantly as a result of immiscibility. Notice that these changes in quartz solubility in the vicinity of the two-phase/single-phase interface do not reflect the bulk quartz solubility in the two-phase region. Instead, these changes in quartz solubility result from the separate, individual flow of the vapor and liquid phases.

3.5.1 Quartz dissolution and precipitation

The rate of quartz dissolution and precipitation predicted from fluid mass fluxes between nodes is shown for the 400 °C, 10^{-13} m^2 simulation at various time intervals from 20 to 100 years of

simulated time in Figure 3.7. Comparison of the dissolution and precipitation distributions at various times demonstrates the quasi-steady state nature of the simulations. During the first few decades of the simulations, the areas of quartz dissolution and precipitation change noticeably as time advances. This reflects the fact that at earlier time intervals the temperature field has not stabilized. The broad zone of dissolution in the upper-right part of the system in the early stages is related to the temperature distribution resembling a static/conductive scenario (i.e., resembling time zero). As fluid circulation is established during the first few decades, the thermal field becomes more advection-dominated. Meanwhile, during the early stages (up to ~50 years), the flow from right to left across the bottom and from bottom to top up the main plume are not well established into a smooth artery. Instead, in those early time slices, the cross flow is discontinuous as pulses of fluid migrate up from the bottom in numerous places. After ~ 60 years, the zones of quartz dissolution and precipitation (especially along the main flow path) are relatively constant through time. Similar explanations apply also to the other simulations (the other permeability/maximum temperature runs).

Figure 3.8 shows the quartz dissolution and precipitation rates at selected quasi-steady state time intervals for each of the four 2-D simulations with different permeability and maximum temperature settings. Some common features in the quartz dissolution/precipitation profiles are observed in all four simulations. Quartz, if present, is dissolved in the lower right inflow part of the system as cold seawater is heated as it flows downward into the subsurface and then from right to left towards the heat source (Fig. 3.4). In all four simulations a small zone in which quartz is precipitated as the fluid heats up (retrograde solubility) develops around the bottom-center of the flow path. A zone of quartz precipitation develops in the middle of plumes that form at the left side boundary and about 300 m from the left side. Quartz is dissolved along

the sides of the plume, where fluid that did not quite reach the surface (and seawater that is drawn into the near-plume recharge zone) is heated as it descends, and where this colder fluid is drawn laterally back into the plume itself. Zones of quartz precipitation occur at the basal part of the sides of the plumes in the higher-temperature simulations, as described below. A zone of quartz precipitation is present towards the top of the plume, just beneath the vent where fluid approaches cold seawater. However, quartz precipitated in this upper region may later be dissolved when a later hot pulse of fluid rises through this region. It should be noted that the distribution of zones of quartz dissolution and precipitation shown in Figure 3.8 represent one time interval in an evolving system, and these zones migrate somewhat with time (Fig. 3.7). However, the main features are relatively constant within the conduits of high mass flux (Figs. 3.5-3.7).

The rates of quartz dissolution and precipitation increase with increasing permeability (notice the different z-axis scaling on the 10^{-14} versus 10^{-13} m^2 plots in Figure 3.8). The increase in rate of dissolution and precipitation is a result of the higher mass fluxes that are achieved in the higher-permeability simulations.

The rate of quartz dissolution and precipitation also increases with increasing maximum bottom temperature. As mentioned earlier, the actual difference in maximum bottom temperature used in our simulations is only 25 °C, so the change in rate is unlikely to be the result of the change in quartz solubility with temperature. For example, at a pressure of 36 MPa, which is slightly above the immiscibility curve at both 400 ° and 425 °C, quartz solubility at these two temperatures differs by only 4.5 mmolal, and because quartz solubility is retrograde under those *P-T-X* conditions, quartz would be dissolved during cooling from 425 to 400 °C. Thus, the higher quartz precipitation and dissolution rates observed at increased temperature are the result

of fluid phase immiscibility that occurs in the higher-temperature simulations, and not the result of the slightly higher temperatures. In the 425 °C simulations in which immiscibility occurs, an area of rapid quartz precipitation develops in the *P-T* region of two-phase conditions at the bottom of the flow system (Fig. 3.8, top two plots, lower left).

In the 10^{-13} m^2/400 °C simulation (Fig. 3.8; bottom right), small plumes of hot fluid rise adjacent to the main upflow zone (Fig. 3.4, lower right, middle part of the plot) and cause some dissolution and re-precipitation of quartz in the middle part of the system (Fig. 3.8, lower right, middle part of the plot). The small plumes do not rise to the seafloor even after long simulation times, and they appear to be a result of convection within the near-plume recharge zone. They are not transient features, although they move around somewhat with time. Therefore, dissolution and precipitation of quartz in the vicinity of these small plumes is not well constrained.

3.6 Discussion

3.6.1 Quartz dissolution and precipitation in the sub-seafloor

The fluid flow paths and temperature and quartz solubility trends shown in Figures 3.5 and 3.6 provide insight into the processes driving quartz dissolution and precipitation throughout the system. Quartz dissolution and quartz precipitation occur at both prograde and retrograde solubility conditions at different points within the system (Figs. 3.5 & 3.6). Along the bottom of the system, quartz solubility changes from prograde quartz dissolution to retrograde quartz precipitation with increasing temperature, as the fluid flows from the base of the recharge zone on the right towards the heat source on the left-hand side (Fig. 3.8). In the upflow part of the system, quartz is mostly precipitated in the center of the upwelling plume and is dissolved along

the sides where flow is downward and into the plume. These features are common in all simulations, independent of whether immiscibility is absent or present (Fig. 3.8).

The most obvious effect of liquid-vapor immiscibility is the development of a region of quartz precipitation just above the "magma chamber" where immiscibility occurs (Fig. 3.8, upper plots). The reason for this behavior can be seen in Figure 3.6 (the middle plot). In the zone of fluid phase immiscibility in the 425 °C simulations, vapor ascends and condenses, dissolving quartz (if present) above the two-phase to one-phase interface (curve *i* on Fig. 3.6). Meanwhile, single-phase liquid from above descends and phase-separates to produce much vapor and little brine (curve *ii* on Fig. 3.6). Phase-separation of fluid with near-seawater salinity, and the resulting production of a large proportion of vapor, results in an abrupt quartz solubility decrease. This result is similar to that predicted for pure H_2O fluids by Cline et al. (1992). Decrease in quartz solubility results in quartz precipitation in the region of immiscibility, coupled with quartz dissolution above. Dissolution and precipitation in the vicinity of the two-phase region are localized at the base of the plume and the down-going re-charge channel. Concomitant permeability evolution there may have significant consequences for the evolution of sub-seafloor hydrothermal systems, as discussed below.

The volume-normalized rates of quartz precipitation/dissolution shown in Figure 3.8 range up to about 10^{-6} mol/m^3·s, or from Equation (3.2), up to about 0.035 cubic meters of quartz per cubic meter of rock per year. To put this value into perspective, the time required to fill the available pore space in a given rock volume can be estimated from

$$t = \frac{\phi_{initial}}{-d\phi / dt} \tag{3.3}$$

where $d\phi/dt$ is the change in porosity with time from Equation (3.2). If we consider a system with 10% porosity, the pore space would be entirely filled in about 140 years at a rate of quartz precipitation of 10^{-6} mol/m^3·s. Note that this time period, 140 years, is comparable to the lifetime of a seafloor hydrothermal system as described in Section 2.1. It is important to note that this rate of quartz precipitation would not likely be maintained for 140 years while the pore space became increasingly filled with quartz. Quartz precipitation would tend to reduce permeability, thereby decreasing fluid flow rates, which would cause the rate of precipitation to also decrease. This calculation simply demonstrates that quartz-fluid interaction can cause significant re-distribution of porosity and permeability on relatively short timescales. Once again we emphasize that we do not expect quartz precipitation to sustain the maximum observed rates for more than a fraction of the 140-year time period.

The results presented here are for an initially homogeneous permeability distribution and, as noted above, the localized higher rates of dissolution and precipitation will tend to quickly alter the permeability profile and redistribute the fluid flow patterns. Likewise, if we imagine an initial condition in which permeability is not uniform (as in real-world hydrothermal systems), dissolution and precipitation of quartz are certain to affect the fluid flow behavior. Because the rate of quartz precipitation is largely controlled by the mass flux, regions of initially large permeability will tend to clog faster than regions of initially lower permeability. Hence quartz precipitation will tend to homogenize a medium in which the permeability is initially heterogeneous. This is not the case when silica precipitation is kinetically controlled (as pointed out by Martin and Lowell (2000)). The converse would be true in regions of dissolution, where initially high-permeability regions would increase permeability at the expense of low-

permeability ones, thus tending to generate heterogeneous permeability over time. Effects of heterogeneous permeability and permeability evolution will be the focus of a future study.

Quartz precipitation in the region of fluid phase immiscibility may be an explanation for the extremely silicified "epidosites" found beneath VMS deposits. At the Troodos ore-forming hydrothermal systems of Cyprus, the basal part of the sheeted dykes is intensely hydrothermally altered to epidosite, a quartz-rich alteration assemblage that occurs in pods and lenses (Richardson et al., 1987). The epidosites are interpreted as the locus of high-temperature water-rock interaction that liberates metals that are later deposited in other parts of the system to form the VMS ore bodies (Richardson et al., 1987). The spatial distribution of the epidosites with respect to the VMS ore bodies (underneath the ore bodies vertically, and at the bottom of the sheeted dyke layer) is consistent with the location of the zone of quartz precipitation found in the simulations with immiscibility. Furthermore, fluid inclusions in the quartz in the epidosites commonly contain halite daughter minerals (Banerjee et al., 2000; Kelley et al., 1992; Richardson et al., 1987), indicating quartz precipitation in the presence of high-salinity brines.

Quartz precipitation resulting from fluid phase immiscibility occurs just above the conductive boundary layer the bottom of the plume. Coumou et al. (2008) showed that for sub-seafloor hydrothermal systems operating at a state of maximum energy transport, recharge close to the plume (i.e., descending colder fluid along the sides of the plume) is a major heat transfer pathway. The simulations of Coumou et al. (2008) used pure water as the fluid and assumed that phase separation does not change the heat budget. The results of this study suggest that when phase separation occurs, quartz precipitation within the zone of heat exchange at the base of the plume may reduce the permeability in that zone, altering the heat transport in these systems.

Quartz precipitation in the region of fluid-phase immiscibility may assist in immobilizing the brine layer. Bischoff and Rosenbauer (1989) suggested that brine produced by fluid phase separation in sub-seafloor hydrothermal systems may occupy a stably-stratified lowermost layer just above the magmatic heat source. Fontaine and Wilcock (2006) argued that brine may segregate into narrower subordinate fractures throughout the system while vapor dominates the main fracture conduits. Seafloor vent fluid salinities are usually less than seawater salinity (Von Damm, 1995), but numerical simulations of sub-seafloor hydrothermal convection commonly show alternating low- and high-salinity venting over short time-scales (Han, 2011; Lewis and Lowell, 2009a). Results of this study suggest that brine, produced by phase separation above the magmatic heat source, may be partially immobilized by quartz precipitation. If brine is detained at depth via permeability reduction, this would reduce the likelihood of observing high-salinity fluids venting at the seafloor, consistent with observed seafloor vent salinities (Von Damm, 1995). Michael and Cornell (1998) and Wanless et al. (2010) suggested that Cl-enriched basalts at mid-ocean ridges may be the result of magma incorporating brine-rich crustal material. On the other hand, brine storage resulting from a permeability decrease in the two-phase region may be offset by brine release due to thermal or tectonic cracking, which are beyond the scope of this paper.

The discussion thus far has focused on the regions of most rapid quartz dissolution and precipitation. More moderate rates of quartz-fluid interaction may affect fluid flow over longer time scales. At a fast spreading ridge (~ 5 cm/year half-rate), a hydrothermal convection cell of ~ 1 km diameter would remain in the ridge axis zone for ~ 20,000 years. Thus even if hydrothermal activity occurred during only 10 % of the time, the effective lifetime of hydrothermal circulation in the ridge axis zone would be 2000 years. On this time scale quartz

precipitation related to successive hydrothermal episodes could significantly alter flow geometries even if relatively little change occurred during any given episode.

3.6.2 Notes on simplifications

In the de-coupled fluid-flow and quartz dissolution/precipitation model, the fluid flow is not influenced by dissolution/precipitation of quartz because time-dependent permeability changes resulting from dissolution/precipitation are not included in the model. In reality, dissolution and precipitation of quartz can significantly alter the permeability of the system (Lowell et al., 1993), thereby affecting the fluid flow pathways and mass transfer. The de-coupled simplification therefore does not include the feedback mechanisms that will result when quartz-fluid interaction is allowed to affect the porosity/permeability. In addition, the present quartz dissolution and precipitation modeling was conducted at quasi-steady state, but permeability evolution resulting from porosity change may cause similar simulations to move out of quasi-steady state. For the moment, it was important to treat the fluid-flow and quartz dissolution/precipitation effects separately, in order to better understand the causes of quartz dissolution and/or precipitation. Future work will examine the influence of quartz dissolution/precipitation on permeability, to determine if and how the fluid flow is affected.

The model presented here is an equilibrium model. We assume that quartz-fluid equilibrium is maintained throughout the system. The "rates" of quartz dissolution and precipitation reported here represent the amount of silica that would be removed from or added to the fluid phase per unit time, to maintain equilibrium at the fluid flow rates being considered. Evidence for quartz-fluid equilibrium is sometimes observed in real-world seafloor hydrothermal systems (e.g., Bowers et al., 1988). However, equilibrium between quartz and hydrothermal fluids may not always be maintained in these systems (Martin and Lowell, 2000; Wells and

Ghiorso, 1991). There are many examples of seafloor vents that are quartz-supersaturated (Fontaine et al., 2009), indicating fluid flow rates that overwhelm the kinetics of quartz precipitation, and Seyfried et al. (2011) observed vent fluids that were quartz-undersaturated at 36°N on the Mid-Atlantic Ridge. We emphasize that the results of this model are most applicable to the deeper, hotter parts of intermediate-to-felsic- or altered-basalt-hosted systems in which quartz occurs, and may not be appropriate for systems that are quartz-undersaturated.

The present modeling included only two homogeneous permeabilities, in order to evaluate the general effect of permeability on quartz dissolution and precipitation locations and rates in the sub-seafloor. We can qualitatively assess the effects of further variation of permeability based on the results of Han (2011). Han conducted extensive modeling using a similar geometry to that used here, but with more variations in permeability. The results of Han (2011) demonstrate that as permeability is increased, the high-temperature plume develops a finer structure. At permeability of 10^{-12} m^2 a single plume rises to the seafloor, but as permeability is increases the plume separates into multiple cusps. However, the thermal profile is similar along the height of the plume and the vent temperature is essentially identical regardless of the permeability. Meanwhile both the mass and heat fluxes increase with permeability. Based on those results we can expect that if permeability were, say, higher than in our simulations, then the regions of quartz dissolution and precipitation would be more or less the same, but the rates of dissolution and precipitation would be greater than those shown here.

3.7 Conclusions

A relatively simple examination of the dissolution and precipitation of quartz in sub-seafloor hydrothermal systems reveals considerable complexity, including the effects of retrograde solubility and fluid-phase immiscibility. Both higher permeabilities and higher temperatures

favor increased re-distribution of quartz by hydrothermal fluids. Higher permeability favors increased mass fluxes, and higher temperature results in slightly higher quartz solubility and also increases the likelihood that the fluids will undergo phase separation or immiscibility. Immiscibility creates a zone of enhanced precipitation directly above the heat source at the bottom of the system, which is not observed when immiscibility is absent. Quartz precipitation occurs as a result of fluid-phase immiscibility, at rates up to 700 cubic centimeters of quartz per cubic meter of rock per year. Quartz precipitation at the top of the conductive boundary layer may reduce the efficiency of heat transfer in that region and influence the mobility of high-salinity brine. In addition, this region appears to roughly overlap with the sites of localized alteration to quartz-rich epidosites in VMS-bearing ophiolites. The results of this study highlight the significance of multi-component, multi-phase modeling in understanding the processes at work in the sub-seafloor hydrothermal environment. These results provide a starting point for fully coupled fluid flow and water/rock reaction modeling, in which dissolution and precipitation of quartz feed back via time-dependent porosity and permeability variations and the concomitant effects on fluid flow and mass transfer.

3.8 References

Akinfiev, N. N., Diamond, L. W., 2009. A simple predictive model of quartz solubility in water-salt-CO_2 systems at temperatures up to 1000 °C and pressures up to 1000 MPa. *Geochimica et Cosmochimica Acta* **76**, 1597-1608.

Alt, J. C., 1995. Subseafloor processes in mid-ocean ridge hydrothermal systems, in: Humphris, S.E., Zierenberg, R.A., Mullineaux, L.S., Thomson, R.E. (Eds.), *Geophysical Monograph* **91**. American Geophysical Union, Washington DC, pp. 85-114.

Bai, W., Xu, W., Lowell, R.P ., 2003. The dynamics of submarine geothermal heat pipes. *Geophysical Research Letters* **30**, 3-4.

Banerjee, N. R., Gillis, K. M., Muehlenbachs, K., 2000. Discovery of epidosites in a modern oceanic setting, the Tonga forearc. *Geology* **28**, 151-154.

Bischoff, J. L., Pitzer, K. S., 1985. Phase relations and adiabats in boiling seafloor geothermal systems. *Earth and Planetary Science Letters* **75**, 327-338.

Bischoff, J. L., Rosenbauer, R. J., 1989. Salinity variations in submarine hydrothermal systems by layered double-diffusive convection. *Journal of Geology* **97**, 613-623.

Bowers, T. S., Campbell, A. C., Measures, C. I., Spivack, A. J., Khadem, M., Edmond, J. M., 1988. Chemical controls on the composition of vent fluids at 13°-11°N and 21°N, East Pacific Rise. *Journal of Geophysical Research* **93**, 4522-4536.

Canales, J. P., Singh, S. C., Detrick, R. S., Carbotte, S. M., Harding, A., Kent, G. M., Diebold, J. B., Babcock, J., Nedimovic, M. R., 2006. Seismic evidence for variations in axial magma chamber properties along the southern Juan de Fuca Ridge. *Earth and Planetary Science Letters* **246**, 353-366.

Cathles, L. M., 1983. An analysis of the hydrothermal system responsible for massive sulfide deposition in the Hokuroku Basin of Japan, in Ohmoto, H., Skinner, B.J. (Eds.), *Economic Geology Monograph* **5**. pp. 439-487.

Cline, J. S., Bodnar, R. J., Rimstidt, J. D., 1992. Numerical simulation of fluid flow and silica transport and deposition in boiling hydrothermal solutions; application to epithermal gold deposits. *Journal of Geophysical Research* **97**, 9085-9103.

Coumou, D., Driesner, T., Heinrich, C. A., 2008. The Structure and Dynamics of Mid-Ocean Ridge Hydrothermal Systems. *Science* **321**, 1825-1828.

Coumou, D., Driesner, T., Weis, P., Heinrich, C. A., 2009. Phase separation, brine formation, and salinity variation at Black Smoker hydrothermal systems. *Journal of Geophysical Research* **114**, B03212.

Delaney, J. R., Mogk, D. W., Mottl, M. J., 1987. Quartz-cemented breccias from the Mid-Atlantic Ridge; samples of a high-salinity hydrothermal upflow zone. *Journal of Geophysical Research* **92**, 9175-9192.

Detrick, R. S., Buhl, P., Vera, E. E., Mutter, J. C., Orcutt, J. A., Madsen, J. A., Brocher, T. M., 1987. Multi-channel seismic imaging of a crustal magma chamber along the East Pacific Rise. *Nature* **326**, 35-41.

Fontaine, F. J., Wilcock, W. S. D., 2006. Dynamics and storage of brine in mid-ocean ridge hydrothermal systems. *Journal of Geophysical Research* **111**, B06102.

Fontaine, F. J., Wilcock, W. S. D., Foustoukos, D. E., Butterfield, D. A., 2009. A Si-Cl geothermobarometer for the reaction zone of high-temperature, basaltic-hosted mid-ocean ridge hydrothermal systems. *Geochemistry Geophysics Geosystem*s **10**, Q05009.

Fournier, R. O., 1985. The behavior of silica in hydrothermal solutions. *Reviews in Economic Geology* **2**, 45-61.

Fournier, R. O., Rosenbauer, R. J., Bischoff, J. L., 1982. The solubility of quartz in aqueous sodium chloride solution at 350°C and 180 to 500 bars. *Geochimica et Cosmochimica Acta* **46**, 1975-1978.

Foustoukos, D. I., Seyfried, W. E., 2007a. Fluid phase separation processes in submarine hydrothermal systems. *Reviews in Mineralogy and Geochemistry* **65**, 213-239.

Foustoukos, D. I., Seyfried, W. E., 2007b. Quartz solubility in the two-phase and critical region of the NaCl-KCl-H_2O system; implications for submarine hydrothermal vent systems at 9°50'N East Pacific Rise. *Geochimica et Cosmochimica Acta* **71**, 186-201.

Galley, A. G., Hannington, M., Jonasson, I., 2007. Volcanogenic massive sulphide deposits, in: Goodfellow, W.D. (Ed.), *Mineral Deposits of Canada: A Synthesis of Major Deposit-types, District Metallogeny, the Evolution of Geological Provinces, and Exploration Methods*. Special Publication 5, Mineral Deposits Division, Geological Association of Canada, pp. 141-161.

Geiger, S., Driesner, T., Heinrich, C., Matthäi, S., 2006a. Multiphase thermohaline convection in the earth's crust: II. Benchmarking and application of a finite element – finite volume

solution technique with a NaCl–H_2O equation of state. *Transport in Porous Media* **63**, 435-461.

Geiger, S., Driesner, T., Heinrich, C. A., Matthai, S. K., 2006b. Multiphase thermohaline convection in the Earth's crust: I. A new finite element-finite volume solution technique combined with a new equation of state for NaCl-H_2O. *Transport in Porous Media* **63**, 399-434.

Han, L., 2011. Exploring two-phase hydrothermal circulation at a surface pressure of 250 bar: Implications for EPR 9°50'N. MSc. Thesis, Virginia Tech, Blacksburg VA USA. 87 p.

Ingebritsen, S. E., Geiger, S., Hurwitz, S., Driesner, T., 2010. Numerical simulation of magmatic hydrothermal systems. *Reviews of Geophysics* **48**, RG1002.

Kelley, D. S., Robinson, P. T., Malpas, J. G., 1992. Processes of brine generation and circulation in the oceanic crust: Fluid inclusion evidence from the Troodos ophiolite, Cyprus. *Journal of Geophysical Research* **97**, 9307-9322.

Kennedy, G. C., 1950. A portion of the system silica-water. *Economic Geology* **45**, 629-653.

Lalou, C., Reyss, J. L., Brichet, E., 1993. Actinide-series disequilibrium as a tool to establish the chronology of deep-sea hydrothermal activity. *Geochimica et Cosmochimica Acta* **57**, 1221-1231.

Lewis, K. C., Lowell, R. P., 2004. Mathematical modeling of phase separation of seawater near an igneous dike. *Geofluids* **4**, 197-209.

Lewis, K. C., Lowell, R. P., 2009a. Numerical modeling of two-phase flow in the NaCl-H_2O system: 2. Examples. *Journal of Geophysical Research* **114**, B08204.

Lewis, K. C., Lowell, R. P., 2009b. Numerical modeling of two-phase flow in the NaCl-H_2O system: Introduction of a numerical method and benchmarking. *Journal of Geophysical Research* **114**, B05202.

Liu, L., Lowell, R. P., 2009. Models of hydrothermal heat output from a convecting, crystallizing, replenished magma chamber beneath an oceanic spreading center. *Journal of Geophysical Research* **114**, B02102.

Lowell, R. P., 1991. Modeling Continental and Submarine Hydrothermal Systems. *Reviews of Geophysics* **29**, 457-476.

Lowell, R. P., Van Cappellen, P., Germanovich, L. N., 1993. Silica precipitation in fractures and the evolution of permeability in hydrothermal upflow zones. *Science* **260**, 192-194.

Manning, C. E., Ingebritsen, S. E., 1999. Permeability of the continental crust; implications of geothermal data and metamorphic systems. *Reviews of Geophysics* **37**, 127-150.

Martin, J. T., Lowell, R. P., 2000. Precipitation of quartz during high-temperature, fracture-controlled hydrothermal upflow at ocean ridges: Equilibrium versus linear kinetics. *Journal of Geophysical Research* **105**, 869-882.

Michael, P.J., Cornell, W.C., 1998. Influence of spreading rate and magma supply on crystallization and assimilation beneath mid-ocean ridges: Evidence from chlorine and major element chemistry of mid-ocean ridge basalts. *Journal of Geophysical Research* **103**, 18325-18356.

Mottl, M. J., Seewald, J. S., Wheat, C. G., Tivey, M. K., Michael, P. J., Proskurowski, G., McCollom, T. M., Reeves, E., Sharkey, J., You, C. F., Chan, L. H., Pichler, T., 2011. Chemistry of hot springs along the Eastern Lau Spreading Center. *Geochimica et Cosmochimica Acta* **75**, 1013-1038.

Nooner, S. L., Chadwick, W.W., 2009. Volcanic inflation measured in the caldera of Axial Seamount: Implications for magma supply and future eruptions. *Geochemistry Geophysics Geosystems* **10**, Q02002.

Norton, D. L., 1982. Fluid and heat transport phenomena typical of copper-bearing pluton environments; southeastern Arizona, in: Titley, S.R. (Ed.), *Advances in geology of porphyry copper deposits; southwestern North America*. Univ. Ariz. Press, Tucson, AZ.

Phillips, O. M., 1991. *Flow and reactions in permeable rocks*. Cambridge University Press, Cambridge, United Kingdom.

Reeves, E. P., Seewald, J. S., Saccocia, P., Bach, W., Craddock, P. R., Shanks, W. C., Sylva, S. P., Walsh, E., Pichler, T., Rosner, M., 2011. Geochemistry of hydrothermal fluids from the PACMANUS, Northeast Pual and Vienna Woods hydrothermal fields, Manus Basin, Papua New Guinea. *Geochimica et Cosmochimica Acta* **75**, 1088-1123.

Richardson, C. J., Cann, J. R., Richards, H. G., Cowan, J. G., 1987. Metal-depleted root zones of the Troodos ore-forming hydrothermal systems, Cyprus. *Earth and Planetary Science Letters* **84**, 243-253.

Seyfried, W. E., Ding, K., Berndt, M. E., 1991. Phase-equilibria constraints on the chemistry of hot-spring fluids at midocean ridges. *Geochimica et Cosmochimica Acta* **55**, 3559-3580.

Seyfried, W. E., Pester, N. J., Ding, K., Rough, M., 2011. Vent fluid chemistry of the Rainbow hydrothermal system (36°N, MAR): Phase equilibria and in situ pH controls on subseafloor alteration processes. *Geochimica et Cosmochimica Acta* **75**, 1574-1593.

Stakes, D., Vanko, D. A., 1986. Multistage hydrothermal alteration of gabbroic rocks from the failed Mathematician Ridge. *Earth and Planetary Science Letters* **79**, 75-92.

Turner, I. M., Peirce, C., Sinha, M. C., 1999. Seismic imaging of the axial region of the Valu Fa Ridge, Lau Basin; the accretionary processes of an intermediate back-arc spreading ridge. *Geophysical Journal International* **138**, 495-519.

Vanko, D. A., 1988. Temperature, pressure, and composition of hydrothermal fluids, with their bearing on the magnitude of tectonic uplift at mid-ocean ridges, inferred from fluid inclusions in oceanic layer 3. *Journal of Geophysical Research* **93**, 4595-4611.

Vanko, D. A., Bach, W., Roberts, S., Yeats, C. J., Scott, S. D., 2004. Fluid inclusion evidence for subsurface phase separation and variable fluid mixing regimes beneath the deep-sea PACMANUS hydrothermal field, Manus Basin back arc rift, Papua New Guinea. *Journal of Geophysical Research* **109**, B03201.

Vanko, D. A., Griffith, J. D., Erickson, C. L., 1992. Calcium-rich brines and other hydrothermal fluids in fluid inclusions from plutonic rocks, oceanographer transform, mid-Atlantic ridge. *Geochimica et Cosmochimica Acta* **56**, 35-47.

Von Damm, K.L., 1995. Controls on the chemistry and temporal variability of seafloor hydrothermal fluids, in: Humphris, S. E., Zierenberg, R. A., Mullineaux, L. S., Thomson, R.E. (Eds.), *Geophysical Monograph* **91**. American Geophysical Union, Washington DC, pp. 222-247.

Von Damm, K. L., 2004. Evolution of the hydrothermal system at East Pacific Rise 9°50'N; geochemical evidence for changes in the upper oceanic crust, in German, C.R., Lin, J., Parson, L.M (Eds.), *Geophysical Monograph* **148**. American Geophysical Union, Washington DC, pp.285-304.

Von Damm, K. L., Bischoff, J. L., Rosenbauer, R. J., 1991. Quartz solubility in hydrothermal seawater; an experimental study and equation describing quartz solubility for up to 0.5 M NaCl solutions. *American Journal of Science* **291**, 977-1007.

Wanless, V. D., Perfit, M. R., Ridley, W. I., Klein, E., 2010. Dacite Petrogenesis on Mid-Ocean Ridges: Evidence for Oceanic Crustal Melting and Assimilation. *Journal of Petrology* **51**, 2377-2410.

Welhan, J. A., Craig, H., 1979. Methane and hydrogen in East Pacific Rise hydrothermal fluids. *Geophysical Research Letters* **6**, 829-831.

Wells, J. T., Ghiorso, M. S., 1991. Coupled fluid flow and reaction in mid-ocean ridge hydrothermal systems; the behavior of silica. *Geochimica et Cosmochimica Acta* **55**, 2467-2481.

Wood, J. R., Hewett, T. A., 1982. Fluid convection and mass transfer in porous sandstones; a theoretical model. *Geochimica et Cosmochimica Acta* **46**, 1707-1713.

3.9 Figures

Figure 3.1. Isobaric quartz solubility as a function of temperature in pure H_2O, H_2O + 3.2 wt% NaCl, and H_2O + 10 wt% NaCl fluids, at 20 MPa (bottom) and 50 MPa (top). Regions in which retrograde solubility and immiscibility occur are shaded yellow and pink, respectively. Where immiscibility occurs, quartz solubility is higher in the high-salinity liquid and lower in the low-salinity vapor. Quartz solubility was calculated using the equation of Akinfiev and Diamond (2009)

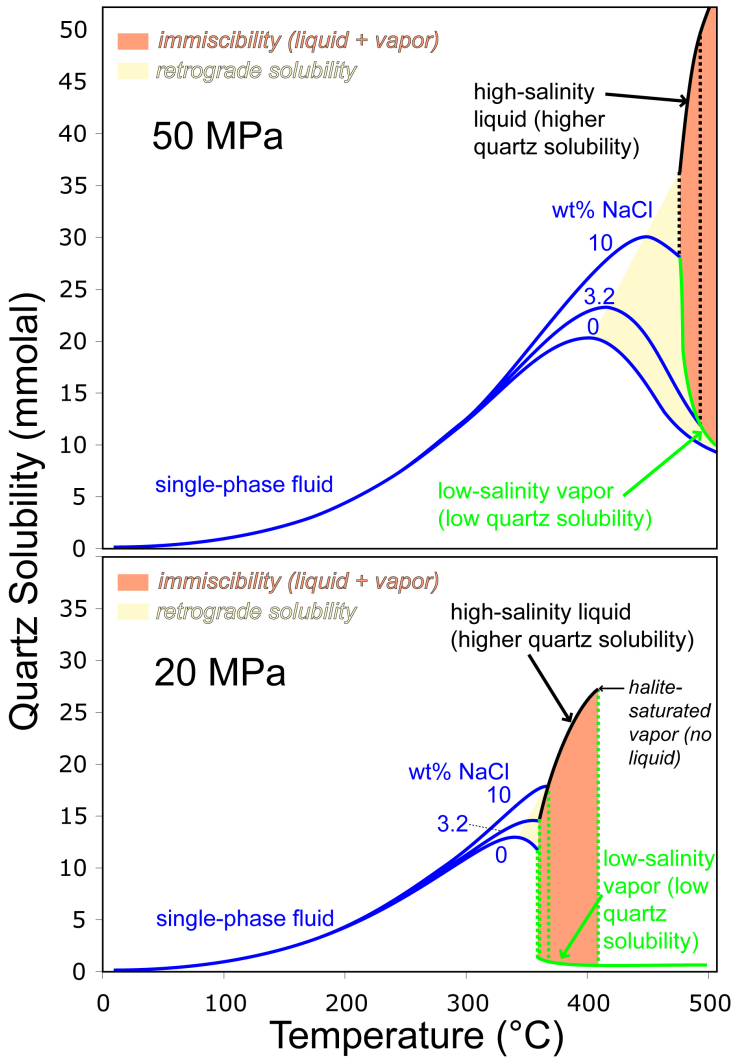

Figure 3.2. Schematic illustration of the initial and boundary conditions of the fluid flow model. All simulations were done with a constant-pressure, flow-through upper boundary condition and variable-pressure, no-flow side boundary conditions. The bottom boundary condition was no-flow and constant temperature, with temperature increasing linearly from 300°C at the bottom right to the maximum temperature of the bottom heat source at a distance of 500 m from the left side All runs had a homogeneous permeability, i.e. no constrained flow geometry was imposed. The simulations were conducted using the package FISHES, developed and described by Lewis and Lowell (2009a, b).

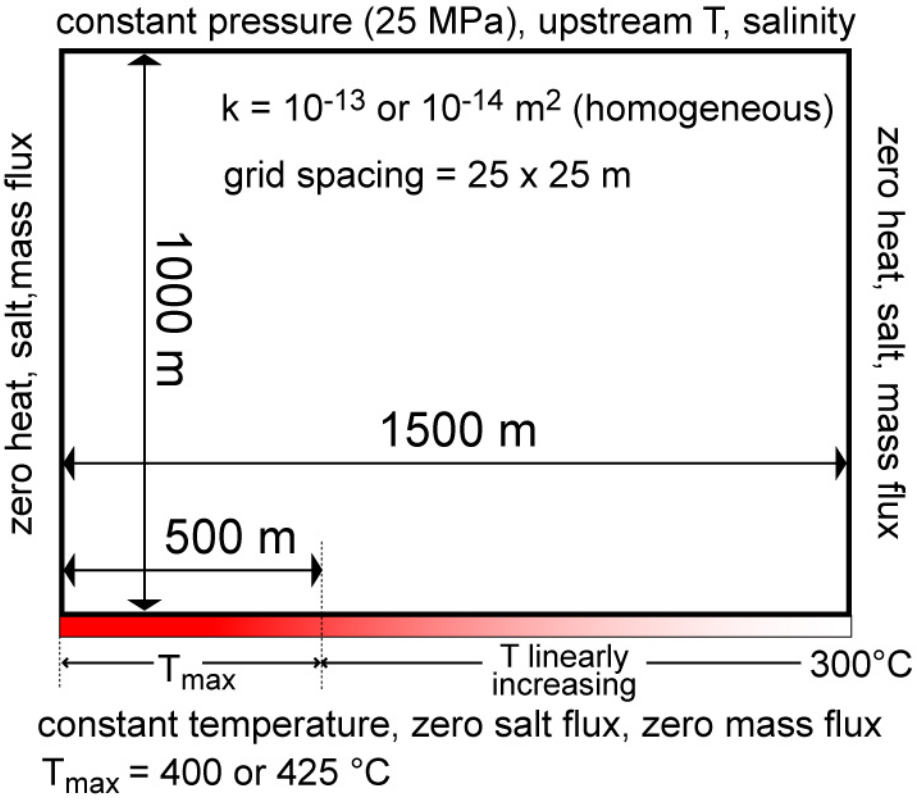

Figure 3.3. One-dimensional fluid flow model assuming twenty-five 2 × 2 m cells and a constant heat flux of 1 W/m^2 along the bottom.
A two-phase region indicated by the low liquid volume saturation develops during the first year and expands upwards through time. Quartz solubility in the two-phase region decreases with time as liquid pools at the bottom. The right-hand graph shows the solubility of quartz in the individual liquid and vapor phases and the bulk quarts solubility at the 10-year time interval. The quartz solubility marked with the asterisk (*) is bulk quartz solubility in the liquid plus vapor region; quartz solubility in the coexisting liquid and vapor phases is shown for year 10 on the right.

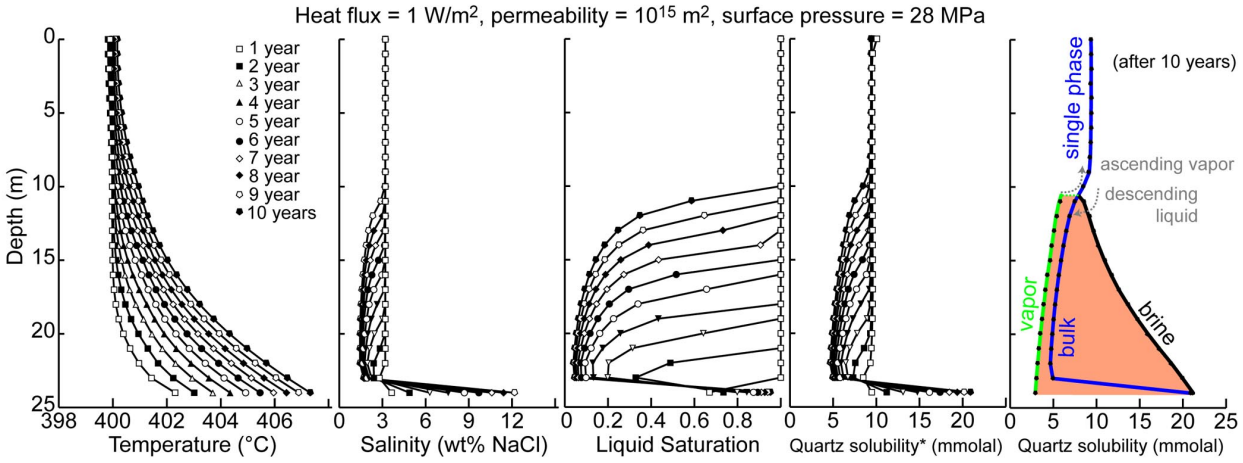

Figure 3.4. Thermal profiles and fluid velocity vectors for a single time-slice from each of the four simulations (permeability of 10^{-14} (left) and 10^{-13} m^2 (right), and maximum bottom temperature of 400 (bottom) and 425 °C (top)).
The vectors in black represent the liquid phase, and the vectors in white represent the vapor phase. The length of the vector arrows is proportional to the magnitude of the velocity. The year of each time slice is indicated in the upper right of each plot.

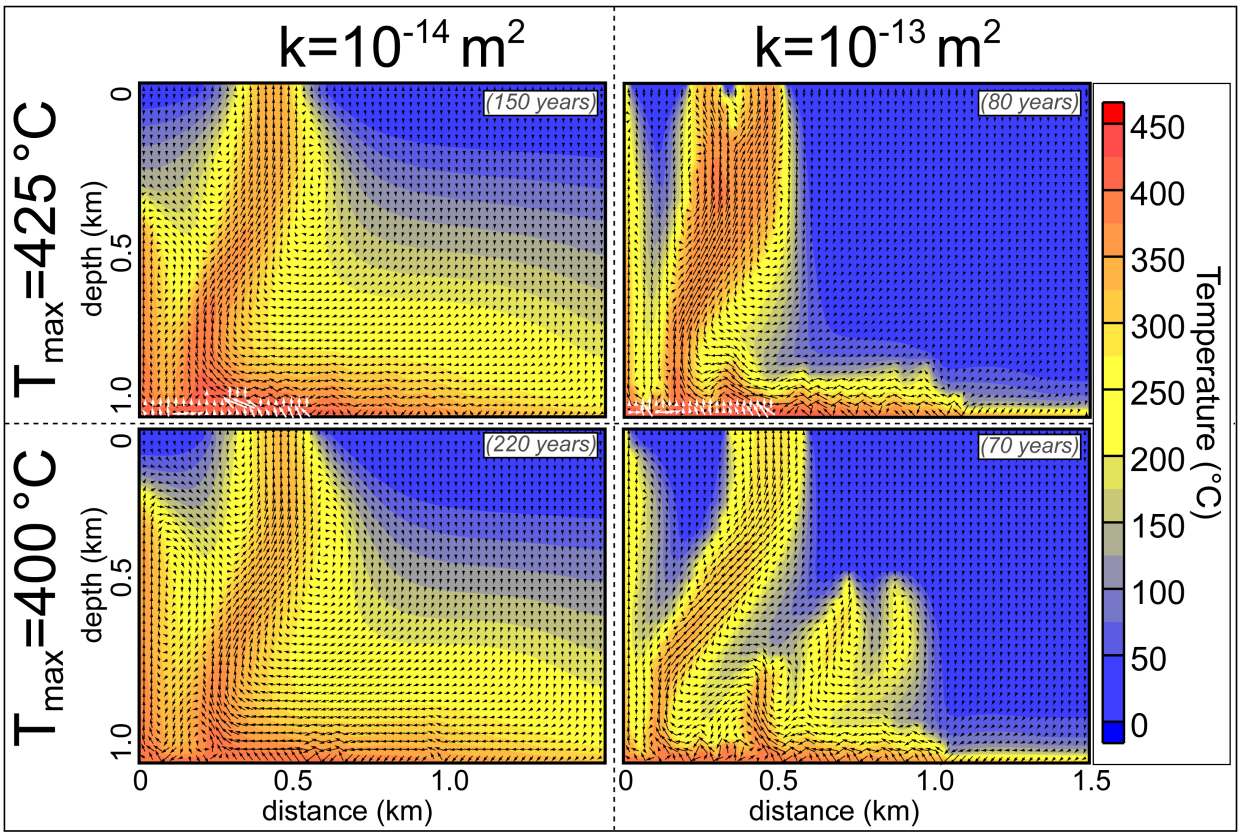

Figure 3.5. Quartz solubility distribution for the k = 10^{-13} m^2, T_{max} = 400 °C simulation at 70 years.
The top cross-section shows contours of quartz solubility within the system. The middle and bottom plots show the quartz solubility and temperature, respectively, of the hydrothermal fluid versus distance along an artery of high fluid mass flux (traced by the vectors on the contour plot - to the left and above the cross-section, the horizontal mass flux across the green slice and the vertical flux across the blue slice are shown, to emphasize the mass flux-dominance of this artery). The points labeled *a*, *b*, *c*, *d* and *e* on the contour plot correspond to the x-axis coordinates on the middle and bottom graphs. Zones of retrograde quartz solubility (quartz solubility increasing with decreasing temperature) are highlighted in yellow.

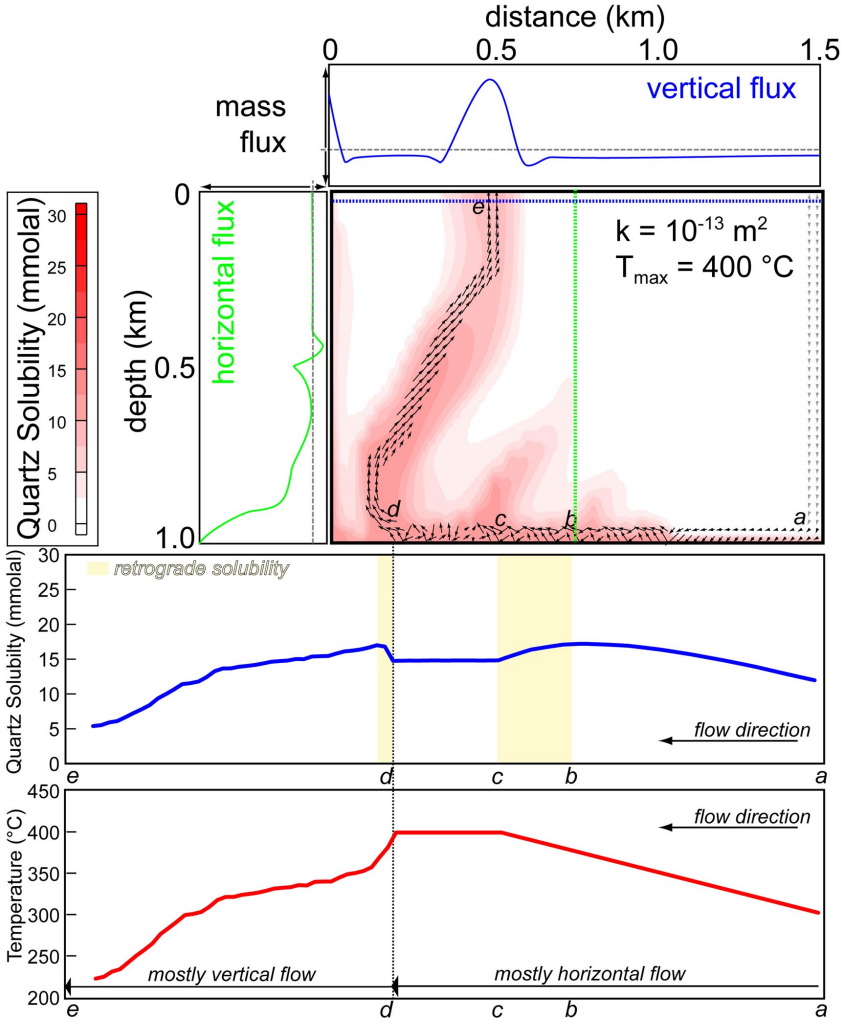

Figure 3.6. Quartz solubility distribution for the k = 10^{-13} m^2, T_{max} = 425 °C simulation at 80 years.
See the description in the caption of Figure 3.5.The pink-shaded zone on the quartz solubility versus distance plot (middle) represents the region in which liquid-vapor immiscibility occurs. Within the immiscibility region, the quartz solubility in the higher-salinity liquid (brine) is in black and the quartz solubility in the lower-salinity vapor is in green. The intermediate blue curve shows the mass-balanced bulk quartz solubility in the liquid-vapor mixture.

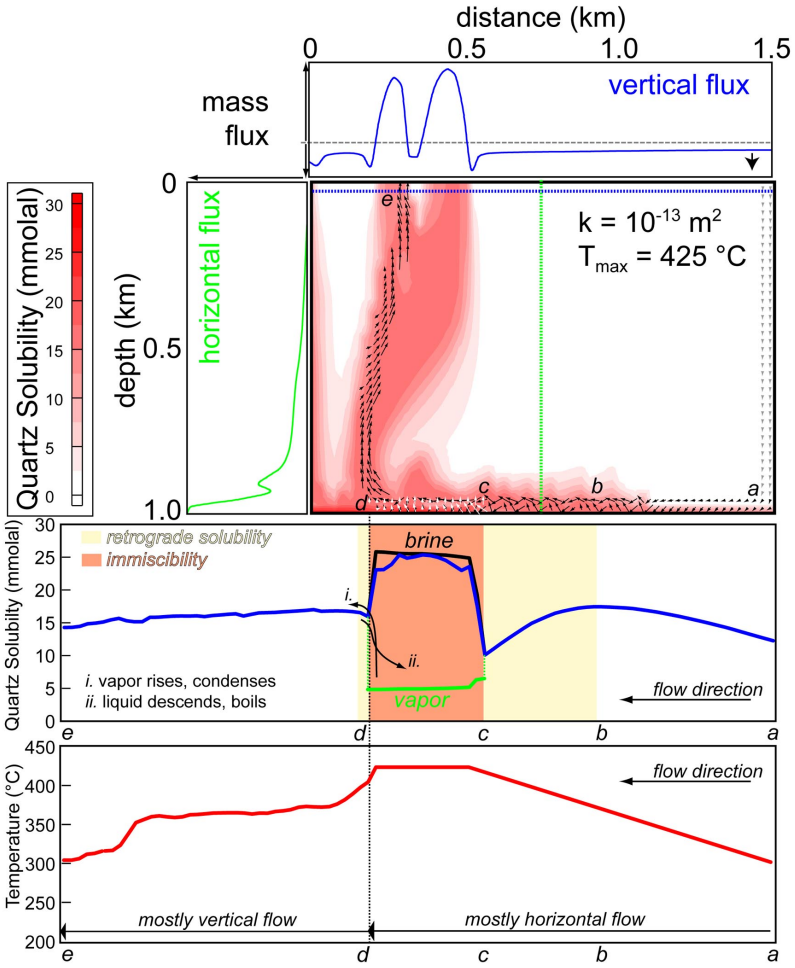

Figure 3.7. Evolution of quartz dissolution and precipitation in the 400 °C, 10^{-13} m^2 hydrothermal system from 20 to 100 years of simulated time.
The model initially evolves towards a quasi-steady state that is achieved at ~50-60 years, and the model is quasi-steady state thereafter.

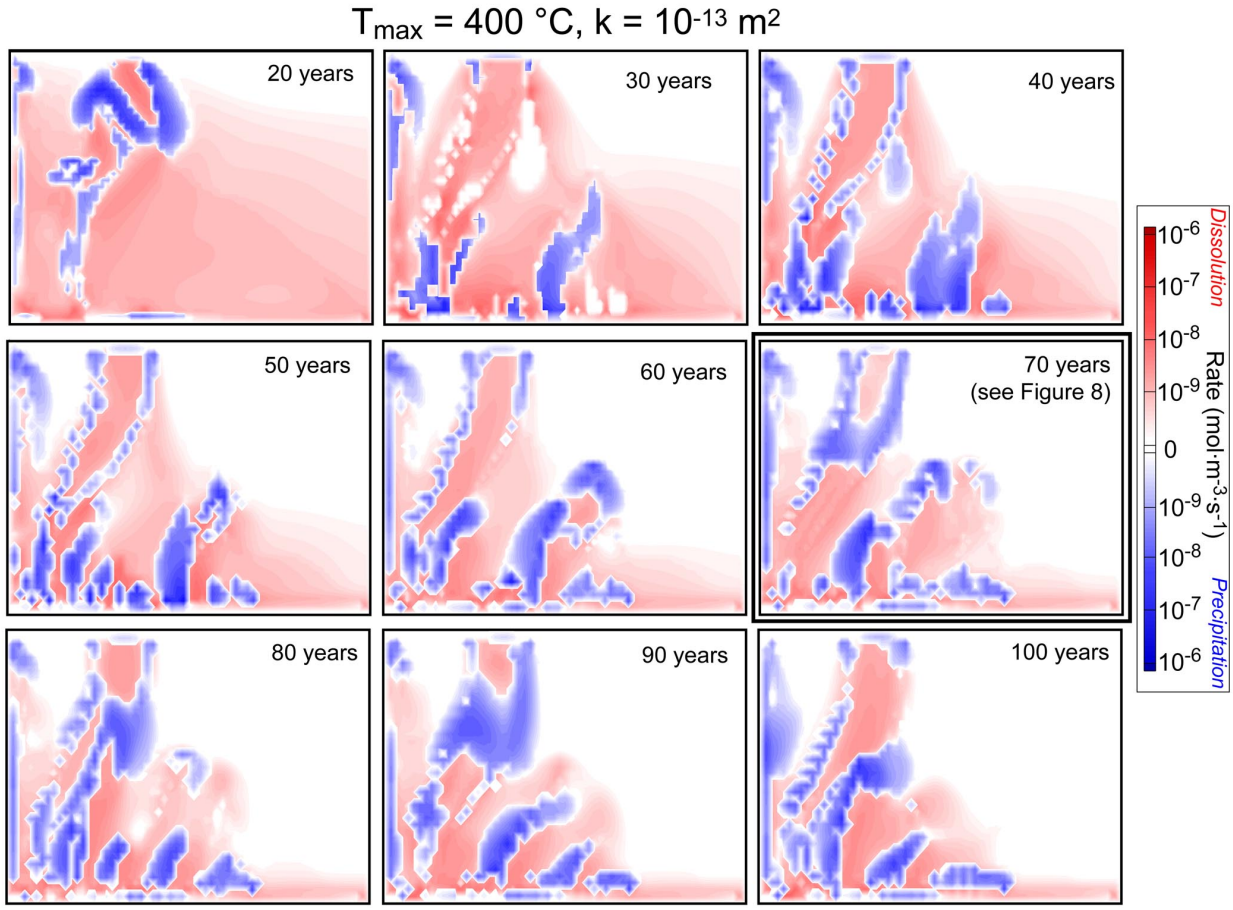

Figure 3.8. Regions of quartz dissolution and precipitation predicted for each of the four simulations.
Areas of quartz dissolution are shown in red and zones of precipitation are shown in blue. Notice the different z-axis scaling for the higher permeability simulations (right) and the lower permeability runs (left). The intensity of dissolution and precipitation increases with increasing permeability (compare left plots to right plots) and with increasing temperature (compare bottom plots to top plots). For reference, the letter markers from Figures 3.5 and 3.6 are shown on the right-hand (10^{-13} m^2) plots. See the text for additional details.

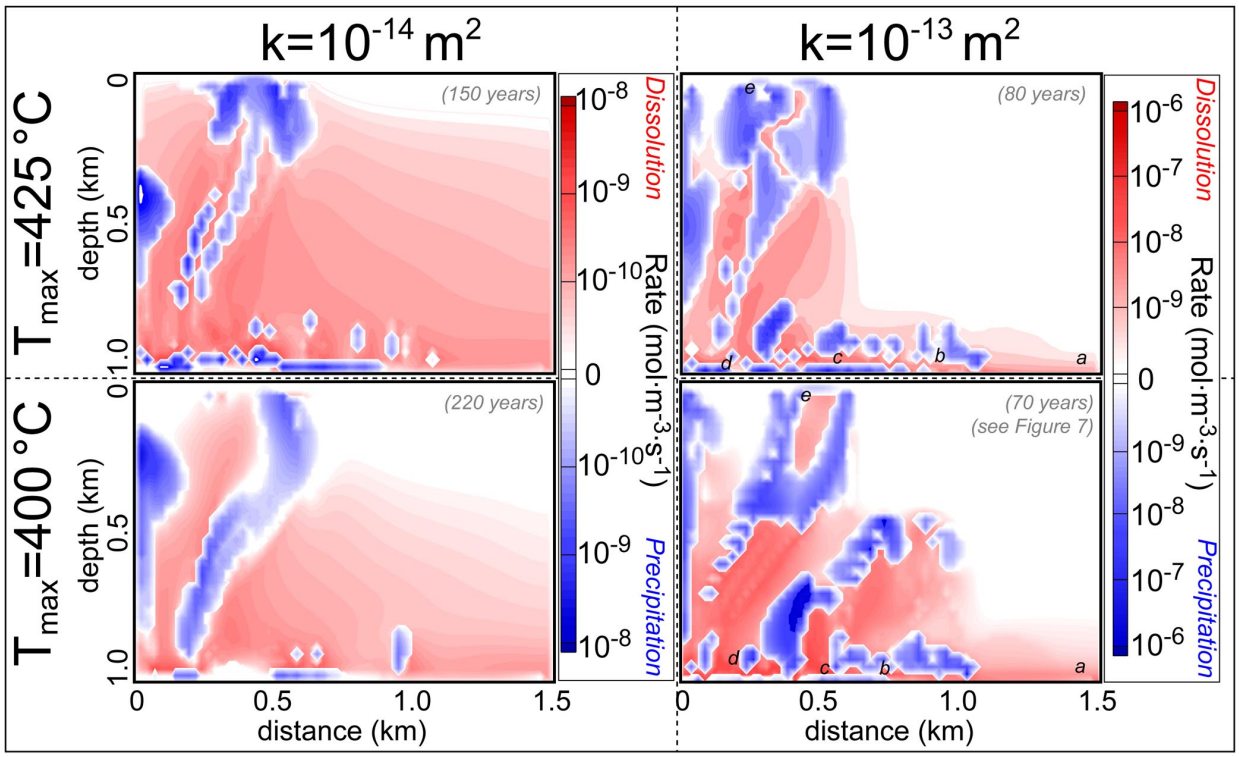

[3]Reprinted from *Earth and Planetary Science Letters*, 321-322, Steele-MacInnis, M., Han, L., Lowell, R.P., Rimstidt, J.D. & Bodnar, R.J., The role of fluid phase immiscibility in quartz dissolution and precipitation in sub-seafloor hydrothermal systems, 139-151, Copyright (2012), with permission from Elsevier.